Magneto-optical properties of II-VI semiconductor colloidal nanostructures

Dissertation

presented to the Faculty of Physics of the
TU Dortmund University, Germany,
in partial fulfillment of the requirements
for the degree of

Doktor rer. nat.

by

Feng Liu

technische universität
dortmund

Dortmund, June 2013

Examination board:
Prof. Dr. Dmitri R. Yakovlev
Prof. Dr. Heinz Hövel
Prof. Dr. Bernhard Spaan
Dr. Jörg Debus

Contents

Chapter 1

Introduction

1.1 Motivation

Nowadays, semiconductor-based electronic devices, such as computers, smart phones and digital cameras, already become the base of our modern life. Currently, one of the biggest challenges for the semiconductor industry is the miniaturization of semiconductor devices. Following the trend predicted by Moore[1], the size of the basic unit for most semiconductor devices – field effect transistor – already steps into nanometre scale and will reach the physical limit soon. Therefore low-dimensional semiconductor structures, such as two-dimensional quantum wells, one-dimensional quantum wires and zero-dimensional quantum dots, are required to continue the miniaturization of semiconductor devices and develop new technologies taking advantages of various miraculous quantum effects. Among different low-dimensional semiconductor nanostructures, colloidal nanocrystals (NCs) attract much attention due to their importance in fundamental research on zero-dimensional structures and great potential in a variety of practical applications, such as spintronics[2], quantum information[3,4] , light emitting diodes[5], optically pumped lasing[6], and biolabeling[7,8].

Colloidal semiconductor nanocrystals are crystallized semiconductor nanostructures synthesized using wet chemical method[9,10]. Since the discovery of colloidal NCs, they have suffered a lot from the non-radiative Auger process for a long time[11,12], which significantly limits the practical application of colloidal nanocrystals. However, the situation has changed with the growth of CdSe/CdS core/thick-shell NCs, recently reported by two groups[13,14]. The interest on this new type of thick-shell colloidal NCs is stimulated by their optical properties that are superior to any other NC heterostructures fabricated up to now. The photoluminescence is never completely quenched in these NCs[15] and the blinking is almost completely suppressed[13,16]. The structures demonstrate suppression of non-radiative Auger recombination[17,18] and almost 100% photoluminescence quantum yield[8,19]. Op-

tical properties of colloidal NCs are determined by the fine structure of exciton complexes. Until now, although the exciton fine structure of conventional thin-shell NCs have been studied both theoretically[20,21,22,23] and experimentally[20,24,25,26,27,28], there is still a lack of systematic study of the fine structure of exciton complexes in the new type of thick-shell CdSe/CdS NCs. In addition, there is no study of the spin dynamics of exciton complexes in this type of NCs which is rather important for both the fundamental understanding of properties of thick-shell CdSe/CdS NCs and practical applications.

Besides optical properties of individual colloidal NCs, the interaction between colloidal NCs is also a very interesting topic for fundamental research and can be potentially used in a variety of fields, such as photovoltaics[29,30,31], nanophotonic circuitry[32], light emitting diode[33] and biosensors[34]. One of the most important ways for colloidal NCs to communicate with each other is long-range non-radiative Förster resonant energy transfer (FRET)[35] realized via dipole-dipole interaction. FRET in an ensemble of colloidal NCs has been intensively studied in different material systems, such as CdTe NCs[36], CdSe NCs[37] and PbS NCs[38], with different shapes[39,40] and structures, such as monodispersed ensemble NCs[41,42], bilayer structure[43,44] and cascaded energy transfer structure[45,46]. It was found that the energy transfer (ET) rate between colloidal NCs could be as fast as hundreds of picoseconds[47] and the ET efficiency is influenced by temperature[48] and the distance between NCs[49,43]. However, most of previous studies were performed at room temperature, where bright- and dark-exciton states are already fully thermally mixed. To have a deep insight into the FRET in colloidal NCs, a study conducted at cryogenetic temperatures is needed. Additionally, up to now there is no detailed study of the influence of magnetic field on FRET in colloidal NCs. Although an enhancement ($\sim$7%) of ET efficiency by mangetic field (10 T) was reported[50], these data were estimated indirectly with low accuracy. To correctly and accurately estimate the enhancement of ET rate by mangetic field, experimental techniques allowing direct measurement of the ET rate has to be employed and a more detailed model is required.

For a long time, the synthesis of colloidal NCs was limited to zero-dimensional quasi-spherical nanocrystals. Later on, the route to quasi-1D behavior was opened by the fabrication of rod-shaped[51] and tetrapod-shaped[52] nanocrystals. However one of the problems of these colloidal nanostrucutres is that in the ensemble sample, these colloidal nanostructures are randomly oriented, which on the one hand limits their practical application and on the other hand complicates the interpretation of experimental results. Very recently, zero-dimensional colloidal NCs with two-dimensional shell – dot-in-plate structure[53] – and two-dimensional colloidal nanostructure – nanoplatelet[54,55] – were successfully synthesized. These new types of colloidal nanostructures overcome the orientation problem and show much narrower line width compared with that of ensemble quasi-spherical NCs, which indicates a highly improved uniformity of the size of these nanostructures[54]. Since

these two-dimensional colloidal nanostructures are only available recently, until now there are very few study on their basic magneto-optical properties and the exciton fine structure is still unclear. Therefore, to have a comprehensive understanding of these colloidal nanostructures, a detailed temperature dependence and magneto-optical study are needed.

1.2 Thesis structure

The aim of this research is to investigate fundamental properties, e.g. g-factor of exciton complexes, spin dynamics and bright-dark splitting, of a variety of colloidal nanostructures and explore new interesting phenomena in these colloidal nanostructures using magneto-optical experimental techniques. The summary of the results is organized in the following way: Firstly the motivation and a brief literature review for this research field is presented in Chap. 1. Secondly, the existed theoretical basis and newly developed theories needed to understand and explain the experimental results are introduced in Chap. 2. Thirdly, samples and experimental techniques employed in this research are described in Chap. 3. Fourthly, the spin dynamics of negative trions in CdSe/CdS core/thick-shell colloidal nanocrystals are discussed in Chap. 4. Fifthly, following the study of CdSe NCs, spin dynamics and FRET phenomenon in CdTe colloidal NCs are explored and the results are shown in Chap. 5. Finally, the experimental results about recombination and spin dynamics of CdSe-based platelet colloidal structures are presented and discussed in Chap. 6.

Chapter 2

Theoretical background

This chapter introduces existed theoretical basis and newly developed theories used in our study on colloidal nanostructures. The chapter is organized as follows: firstly, the definition of colloidal semiconductor nanostructures is briefly explained. Secondly, exciton fine structure in colloidal nanocrystals (NCs) are presented. Thirdly, the temperature dependence of recombination dynamics in colloidal NCs is introduced. Fourthly, the PL polarization degree of excitons and negative trions in colloidal NCs is derived. Fifthly, the spin relaxation mechanism of negative trions in thick-shell CdSe/CdS colloidal NCs is discussed. Finally, a model describing the non-radiative energy transfer process in colloidal NCs is introduced.

2.1 Colloidal semiconductor nanostructures

Colloidal semiconductor nanostructures are semiconductor nanostructures synthesized using wet chemical method in which colloidal nanostructures are self-assembled in a solvent heated up to sufficiently high temperature[9,10]. In past decade, the most intensively studied colloidal nanostructure is quasi-spherical colloidal nanocrystals (NCs). Quasi-spherical colloidal NC is crystallized semiconductor sphere with a diameter of a few nanometers. In the solvent, colloidal NCs tend to conjugate to bigger clusters. To prevent the aggregation of NCs, the core of colloidal NCs is usually protected by ligands or an additional shell. Figure 2-1 shows a transmission electron microscopy (TEM) image of core/shell CdSe/CdS colloidal NCs with a core diameter of 1.5 nm and shell thickness of 6 nm.

In additional to spherical colloidal NCs, even more complicated structures, such as dot-in-rod structures (spherical core in cylindrical shell)[56,57], nanoplatelets (nanostructures with two-dimensional confinement)[58], dot-in-plate structures[53] and dot-in-tetrapod structures[40,52], can be fabricated by varying the synthesis conditions.

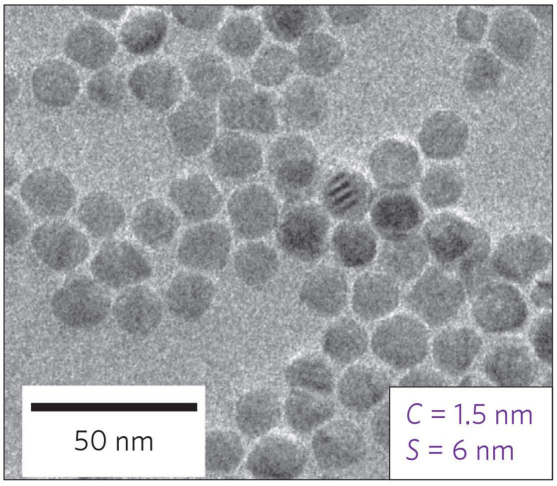

Figure 2-1: The transmission electron microscopy (TEM) image of core/shell CdSe/CdS colloidal NCs. The diameter of the core is 1.5 nm and the shell thickness is 6 nm[18].The image was taken on a JEOL 2010 field electron gun microscope operated at 200 keV. This figure is adapted from Ref. 18.

2.2 Exciton fine structure in colloidal NCs

Optical properties of neutral colloidal NCs are determined by the exciton fine structure. Since the Coulomb interaction between electron and hole can be considered as perturbation in strong confinement regime, the exciton fine structure can be calculated from solving the Schrödinger equation of electron and hole in a spherical potential respectively with effective mass approximation. Wave functions and energy of the ground state of an electron in a two-fold degenerated conduction band (the projection of electron spin $s_z = \pm 1/2$) and a hole in a four-fold degenerated valence band (the projection of the total momentum: $M = \pm 1/2, \pm 3/2$) in a spherical potential with infinite potential barrier for carries are[20]:

$$E_{1S} = \frac{\hbar^2 \pi^2}{2m_{\mathrm{e}}^* a^2} \tag{2.1}$$

$$\psi_\alpha(\mathbf{r}) = \xi(\mathbf{r})|S\alpha\rangle = \sqrt{\frac{2}{a}}\frac{\sin(\pi r/a)}{r} Y_{00}(\Omega)|S\alpha\rangle \tag{2.2}$$

$$E_{3/2}(\beta) = \frac{\hbar^2 \varphi^2(\beta)}{2m_{\mathrm{hh}}^* a^2} \tag{2.3}$$

$$\psi_M(\mathbf{r}) = 2\sum_{l=0,2} R_l r(-1)^{M-3/2} \times \sum_{m+\mu=M} \begin{pmatrix} 3/2 & l & 3/2 \\ \mu & m & -M \end{pmatrix} Y_l m(\Omega) u_\mu \tag{2.4}$$

E_{1S} and $\psi_\alpha(\mathbf{r})$ are the energy and wave function of electron. $E_{3/2}(\beta)$ and $\psi_M(\mathbf{r})$ are the energy and wave function of hole. The two-fold degenerated electron state and four-fold degenerated hole state result in a eight-fold degenerated exciton state ($1S_{3/2}1S_{\mathrm{e}}$) whose wave functions and energy are characterized by the sum of the

projection of the electron spin and hole total momentum, $J_z = s_z + M$.[20] In colloidal NCs, the degeneracy of the $1S_{3/2}1S_e$ state is lifted by three factors: electron-hole exchange interaction originating from the coupling between electron spin and hole angular momentum, shape asymmetry, such as prolate or oblate shape, and internal crystal structure anisotropy, such as hexagonal crystal structure. The energy of these three factors can be written as[20]:

$$\widehat{H}_{\text{exch}} = -(2/3)\epsilon_{\text{exch}}(a_0)^3\delta(\mathbf{r}_e - \mathbf{r}_h)\sigma J \tag{2.5}$$

$$\Delta_{\text{int}} = \Delta_{cr}v(\beta) \tag{2.6}$$

$$\Delta_{\text{sh}} = 2\mu u(\beta)E_{3/2}(\beta) \tag{2.7}$$

where $\mu = c/b - 1$. c and b are the major and minor axes of the ellipsoid.

By solving the secular equation $(\widehat{E} - \epsilon_{|F|}) = 0$ which takes into account all three factors above, wave functions and energy of the eight states can be obtained[20]:

$$\epsilon_{|F|=2} = -3\eta/2 - \Delta/2 \tag{2.8}$$

$$\Psi_{-2}(\mathbf{r}_e, \mathbf{r}_h) = \Psi_{\downarrow,-3/2}(\mathbf{r}_e, \mathbf{r}_h) \tag{2.9}$$

$$\Psi_{2}(\mathbf{r}_e, \mathbf{r}_h) = \Psi_{\uparrow,3/2}(\mathbf{r}_e, \mathbf{r}_h) \tag{2.10}$$

$$\epsilon^{\text{U,L}}_{|F|=2} = \eta/2 \pm \sqrt{(2\eta - \Delta)^2/4 + 3\eta^2} \tag{2.11}$$

$$\Psi^{\text{U,L}}_{1}(\mathbf{r}_e, \mathbf{r}_h) = \mp iC^{+}\Psi_{\uparrow,1/2}(\mathbf{r}_e, \mathbf{r}_h) + C^{-}\Psi_{\downarrow,3/2}(\mathbf{r}_e, \mathbf{r}_h) \tag{2.12}$$

$$\Psi^{\text{U,L}}_{-1}(\mathbf{r}_e, \mathbf{r}_h) = \mp iC^{-}\Psi_{\uparrow,-3/2}(\mathbf{r}_e, \mathbf{r}_h) + C^{+}\Psi_{\downarrow,-1/2}(\mathbf{r}_e, \mathbf{r}_h) \tag{2.13}$$

$$\epsilon^{\text{U,L}}_{|F|=0} = \eta/2 - \Delta/2 \pm 2\eta \tag{2.14}$$

$$\Psi^{\text{U,L}}_{0}(\mathbf{r}_e, \mathbf{r}_h) = \frac{1}{\sqrt{2}}[\mp i\Psi_{\uparrow,-1/2}(\mathbf{r}_e, \mathbf{r}_h) + \Psi_{\downarrow,1/2}(\mathbf{r}_e, \mathbf{r}_h)] \tag{2.15}$$

where $\Delta(a, \beta, \mu) = \Delta_{\text{ini}} + \Delta_{\text{sh}}$. It can be seen that the energy of these states are highly dependent on the size a and shape μ of colloidal NCs. Figure 2-2 and 2-3 shows the calculated size dependence of exciton fine structures in hexagonal CdSe colloidal NCs and cubic CdTe colloidal NCs with different shapes. It can be seen that in most cases, except spherical CdTe NCs, the lowest state is optically passive state (or dark state), which makes optical properties of colloidal NCs quite different from epitaxial grown quantum dots (QDs).

2.3 Temperature dependence of recombination dynamics

Although the exciton fine structure is complicated, since these energy levels are well separated due to the strong confinement, the recombination dynamics of excitons

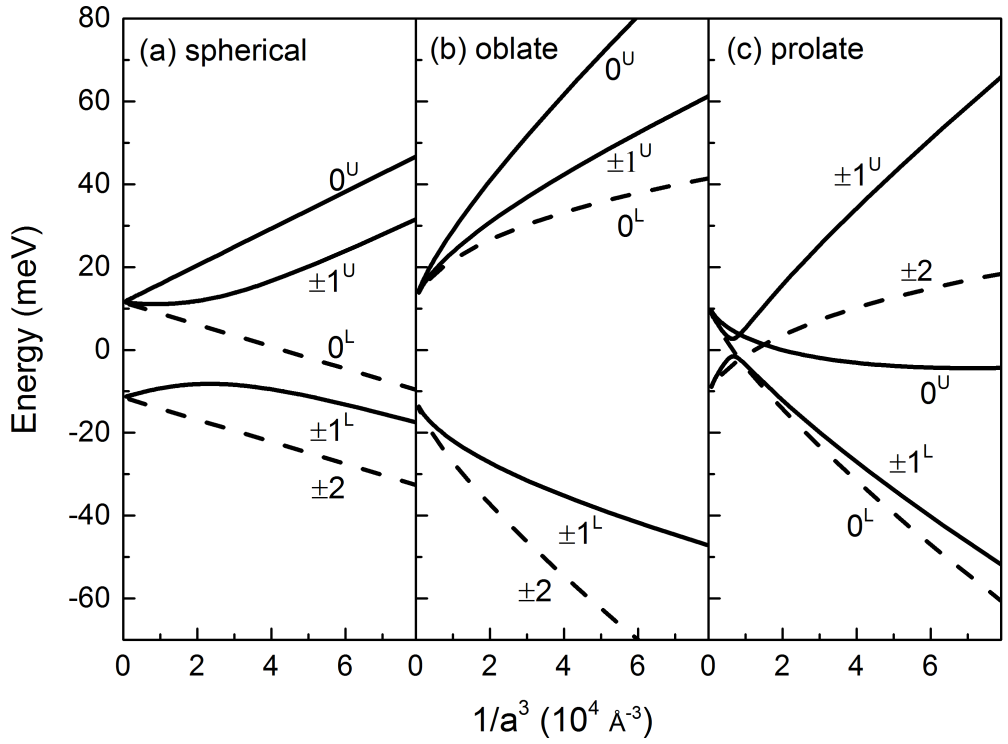

Figure 2-2: Size dependence of exciton fine structure in hexagonal CdSe NCs with (a) spherical ($\mu = 0$) (b) oblate ($\mu = -0.28$) and (c) prolate ($\mu = 0.28$) shape. $\beta = 0.28$. Figures are adapted from Ref. 20.

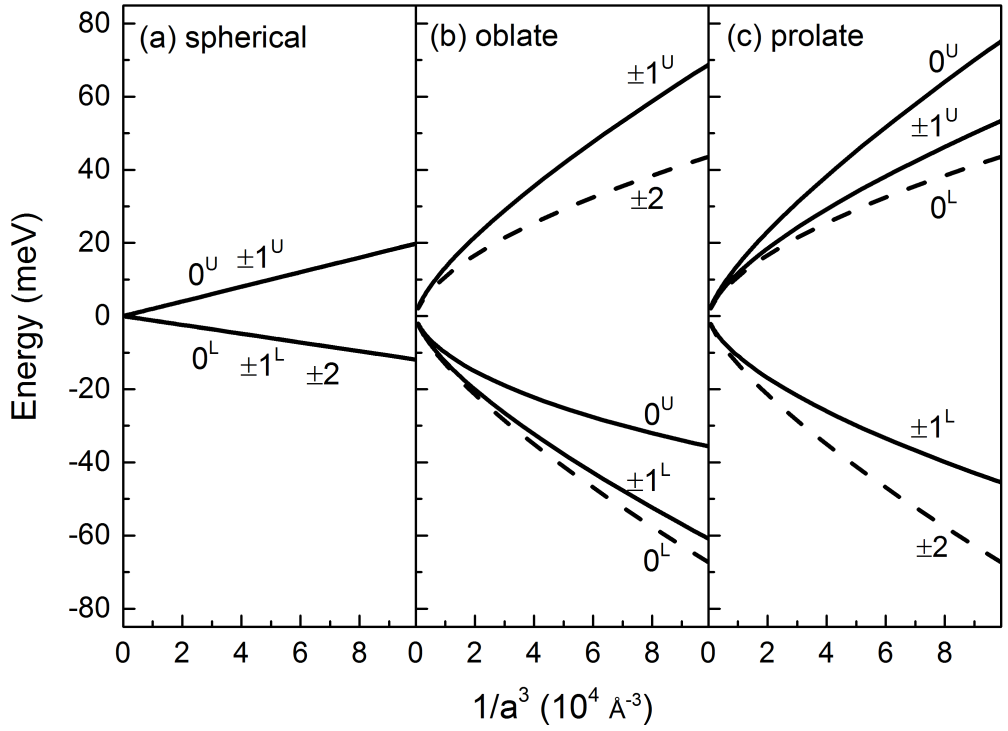

Figure 2-3: Size dependence of exciton fine structure in cubic CdTe NCs with (a) spherical ($\mu = 0$) (b) oblate ($\mu = -0.28$) and (c) prolate ($\mu = 0.28$) shape. $\beta = 0.086$. Figures are adapted from Ref. 20.

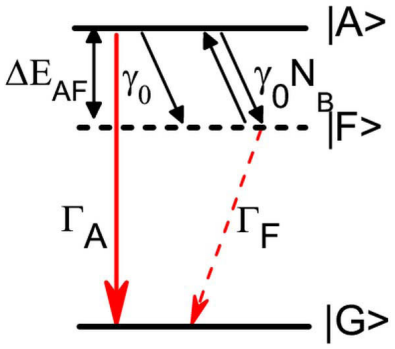

Figure 2-4: Energy level scheme of excitons in colloidal NCs. $|A\rangle$ and $|F\rangle$ are optically allowed state (bright state) and optically forbidden state (dark state). $|G\rangle$ is the ground state. ΔE_{AF} is the energy difference between bright and dark states. γ_0 is the relaxation rate from bright state to dark state at $T = 0$. At $T > 0$, excitons can be thermally excited to bright state from dark state and relax back. In the case of one-phonon assisted relaxation, this process is characterized by $\gamma_0 N_B$, where N_B is the Bose-Einstein phonon number at temperature T ($N_B = 1/[\exp(\Delta E/k_B T) - 1]$)[59]. Γ_A and Γ_F are recombination rates of bright and dark states.

in colloidal NCs can be well described by a three-level model which involves the lowest dark state and the lowest bright state (see Fig. 2-4)[59]. The recombination dynamics of such a system excited by a short laser pulse is described by rate equations:

$$\frac{dN_A}{dt} = -N_A(\Gamma_A + \gamma_0(1 + N_B)) + N_F\gamma_0 N_B \tag{2.16}$$

$$\frac{dN_F}{dt} = -N_F(\Gamma_F + \gamma_0 N_B) + N_A\gamma_0(1 + N_B) \tag{2.17}$$

In the case of nonresonant excitation, $N_A(t = 0)$ is equal to $N_F(t = 0) = 0.5$. Due to the existence of non-radiative channels in colloidal NCs, not all excitons relaxing to the ground state are converted to photons. By taking into account the non-radiative channel, the PL intensity can be written as[59]:

$$I(t) = \eta_A\Gamma_A N_A + \eta_F\Gamma_F N_F \tag{2.18}$$

where η_A and η_F are radiative quantum efficiency of bright and dark states. By solving rate equations and Eq. (2.18) in the approximation $\gamma_0 >> \Gamma_A >> \Gamma_F$, the radiative recombination dynamics can be obtained[59]:

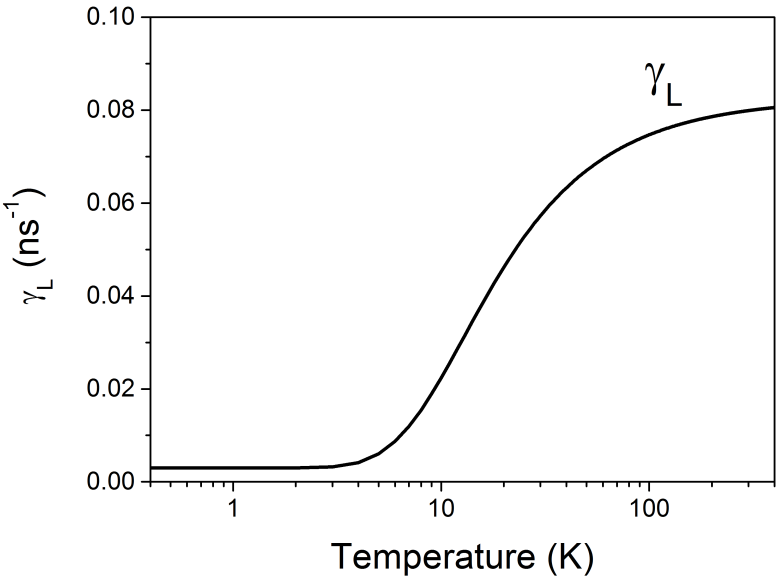

Figure 2-5: Calculated temperature dependence of γ_{L} in CdTe colloidal NCs. Parameters: $\Gamma_{\mathrm{A}} = 0.162$ ns^{-1}, $\Gamma_{\mathrm{F}} = 0.003$ ns^{-1}, $\Delta_{\mathrm{AF}} = 1.7$ meV.

$$I(t) = \frac{\eta_{\mathrm{A}}\Gamma_{\mathrm{A}}N_{\mathrm{B}} + \eta_{\mathrm{F}}\Gamma_{\mathrm{F}}}{1+2N_{\mathrm{B}}}\exp\left(-\frac{t}{\tau_{\mathrm{L}}}\right) + \eta_{\mathrm{A}}\Gamma_{\mathrm{A}}\left[N_{\mathrm{A}}(0) - \frac{N_{\mathrm{B}}}{1+2N_{\mathrm{B}}}\right]\exp\left(-\frac{t}{\tau_{\mathrm{S}}}\right) \tag{2.19}$$

$$\tau_{\mathrm{L}}^{-1} = \frac{\Gamma_{\mathrm{A}}+\Gamma_{\mathrm{F}}}{2} - \left(\frac{\Gamma_{\mathrm{A}}-\Gamma_{\mathrm{F}}}{2}\right)\tanh\left(\frac{\Delta E_{\mathrm{AF}}}{2k_{\mathrm{B}}T}\right) \tag{2.20}$$

$$\tau_{\mathrm{S}}^{-1} = \gamma_0(1+2N_{\mathrm{B}}) \tag{2.21}$$

where k_{B} is the Boltzmann constant. The temperature dependence of PL decay of excitons in neutral colloidal NCs can be clearly explained by equations above. The PL decay consists of a short component and a long component with decay time τ_{L} and τ_{S} respectively. In the low temperature limit $k_{\mathrm{B}}T << \Delta E_{\mathrm{AF}}$, the decay time of the short component is only determined by γ_0 and the decay time of the long component is only determined by γ_{F}. With the increase of temperature, both short component and long component becomes faster. In the high temperature limit $k_{\mathrm{B}}T >> \Delta E_{\mathrm{AF}}$, the amplitude of the short component approaches to zero in the case of nonresonant excitation and the PL decay only contains one component with the decay time of $(\Gamma_{\mathrm{A}}+\Gamma_{\mathrm{F}})/2$[59]. With all parameters determined in the low and high temperature limit ($\gamma_0, \Gamma_{\mathrm{A}}$ and Γ_{F}), the bright-dark splitting energy ΔE_{AF} can be extracted by fitting the temperature dependence of the decay time of the long component. A calculated temperature dependence of γ_{L} of CdTe colloidal NCs is shown in Fig. 2-5.

2.4 Effect of magnetic field on exciton complexes

Magnetic field plays a key role in the recombination dynamics and spin dynamics of an exciton complex, e.g. a neutral or charged exciton, in colloidal NCs. In neutral colloidal NCs with hexagonal crystal structures and/or non-spherical shape, the spin of hole is always aligned along a special quantization axis originating from the internal crystal anisotropy and shape asymmetry. The spin of electron is also aligned along this quantization axis due to the exchange interaction between hole and electron. Therefore,the Zeeman splitting of excitons is dependent on exciton g-factor, magnetic field and the angle between magnetic field and the quantization axis:

$$\Delta E = 2g\mu_{\mathrm{B}}\mathbf{B}\cdot\mathbf{J}/\hbar = 2g\mu_{\mathrm{B}}BJ_z\cos(\theta) \tag{2.22}$$

where μ_{B} is the Bohr magneton. $\mathbf{J}$ is the sum of spin of electron and total momentum of heavy hole. $J_z = s_z + M$ is the project of $\mathbf{J}$ on the quantization axis. θ is the angle between magnetic field and the quantization axis. The transverse component of magnetic field which is perpendicular to the quantization axis mixes the bright- and dark-exciton states resulting in an acceleration of both the recombination dynamics of the exciton[20].

The same principle can also be applied to negative trions. Negative trions consist of two electrons and one hole. The spin of two electrons are antiparallel at the ground state. Therefore the spin of negative trion is solely determined by the total momentum of heavy hole ($M = \pm 3/2$). For negative trions in NCs with hexagonal crystal structures and/or non-spherical shape, the Zeeman splitting can be written as:

$$\Delta E_{\mathrm{hh}} = -2g\mu_{\mathrm{B}}BM\cos(\theta) \tag{2.23}$$

The transverse component of magnetic field mixes the heavy-hole and light-hole states, and this mixing efficiently accelerates the spin relaxation of negative trions. But this mixing does not affect the recombination dynamics because trions do have dark states and trions with heavy hole and light hole have the same recombination rates.

By contrast, the Zeeman splitting of positive trion is not influenced by the angle between magnetic field and quantization axis because the Zeeman splitting of positive trions is only determined by the electron, and the exchange interaction between an electron and two holes with opposite total momentum is zero, which means the electron spin is not aligned along any axis.

The situation in spherical colloidal NCs with cubic crystal structure is rather simple. Since in such NCs, there is no quantization axis, the Zeeman splitting of exciton complexes is only dependent on the g-factor and magnetic field.

2.5 PL polarization in colloidal nanocrystals

The helicity of PL from colloidal NCs is determined by the spin of exciton complexes. Therefore analysis of the PL circular polarization induced by the external magnetic field is a powerful tool to investigate the spin levels of exciton complexes, to identify their charging state and to obtain information on spin dynamics. The degree of circular polarization (DCP) is defined as:

$$P_{\mathrm{c}}(t) = \frac{I^{+}(t) - I^{-}(t)}{I^{+}(t) + I^{-}(t)} \tag{2.24}$$

Here $I^{+}(t)$ and $I^{-}(t)$ are the σ^{+} and σ^{-} polarized PL intensities, respectively, measured at time delay t after pulsed excitation. Note that in Refs. 25, 60, other definition of P_{c} has been used, namely $P_{\mathrm{c}} = (I^{-} - I^{+})/(I^{-} + I^{+})$, which gives inverted sign for DCP compared to the definition used here. The time-integrated DCP $P_{\mathrm{c}}^{\mathrm{int}}$ can be evaluated by integrating the corresponding PL intensities:

$$P_{\mathrm{c}}^{\mathrm{int}}(B,T) = \frac{\int dt I^{+}(t) - \int dt I^{-}(t)}{\int dt I^{+}(t) + \int dt I^{-}(t)} \tag{2.25}$$

In case of CW excitation the measured polarization degree corresponds to $P_{\mathrm{c}}^{\mathrm{int}}$.

2.5.1 PL polarization in a single NC

Now let us consider how to relate the PL polarization to the spin polarization of exciton complexes in colloidal NCs. Firstly, we consider the spin polarization in a single NC. Figure 2-6 shows the energy level scheme of two Zeeman-split levels of exciton complexes in colloidal NCs in external magnetic field. The recombination dynamics of such system is described by the following rate equations:

$$\frac{dN^{+}}{dt} = -N^{+}(\Gamma + \Gamma^{+}) + N^{-}\Gamma^{-} + G^{+}(t) \tag{2.26}$$

$$\frac{dN^{-}}{dt} = -N^{-}(\Gamma + \Gamma^{-}) + N^{+}\Gamma^{+} + G^{-}(t) \tag{2.27}$$

In the condition of continuous excitation where $G(t) = G_0$, the solution of rate equations for the steady state regime ($dN^{\pm}/dt = 0$) is:

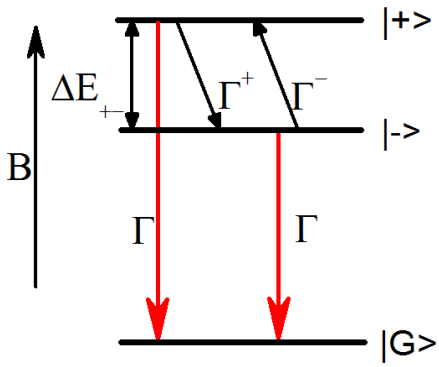

Figure 2-6: Energy level scheme of two Zeeman-split levels of exciton complexes in colloidal NCs in external magnetic field. $|+\rangle$ and $|\text{-}\rangle$ are the higher and lower energy states. $|\text{G}\rangle$ is the ground state. ΔE_{+-} is the Zeeman splitting. Γ^+ and Γ^- are spin relaxation rate from $|+\rangle$ to $|\text{-}\rangle$ and $|\text{-}\rangle$ to $|+\rangle$ respectively. Γ is the recombination rate of excitons at $|+\rangle$ and $|\text{-}\rangle$.

$$\rho = \frac{N^- - N^+}{N^- + N^+} = \rho_0 \frac{\tau}{\tau + \tau_s} \tag{2.28}$$

where

$$\tau_s = 1/(\Gamma^+ + \Gamma^-) \tag{2.29}$$

$$\rho_0 = \frac{\Gamma^+ - \Gamma^-}{\Gamma^+ + \Gamma^-} \tag{2.30}$$

In the condition of short pulse nonresonant excitation where we assume that the short nonresonant excitation of the ground state with δ pulse produces the population of the levels $N^+(t=0) = N^-(t=0) = N_0/2$ and $G(t) = 0$ for $t > 0$, the time evolution of the created population and the rise of the spin polarization are described by

$$\rho(t) = \frac{N^- - N^+}{N^- + N^+} = \rho_0(1 - \exp(-t/\tau_s)) \tag{2.31}$$

The time-integrated DCP P_c^{int}defined by Eq. (2.25) is:

$$\rho_{\text{int}}(B,T) = \frac{\int_0^\infty (N^-(t) - N^+(t))dt}{\int_0^\infty (N^-(t) + N^+(t))dt} = \rho_0 \frac{\tau}{\tau + \tau_s} \tag{2.32}$$

At $t \to \infty$, the population distribution approaches to thermal equilibrium and the polarization saturates. The saturated value of the polarization at $t \to \infty$ is

given by:

$$\rho_\infty = \rho_0 = \frac{\Gamma^+ - \Gamma^-}{\Gamma^+ + \Gamma^-} \tag{2.33}$$

It should be noticed that for dark excitons, the relaxation between two Zeeman-split levels may be realized indirectly through interaction with other exciton sublevels. So rates Γ^+ and Γ^- may correspond not to the one step process but to more complicated processes, but it does not change the conclusions of this consideration as far as we assume that the process leads to the thermal equilibrium.

Since in the thermal equilibrium state, the population distribution of exciton complexes at different energy levels should obey Boltzmann distribution, therefore the spin polarization degree of exciton complexes in two Zeeman-split levels is:

$$\rho_0 = \tanh(\Delta E/2k_\mathrm{B}T) \tag{2.34}$$

ΔE is the Zeeman splitting of exciton complexes. It should be emphasized that as mentioned in Sec. 2.4, in colloidal NCs with hexagonal crystal structures and/or non-spherical shape, the Zeeman splitting of excitons and negative trions is not only determined by magnetic field but also influenced by the angle between the magnetic field and the quantization axis. By contrast, the Zeeman splitting of positive trion is not influenced by the angle between magnetic field and quantization axis.

Now let us consider how to derive PL polarization from spin polarization. For excitons in spherical NCs with cubic crystal structure, the PL polarization is fully determined by the spin polarization of excitons. If we ignore the non-radiative channel, the time-dependent DCP $P_\mathrm{c}(t)$, time-integrated DCP $P_\mathrm{c}^\mathrm{int}$ and thermal equilibrium DCP P_c^eq of PL have the same form as the spin polarization (see also Eqs. (2.31, 2.32 2.34)):

$$P_\mathrm{c}(t) = \rho_0(1 - \exp(-t/\tau_\mathrm{s})) \tag{2.35}$$

$$P_\mathrm{c}^\mathrm{int}(B,T) = \rho_0 \frac{\tau}{\tau + \tau_\mathrm{s}} \tag{2.36}$$

$$P_\mathrm{c}^\mathrm{eq} = \rho_0 \tag{2.37}$$

The PL polarization of excitons in NCs with hexagonal crystal structure and/or non-spherical shape is more complicated. According to the electric dipole approximation and Boltzmann distribution between two Zeeman-split levels, in thermal equilibrium condition, the relative intensity of detected σ^+ and σ^- polarized light from a neutral NC measured along the direction of magnetic field is[25]:

$$I^{\pm} = 1 + x^2 \mp 2x\rho_0(B, x, T) \tag{2.38}$$

where $x = \cos(\theta)$. θ is the angle between the quantization axis and magnetic field. Therefore the thermal equilibrium DCP of a single NC is:

$$P_{\mathrm{c}}^{\mathrm{eq}} = \frac{I^+ - I^-}{I^+ - I^-} = -\frac{2x\rho_0(B, x, T)}{1 + x^2} \tag{2.39}$$

Combining with Eq. (2.31) time-dependent DCP and time-integrated DCP of PL from a single NCs with hexagonal crystal structure and/or non-spherical shape can be obtained:

$$P_{\mathrm{c}}(t) = -\frac{2x\rho_0(B, x, T)(1 - \exp(-t/\tau_{\mathrm{s}}))}{1 + x^2} \tag{2.40}$$

$$P_{\mathrm{c}}^{\mathrm{int}}(B, T) = -\frac{2x\rho_0(B, x, T)\frac{\tau}{\tau+\tau_{\mathrm{s}}}}{1 + x^2} \tag{2.41}$$

The resulting equation is also applicable for the PL polarization degree of negative trions. The only difference is that in the case of negative trion we are dealing with the Zeeman splitting of the heavy-hole state instead of the Zeeman splitting of the exciton.

It can be seen that the angle between magnetic field and quantization axis of a NC plays a key role in the measurement of the PL polarization. This angle not only influences the Zeeman splitting that determines the spin polarization, but also modifies the finally detected PL polarization, which means the measured PL polarization degree is different from the spin polarization degree in the case of $|\theta| \neq 0, \pi/2$.

2.5.2 PL polarization in an ensemble of NCs

The PL polarization of excitons in an ensemble of spherical cubic colloidal NCs has the same form as that of a single NC (see Eqs. (2.35, 2.36, 2.37)). To calculate the PL polarization of excitons in an ensemble of randomly oriented NCs with hexagonal crystal structure and/or non-spherical shape, one has to take into account the influence of θ, the angle between magnetic field and the quantization axis. In an ensemble of NCs, the quantization axis is randomly oriented with respect to the magnetic field, therefore θ varies from 0 to $\pi/2$. The time-dependent DCP, time-integrated DCP and thermal equilibrium DCP of excitons in an ensemble of randomly oriented NCs with hexagonal crystal structure and/or non-spherical

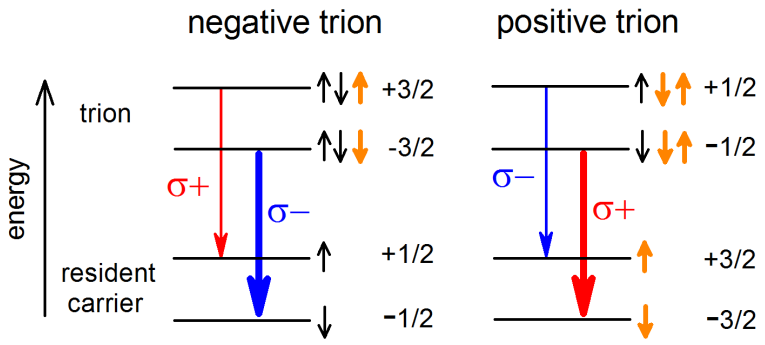

Figure 2-7: Schematic presentation of the spin level structure and the optical transitions between these levels for negative and positive trions in an external magnetic field. Short black and orange arrows indicate electron and hole spins, respectively. Polarized optical transitions are shown by red (σ^+) and blue (σ^-) arrows. The more intense emission, shown by thicker arrow, comes from the lowest in energy trion state with spin $-3/2$ for the negative trion and with spin $-1/2$ for the positive trion.

shape can be obtained by integrating Eqs. (2.40, 2.41, 2.39) over all angles:

$$P_{\rm c}(t) = -\frac{\int_0^1 2x\rho_0(B,x,T)(1-\exp(-t/\tau_{\rm s}))dx}{\int_0^1(1+x^2)dx} \tag{2.42}$$

$$P_{\rm c}^{\rm int}(B,T) = -\frac{\int_0^1 2x\rho_0(B,x,T)\frac{\tau}{\tau+\tau_{\rm s}}dx}{\int_0^1(1+x^2)dx} \tag{2.43}$$

$$P_{\rm c}^{\rm eq}(B,T) = -\frac{\int_0^1 2x\rho_0(B,x,T)dx}{\int_0^1(1+x^2)dx} \tag{2.44}$$

Next, let us discuss PL polarization of trions in colloidal NCs with hexagonal crystal structure and/or nonspherical shape. The spin structure of negative and positive trions in CdSe/CdS NCs subject to a magnetic field is shown in Fig. 2-7. The external magnetic field lifts the spin degeneracy of an unpaired hole or electron in the negative and positive trion, respectively. The ground state of the positive trion has spin projection, $s_{\rm z} = -1/2$, on the magnetic field direction, because in CdSe NCs the electron g-factor, $g_{\rm e}$, is positive and the electron spin level energies are given by $E_{\rm e} = s_{\rm z} g_{\rm e} \mu_{\rm B} B$.

The ground state of the negative trion consists of two electrons in a singlet state and a hole with momentum projection $M = \pm 3/2$ onto the quantization axis. Its spin level energy is strongly anisotropic and can be described as $E_{\rm hh} = -M g_{\rm h} \mu_{\rm B} B \cos\theta$, where $g_{\rm h}$ is the hole g-factor, $\theta \in [0;\pi/2]$ and $\cos\theta \geq 0$[20,61]. Since the hole g-factor is negative[20,62] in CdSe NCs, the lowest hole spin sublevel

in magnetic field has momentum projection $-3/2$ (see Fig. 2-7).

After trion decay, the remaining resident carrier occupies one of its spin sublevels. The spin allowed optical transitions between the trion and resident carrier spin sublevels are shown by arrows in Fig. 2-7. σ^+ polarized photon emission is connected with transitions, which changes the spin projection by $+1$ (red arrows), and σ^- polarized photons result from transitions, which changes the spin projection by -1 (blue arrows). At low temperatures, when $k_\mathrm{B}T$ is smaller than the trion Zeeman splitting, stronger emission intensity arises from the energetically lowest trion state.

Next, we only consider negatively charged NCs. In this equilibrium, the trion spin polarization along the NC quantization axis, M^eq, is given by $M^\mathrm{eq}(B,\theta,T) = -(3/2)(N_{-3/2} - N_{3/2})/(N_{-3/2} + N_{3/2}) = -(3/2)\rho_0(B,x,T)$, where $x = \cos(\theta)$ and

$$\rho_0(B,x,T) = \tanh\left(\frac{\Delta E_\mathrm{hh}(B,\theta)}{2k_\mathrm{B}T}\right) \tag{2.45}$$

Here $\Delta E_\mathrm{hh}(B,\theta) = -3g_\mathrm{h}\mu_\mathrm{B}B\cos\theta$ is the trion Zeeman splitting determined by the Zeeman splitting of the heavy hole in the trion. In the randomly oriented NC ensemble the value of the Zeeman splitting depends on the angle θ between quantization axis and magnetic field direction. This results in different M^eq in differently oriented NCs. In turn, the contribution of the individual NCs to the ensemble polarization also depends on the angle θ[20,61]. The ensemble equilibrium PL polarization P_c^eq is obtained from averaging over all possible orientations of the NCs.

After short pulse unpolarized excitation, the polarization dynamics in each NC can be described by $M(B,\theta,T,t) = -(3/2)\rho(B,x,T,t)$, where

$$\rho(B,x,T,t) = \rho_0(B,x,T)\left(1 - \exp\left(-\frac{t}{\tau_\mathrm{s}(B,x,T)}\right)\right) \tag{2.46}$$

Here τ_s is the spin relaxation time, which depends on temperature, external magnetic field and the angle θ. For negative trions τ_s describes the spin-flips of the hole with $M = \pm 3/2$, as seen from Fig. 2-7. From Eq. (2.46) it is clear that $\rho(t) \longrightarrow \rho_0$ and $M(B,\theta,t) \longrightarrow M^\mathrm{eq}(B,\theta)$ for $t \gg \tau_\mathrm{s}$. Consequently the ensemble average value $P_\mathrm{c}^\mathrm{eq}(B)$ can be taken from experiment as saturation value of the time-dependent DCP: $P_\mathrm{c}^\mathrm{eq}(B) = P_\mathrm{c}(B, t \to \infty)$.

The PL polarization arises from the difference in the populations of the two lowest spin sublevels of the negatively charged trion with momentum projection $M = +3/2$ and $M = -3/2$ on the quantization axis that are split by the external magnetic field leads to the PL polarization. The DCP in thermal equilibrium of the negative trions PL from an ensemble of randomly oriented NCs can be obtained by integrating a single negatively charged NC (see Eq. (2.41)) over all

NC orientations:

$$P_{\mathrm{c}}^{\mathrm{eq}}(B,T) = -\frac{\int_0^1 2x\rho_0(B,x,T)dx}{\int_0^1(1+x^2)dx} \tag{2.47}$$

In thermal equilibrium, the DCP depends only on Zeeman splitting and temperature, but does not depend on the spin relaxation time, as one can see from Eq. (2.47). To describe the time-dependent ensemble polarization $P_{\mathrm{c}}(B,T,t)$ and the time-integrated ensemble polarization $P_{\mathrm{c}}^{\mathrm{int}}(B,T)$ spin relaxation should be taken into account.

By integrating the time-resolved DCP of a single negatively charged NCs (see Eq. (2.40)) the time-dependent DCP in the ensemble of randomly oriented NCs can be obtained:

$$P_{\mathrm{c}}(B,T,t) = -\frac{\int_0^1 2x\rho(B,x,T,t)dx}{\int_0^1(1+x^2)dx} \tag{2.48}$$

where $\rho(B,x,T,t)$ is given by Eq. (2.46). Obviously the time-dependent DCP of the negative trion in individual NCs is controlled not only by the trion equilibrium polarization, $M^{\mathrm{eq}} \propto \rho_0(B,x,T)$, but also by the spin relaxation time $\tau_{\mathrm{s}}(B,x,T)$.

Using the time-dependent DCP of trion a negatively charged NC (see Eq. (2.41)), time-integrated circular polarization degree for an ensemble of randomly oriented NCs can be obtained:

$$P_{\mathrm{c}}^{\mathrm{int}}(B,T) = -\frac{\int_0^1 2x\rho_{\mathrm{s}}(B,x,T)dx}{\int_0^1(1+x^2)dx} \tag{2.49}$$

where

$$\rho_{\mathrm{s}}(B,x,T) = \rho_0(B,x,T)\frac{\tau_{\mathrm{r}}}{\tau_{\mathrm{s}}(B,x,T)+\tau_{\mathrm{r}}} \tag{2.50}$$

It should be noticed that the theory about the PL polarization degree of an ensemble of randomly oriented negatively charged colloidal NCs is newly developed.

2.6 Spin relaxation of negative trions in thick-shell CdSe/CdS NCs

The spin relaxation process of exciton complexes is the process in which exciton complexes flip the spin from one state to another. The spin relaxation can be realized through various channels, such as hyperfine interaction, spin-orbit interaction and carrier-lattice (or phonons) interaction[63]. Here we focus on the spin relaxation mechanism of negative trions between two Zeeman-split levels in thick-shell CdSe/CdS colloidal NCs. The spin of negative trion is determined by the total momentum of heavy hole ($M = \pm 3/2$). Figure 2-8 illustrates the spin relaxation

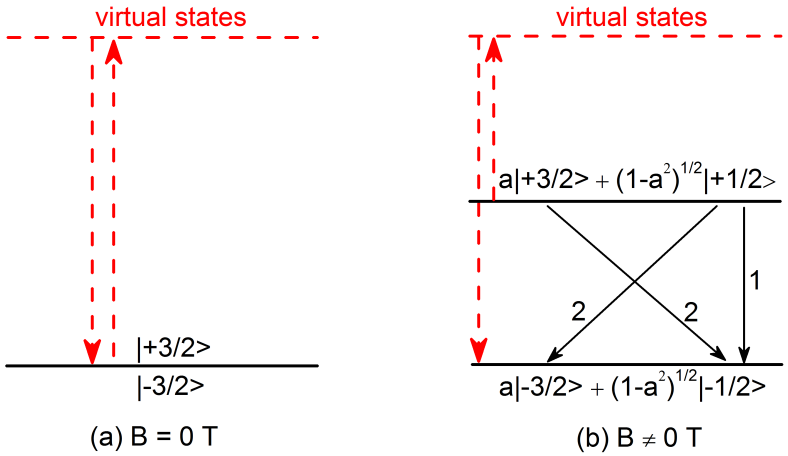

Figure 2-8: Schematics of spin relaxation of negative trions between two Zeeman-split levels in thick-shell CdSe/CdS at (a) $B = 0$ T and (b) $B \neq 0$ T. B is the external magnetic field.

mechanism of negative trions in thick-shell CdSe/CdS NCs. In zero magnetic field, the two trion states $|+3/2\rangle$ and $|-3/2\rangle$ are degenerated. The difference of the spin between these two states is 3. According to the conservation law of total momentum, to flip the spin from $+3/2$ to -3/2, the difference of the spin 3 has to be compensated. One possible way is to flip the spin with the assistant of phonons which can take away some angular momentum. The total momentum of phonons in a confined system can be 0, 1, 2, 3 or even more. However, the phonon with angular momentum of 3 does not couple with heavy holes[64]. Therefore, one-phonon assisted spin flip is forbidden at 0 T. But two-phonon-assisted spin relaxation via virtual states is possible (see red arrows in Fig. 2-8(a)). The negative trion can jump to a virtual state by absorbing a phonon with total momentum of 1 or 2, and then relaxes back by emitting a phonon with angular momentum of 2 or 1.

In an external magnetic field, the relaxation mechanism of negative trions in thick-shell CdSe/CdS colloidal NCs is controlled by the mixing of the heavy-hole states $M = \pm 3/2$ with light-hole states $M = \pm 1/2$, induced by the component of the magnetic field perpendicular to the NC quantization axis (see Fig. 2-8(b)). The mixing between heavy-hole and light-hole states accelerates the spin relaxation in two ways. Firstly, this admixture reduces the difference between momenta of the initial and final states from ± 3 to ± 1 or ± 2. This difference in angular momentum conservation required for the spin-flip transition can be satisfied by emitting and absorbing phonons with angular momenta 1 or 2. These phonons are coupled with the $M = \pm 1/2, \pm 3/2$ hole states[64]. Secondly, two-phonon-assisted spin relaxation is accelerate because now negative trions can involve phonons with angular momentum of 0 in the virtual transition. The mixing matrix element $V_{\pm 3/2,\pm 1/2} \propto B \sin\theta$, as shown in Ref. 20. As a result, the probability of virtual transitions between $\pm 1/2$ and $\pm 3/2$ states is proportional to $|V_{\pm 3/2,\pm 1/2}|^2/\Delta_{\mathrm{LH}}^2 \propto B^2(1-x^2)$, where Δ_{LH} is the splitting between the heavy-hole and light-hole states.

The theory is specifically developed for colloidal NCs.

According to this suggestion the spin relaxation rate of negative trions between two Zeeman-split levels can be written as

$$\frac{1}{\tau_{\mathrm{s}}(B,x,T)} = \frac{1}{\tau_{\mathrm{s0}}(T)} + \alpha(T)B^2(1-x^2) \tag{2.51}$$

where $\tau_{\mathrm{s0}}(T)$ which is independent on magnetic field is the spin relaxation time between the $M = \pm 3/2$ and $M = \mp 3/2$ hole states in zero magnetic field. $\alpha(T)$ is the coefficient that describes the phonon-assisted mechanism, that flips a hole from the virtual $\pm 1/2$ intermediate state to the $\mp 3/2$ second sublevel of the ground state, which allows to conserve the momentum during spin flip process. It should be stressed that this theory is newly developed specifically for negative charged thick-shell CdSe/CdS colloidal NCs.

2.7 Non-radiative energy transfer process in an ensemble of NCs

Energy can be transferred non-radiatively between closely-packed colloidal NCs. This can be the Förster process due to the dipole-dipole interaction or other process involving the higher oder multipoles (like Dexter process). However, the dipole-dipole interaction if allowed is stronger and the observed effect of the temperature and magnetic field on the energy transfer supports the assumption about the dipole-dipole mechanism[48,50,60]. In this section we present A. V. Rodina's theoretical model which describes the recombination dynamics in acceptor NCs and allows to extract the energy transfer rate Γ_{ET} from the experimental data. It should be emphasized that this model is general for any resonant non-radiative energy transfer process.

Let us consider an ensemble of closely-packed colloidal NCs. Larger NCs emitting at the energy E_{a} at the low energy side of the PL band play mostly the role of the acceptor NCs. Smaller NCs emitting at the energy $E_{\mathrm{d}} > E_{\mathrm{a}} + E_{\mathrm{da}}$ may play a role of the donor NCs for the chosen acceptor if there is nonzero overlap between donor PL spectrum and acceptor absorption spectrum. Therefore the minimum energy distance E_{da} should be not smaller than the Stokes shift in the acceptor NC and is considered as the parameter of the model.

The energy transfer process between donor NC with energy E_{d} and acceptor NC with energy E_{a} is shown schematically in Fig. 2-9 This process can be described by rate equations for the evolution of donor N_{d} and acceptor N_{a} population with time. We will assume the model of bright (optically-allowed $|\mathrm{A}\rangle$ state) and dark (optically-forbidden $|\mathrm{F}\rangle$ state) exciton states with energy splitting ΔE_{AF} for both donor and acceptor NCs and population $N_{\mathrm{d,a}} = N^{\mathrm{A}}_{\mathrm{d,a}} + N^{\mathrm{F}}_{\mathrm{d,a}}$. We assume that

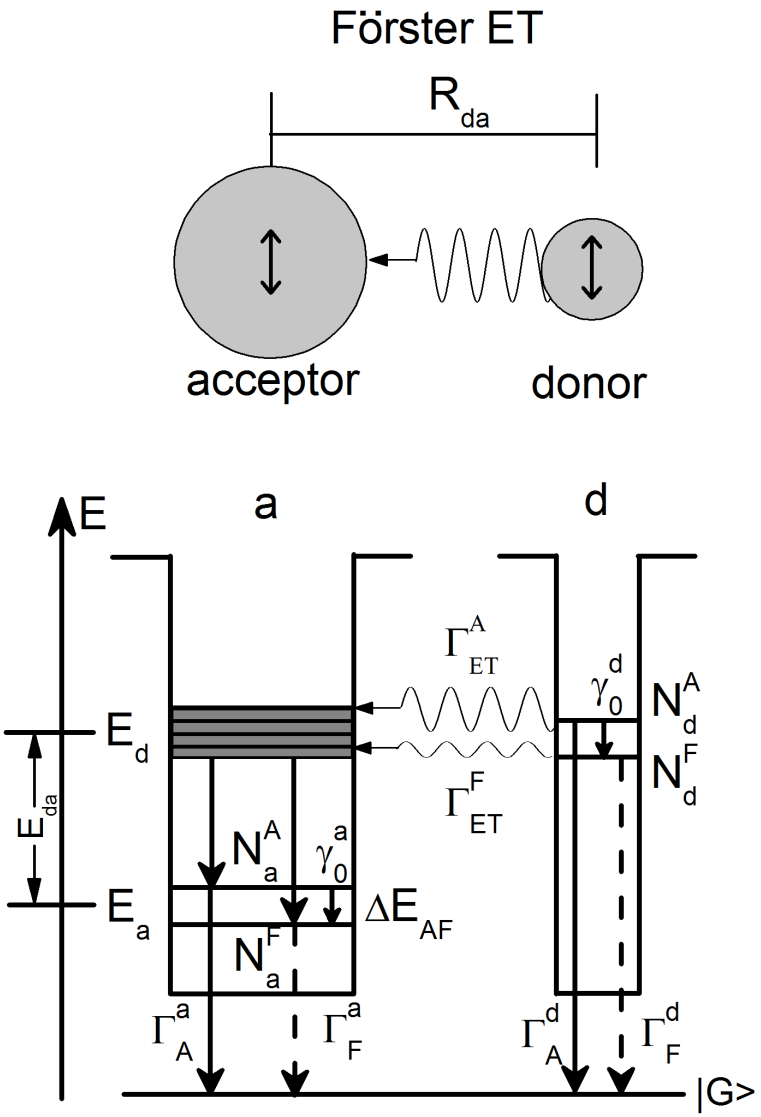

Figure 2-9: Schematic of the energy transfer process between donor NC with energy E_{d} and acceptor NC with energy E_{a}.

first initial excitation of the NC happens at the excited level from which excitons relax very fast (instantly) to populate $|\mathrm{A}\rangle$ and $|\mathrm{F}\rangle$ states in equal proportion. During the energy transfer process the same fraction f of population from both bright $fN_{\mathrm{d}}^{\mathrm{A}}$ and dark $fN_{\mathrm{d}}^{\mathrm{F}}$ exciton states of the donor NC is transfered resonantly to some excited level of the acceptor NC which lays by energy $E_{\mathrm{da}} \gg \Delta E_{\mathrm{AF}}$ above the lowest bright and dark exciton level of acceptor NC. Then the fast energy relaxation from the excited state leads to the increase of the $N_{\mathrm{a}}^{\mathrm{A}}$ and $N_{\mathrm{a}}^{\mathrm{F}}$ populations in equal proportion. The evolution of the donor and acceptor NC populations can be described by the following rate equations:

$$\frac{dN_{\mathrm{d}}^{\mathrm{A}}}{dt} = -N_{\mathrm{d}}^{\mathrm{A}}(\Gamma_{\mathrm{A}}^{\mathrm{d}} + \gamma_0^d + \gamma_{\mathrm{th}}^d + \Gamma_{\mathrm{ET}}^{\mathrm{A}}) + N_{\mathrm{d}}^{\mathrm{F}}\gamma_{\mathrm{th}}^d \tag{2.52}$$

$$\frac{dN_{\mathrm{d}}^{\mathrm{F}}}{dt} = -N_{\mathrm{d}}^{\mathrm{F}}(\Gamma_{\mathrm{F}}^{\mathrm{d}} + \gamma_{\mathrm{th}}^d + \Gamma_{\mathrm{ET}}^{\mathrm{F}}) + N_{\mathrm{d}}^{\mathrm{A}}(\gamma_0^{\mathrm{d}} + \gamma_{\mathrm{th}}^d) \tag{2.53}$$

and

$$\frac{dN_{\mathrm{a}}^{\mathrm{A}}}{dt} = -N_{\mathrm{a}}^{\mathrm{A}}(\Gamma_{\mathrm{A}}^{\mathrm{A}} + \gamma_0^a + \gamma_{\mathrm{th}}^a) + N_{\mathrm{A}}^{\mathrm{F}}\gamma_{\mathrm{th}}^a + 0.5f(N_{\mathrm{d}}^{\mathrm{A}}\Gamma_{\mathrm{ET}}^{\mathrm{A}} + N_{\mathrm{d}}^{\mathrm{F}}\Gamma_{\mathrm{ET}}^{\mathrm{F}}) \tag{2.54}$$

$$\frac{dN_{\mathrm{a}}^{\mathrm{F}}}{dt} = -N_{\mathrm{a}}^{\mathrm{F}}(\Gamma_{\mathrm{F}}^{\mathrm{A}} + \gamma_{\mathrm{th}}^a) + N^{\mathrm{A}}(\gamma_0^{\mathrm{d}} + \gamma_{\mathrm{th}}^a) + 0.5f(N_{\mathrm{d}}^{\mathrm{A}}\Gamma_{\mathrm{ET}}^{\mathrm{A}} + N_{\mathrm{d}}^{\mathrm{F}}\Gamma_{\mathrm{ET}}^{\mathrm{F}}) \tag{2.55}$$

Here $\Gamma_{\mathrm{A}}^{\mathrm{d,a}}$ and $\Gamma_{\mathrm{F}}^{\mathrm{d,a}}$ are the recombination rates (including radiative and non-radiative recombination) of the bright and dark excitons, respectively. In the analysis below we assume them to be the same for donor and acceptor NCs and omit the respective upper indexes. The same we apply to the relaxation rates from bright to dark-exciton states at zero temperature $\gamma_0^{\mathrm{d}} = g_0^{\mathrm{A}} = \gamma_0$ and to $g_{\mathrm{th}}^{\mathrm{d,a}} = g_0^{\mathrm{d,a}}/(\exp(\Delta E_{\mathrm{AF}}/k_{\mathrm{B}}T) - 1) = g_{\mathrm{th}}$ which describes the thermal mixing of bright and dark excitons in the case of the one phonon process. The rates $\Gamma_{\mathrm{ET}}^{\mathrm{A}}$ and $\Gamma_{\mathrm{ET}}^{\mathrm{F}}$ describe the energy transfer from bright- and dark-exciton states of donor NCs. In the case of the dipole-dipole Förster energy transfer, the nonzero energy transfer rate $\Gamma_{\mathrm{ET}}^{\mathrm{F}}$ from the dark-exciton state is possible due to the admixture of the bright to dark state, therefor one may expect the approximate relation $\Gamma_{\mathrm{ET}}^{\mathrm{F}}/\Gamma_{\mathrm{ET}}^{\mathrm{A}} \approx \Gamma_{\mathrm{F}}^{\mathrm{rad}}/\Gamma_{\mathrm{A}}^{\mathrm{rad}}$, where $\Gamma_{\mathrm{A,F}}^{\mathrm{rad}}$ are respective radiative recombination rates of the bright and dark excitons.

Rate equation Eq. (2.53) describe the time evolution of donor population fraction $N_{\mathrm{d}}^{(f)} = fN_{\mathrm{d}}$ participating in the energy transfer as well as the fraction $N_{\mathrm{d}}^{(1-f)} = (1-f)N_{\mathrm{d}}$ which does not participate. For the last case one has to assume $\Gamma_{\mathrm{ET}}^{\mathrm{A}} = \Gamma_{\mathrm{ET}}^{\mathrm{F}} = 0$. The rate equations should be completed by the initial conditions at $t = 0$:

$$N_{\mathrm{d}}^{A}(0) = N_{\mathrm{d}}^{\mathrm{F}}(0) = N_{\mathrm{d}}^{0}/2 \tag{2.56}$$

$$N_{\mathrm{a}}^{A}(0) = N_{\mathrm{a}}^{\mathrm{F}}(0) = N_{\mathrm{a}}^{0}/2 \tag{2.57}$$

While for each particular NC the initial number of created excitons is 1, the introduced N_{a}^0 and N_{d}^0 reflect the total number of the NCs emitting at the respective energies E_{a} and E_{d}. At the limit cases of low temperatures (when approximation $g_{\mathrm{th}} = 0$ is valid) and large temperatures (when approximation $N_{\mathrm{a,d}}^{\mathrm{A}} = N_{\mathrm{a,d}}^{\mathrm{F}}$ is valid) the analytical solutions for these rate equations can be easily obtained:

$$N_{\mathrm{d}}^{\mathrm{A}}(t) = (N_{\mathrm{d}}^0/2)\exp(-t/\tau_{\mathrm{d}}^{\mathrm{A}}) \tag{2.58}$$

$$N_{\mathrm{d}}^{\mathrm{F}}(t) = -(N_{\mathrm{d}}^0/2)(g_0^{\mathrm{d}}/g^*)\exp(-t/\tau_{\mathrm{d}}^{\mathrm{A}}) + (N_{\mathrm{d}}^0/2)(1 + (g_0^{\mathrm{d}}/g_{\mathrm{d}}^*))\exp(-t/\tau_{\mathrm{d}}^{\mathrm{F}}) \tag{2.59}$$

where

$$\frac{1}{\tau_{\mathrm{d}}^{\mathrm{A}}} = g_{\mathrm{A}} + g_0^{\mathrm{d}} + g_{\mathrm{ET}}^{\mathrm{A}} \tag{2.60}$$

$$\frac{1}{\tau_{\mathrm{d}}^{\mathrm{F}}} = g_{\mathrm{F}} + g_{\mathrm{ET}}^{\mathrm{F}} \tag{2.61}$$

$$g_{\mathrm{d}}^* = 1/\tau_{\mathrm{d}}^{\mathrm{A}} - 1/\tau_{\mathrm{d}}^{\mathrm{F}} \tag{2.62}$$

These solutions are also valid for the NCs that do not participate in energy transfer process if one put $g_{\mathrm{ET}}^{\mathrm{A}} = g_{\mathrm{ET}}^{\mathrm{F}} = 0$. So comparing the life times determined by fitting at the high energy side one can estimate all parameters. For the acceptor NCs we obtain:

$$N_{\mathrm{a}}^{\mathrm{A}}(t) = A_1\exp(-t/\tau_{\mathrm{a}}^{\mathrm{A}}) + A_2\exp(-t/\tau_{\mathrm{d}}^{\mathrm{A}}) + A_3\exp(-t/\tau_{\mathrm{d}}^{\mathrm{F}}) \tag{2.63}$$

$$N_{\mathrm{d}}^{\mathrm{F}}(t) = F_1\exp(-t/\tau_{\mathrm{a}}^{\mathrm{A}}) + F_2\exp(-t/\tau_{\mathrm{d}}^{\mathrm{A}}) + F_3\exp(-t/\tau_{\mathrm{d}}^{\mathrm{F}}) + F_4\exp(-t/\tau_{\mathrm{a}}^{\mathrm{F}}) \tag{2.64}$$

where

$$\frac{1}{\tau_{\mathrm{a}}^{\mathrm{A}}} = g_{\mathrm{A}} + g_0^{\mathrm{A}} \tag{2.65}$$

$$\frac{1}{\tau_{\mathrm{a}}^{\mathrm{F}}} = g_{\mathrm{F}} \tag{2.66}$$

and amplitudes A_i and F_i can be found from equations and initial conditions.

The PL intensity from donor NC $I_{\mathrm{d}}(E_{\mathrm{d}}, t)$ and acceptor NC $I_{\mathrm{a}}(E_{\mathrm{a}}, t)$ is given by

$$I_{\mathrm{d}}(E_{\mathrm{d}}, t) = I_{\mathrm{d}}^{(f)}(E_{\mathrm{d}}, t) + I_{\mathrm{d}}^{(1-f)}(E_{\mathrm{d}}, t) \tag{2.67}$$

$$I_{\mathrm{d}}^{(i)}(E_{\mathrm{d}}, t) = \eta_{\mathrm{A}}\Gamma_{\mathrm{A}}N_{\mathrm{d}}^{A,(i)} + \eta_{\mathrm{F}}\Gamma_{\mathrm{F}}N_{\mathrm{d}}^{F,(i)} \tag{2.68}$$

$$I_{\mathrm{a}}(E_{\mathrm{a}}, t) = \eta_{\mathrm{A}}\Gamma_{\mathrm{A}}N_{\mathrm{a}}^{\mathrm{A}} + \eta_{\mathrm{F}}\Gamma_{\mathrm{F}}N_{\mathrm{a}}^{\mathrm{F}} \tag{2.69}$$

where $\eta_{\mathrm{A,F}} = \Gamma_{\mathrm{A,F}}^{\mathrm{rad}}/\Gamma_{\mathrm{A,F}}$ gives the radiative quantum efficiency of the bright- and

dark-exciton states.

In order to take into account the contribution of all donor NCs into the acceptor PL $I_{\mathrm{a}}(E_{\mathrm{a}}, t)$ one has to replace the last term in Eq. (2.55) describing the energy transfer related feeding by

$$0.5 \int_{E_{\mathrm{a}}+E_{\mathrm{da}}}^{+\infty} f(E) \left(N_{\mathrm{d}}^{\mathrm{A}}(E) \Gamma_{\mathrm{ET}}^{\mathrm{A}}(E) + N_{\mathrm{d}}^{\mathrm{F}}(E) \Gamma_{\mathrm{ET}}^{\mathrm{F}}(E) \right) dE.$$

The consideration can be considerably simplified if one assumes that energy transfer rates $\Gamma_{\mathrm{ET}}^{\mathrm{A,F}}$ and the fraction f are the same for all donor NCs similar to the already used approximation of the constant recombination rates $\Gamma_{\mathrm{A,F}}$ and relaxation rate γ_0 over the spectrum. With this assumption, the Eqs. (2.53, 2.55) can be solved without any modification while the initial conditions at $t = 0$ of Eq. (2.57) should be completed by an additional constrain:

$$N_{\mathrm{d}}^{0} = r_0 N_{\mathrm{a}}^{0} \tag{2.70}$$

$$r_0 = \frac{\int_{E_{\mathrm{a}}+E_{\mathrm{da}}}^{+\infty} \mathrm{Exp}\left[-(E-E_0)^2/(2\sigma^2)\right] dE}{\mathrm{Exp}[-(E_{\mathrm{a}}-E_0)^2/(2\sigma^2)]} \tag{2.71}$$

Here parameter r_0 gives the ratio of the total number of the NCs with energy $E_{\mathrm{a}} + E_{\mathrm{da}}$ to the number of the NCs with fixed energy E_{a}.

Chapter 3

Samples and experimental techniques

This chapter describes the samples and experimental techniques used in the study of colloidal nanostructures. Our study on colloidal nanostructures was started from the magneto-photoluminescence (PL) of colloidal nanocrystals (NCs) measured using polarization-resolved magneto-PL technique. From the PL polarization degree evaluated according to the polarization-resolved magneto-PL, the g-factor of exciton complexes can be estimated. However, this stationary technique does not directly reveal any information about dynamical processes, such as the decay of exciton PL, spin relaxation processes and Förster resonant energy transfer (FRET) process. In order to explore such kinds of dynamical processes, polarization-resolved PL decay technique was adopted. In addition, to comprehensively understand the optical properties of colloidal nanocrystals, the fluorescence line narrowing technique was employed to characterize exciton fine structures and optically-induced spin orientations. In the following, the samples studied will be presented first, and then these three experimental techniques will be described.

3.1 Samples

Colloidal semiconductor nanostructures are synthesized using wet chemical method in which colloidal nanostructures are self-assembled in a solvent heated up to sufficiently high temperature[9,10]. Properties of colloidal nanostructures are dependent on the material, size and shape. To explore how these factors influence properties of colloidal nanostructures, a systematic study was performed on a variety of samples listed in Table 3-1.

Sample #1 to #7 have a core/shell structure, namely a spherical CdSe core is covered by several CdS layers. In the following chapters we refer to them as "C/S", where C is the CdSe core radius and S the CdS shell thickness, both in

sample	material	structure	parameters (nm)
#1	CdSe/CdS	core (w)/shell (w) NC	core/shell 2.5/2
#2	CdSe/CdS	core (c)/shell (w) NC	core/shell 2.5/2
#3	CdSe/CdS	core (c)/shell (w) NC	core/shell 2.5/3
#4	CdSe/CdS	core (c)/shell (w) NC	core/shell 2.5/4
#5	CdSe/CdS	core (c)/shell (w) NC	core/shell 2.5/5
#6	CdSe/CdS	core (c)/shell (w) NC	core/shell 2.5/7
#7	CdSe/CdS	core (c)/shell (w) NC	core/shell 2.5/10
#8	CdTe	Thoil-capped NC (c)	core: 2.3
#9	CdTe	Thoil-capped NC (c)	core: 3.4
#10	CdTe	Thoil-capped NC (c)	core: 3.7
#11	CdSe/CdS	dot in plate (w)	core: 2.5, plate size: 100
#12	CdSe	nanoplatelet (w)	thickness: 1.9, size: 100
#13	CdSe	nanoplatelet (w)	thickness: 2.2, size: 100

Table 3-1: Parameters of studied samples. (w) and (c) in the structure column denote wurtzite and cubic crystal structures respectively.

nanometers. The valence band offset of the core/shell CdSe/CdS NC sample is around 400 meV. The conduction band offset is around -50 meV at T =200 K and decreases with the decrease of temperature. These samples were provided by Laboratoire de Physique et d'Etude des Matériaux, CNRS. Sample #8 to #10 are CdTe cores capped by Thoil. These samples were provided by Photonics and Optoelectronics Group, CeNS, Ludwig-Maximilians-Universität München. Sample #11 has a dot-in-plate structure where a zero-dimensional spherical CdSe core is embedded in a two-dimensional CdS plate with a width of around 100 nm. Sample #12 and #13 have a quasi-two-dimensional structure. The thickness of these samples is rather small (few nanometers) compared with their lateral width (around 100 nm). Sample #11 to #13 are also from Laboratoire de Physique et d'Etude des Matériaux, CNRS.

Optical properties of colloidal nanostructures are greatly influenced by the surface. The exposure of the ideal fresh sample to air should be prevented because the surface of colloidal nanostructures can be oxidized. Also, colloidal nanostrucutres can conjugate to big clusters, therefore the surface oxidation plus the conjugation effect can ruin the optical properties of colloidal nanostructures. For example, the DCP of old samples can be much lower than that of fresh samples and is no longer dependent on the temperature. Moreover, illuminate the sample with white light source for at least 60 minutes before the measurement. If the sample is kept in dark at room temperature for a long time, some charge carriers can be trapped by defects on the surface of colloidal nanostructures and, consequently, lower the quantum yield due to the Auger process. By illuminating the sample with a white light source, trapped charge carriers are released from surface traps. Additionally, if possible, excite the sample with a pulsed laser. The PL intensity of colloidal

nanostructures can decrease in time when illuminated by a CW laser. This is a problem especially for the polarization-resolved magneto-PL measurement introduced in Sec. 3.2, because the measurement of σ^+ and σ^- polarized PL at the same magnetic field is performed at different time (time interval $>$ 60 minutes). This problem can be solved by exciting the sample with a pulsed laser.

3.2 Polarization-resolved magneto-PL technique

The exciton g-factor reflects the band structure of colloidal nanostructures. Its value characterizes the energy splitting of exciton complexes subjected to an external magnetic field, and from the sign of the g-factor one may deduce the type of the exciton[65,66]. The g-factor of an exciton complex can be evaluated from the PL polarization degree (see Sec. 2.5) measured by polarization-resolved magneto-PL technique.

The schematic of the experimental setup for polarization-resolved magneto-PL measurement is shown in Fig. 3-1. The sample was mounted in Faraday geometry (external magnetic field B perpendicular to the quartz plate and parallel to the light wave vector) in the core of a superconducting solenoid generating magnetic fields up to 15 T (see area in the green rectangular). The sample chamber was immersed in a liquid helium bath. Thermal contact between the sample and liquid helium was established by filling the sample chamber with helium gas (pressure of about 0.1 bar). By heating the sample chamber with a resistor, the temperature at the sample position can be varied from $T = 2.4$ up to 20 K. A higher temperature (up to 300 K) could be achieved by reducing the helium gas pressure.

For polarization-resolved magneto-PL measurements, the PL was excited via a multimode optical fiber, using a continuous wave (CW) diode laser with a photon energy of 3.33 eV, and collected through a detection fiber. The excitation laser is unpolarized. A circular polarizer (the combination of linear polarizer and $\lambda/4$ plate) inserted between the sample and the detection fiber allowed us to detect σ^+ and σ^- polarized PL by alternating the magnetic field direction. The collected signal was dispersed with a 0.55 m spectrometer (model: JOBIN YVON SPEX, TRIAX 550) equipped with three gratings (grating #1: 600 lines/mm, grating #2: 900 lines/mm and grating #3: 2400 lines/mm) and detected by a liquid-nitrogen-cooled charge-coupled device (CCD) camera (model: JOBIN YVON SPEX, CCD 3500) (see the area in dashed green rectangular).

3.3 Polarization-resolved PL decay technique

Polarization-resolved PL decay technique can be used to study various dynamical processes, such as radiative decay process, spin relaxation process and Förster

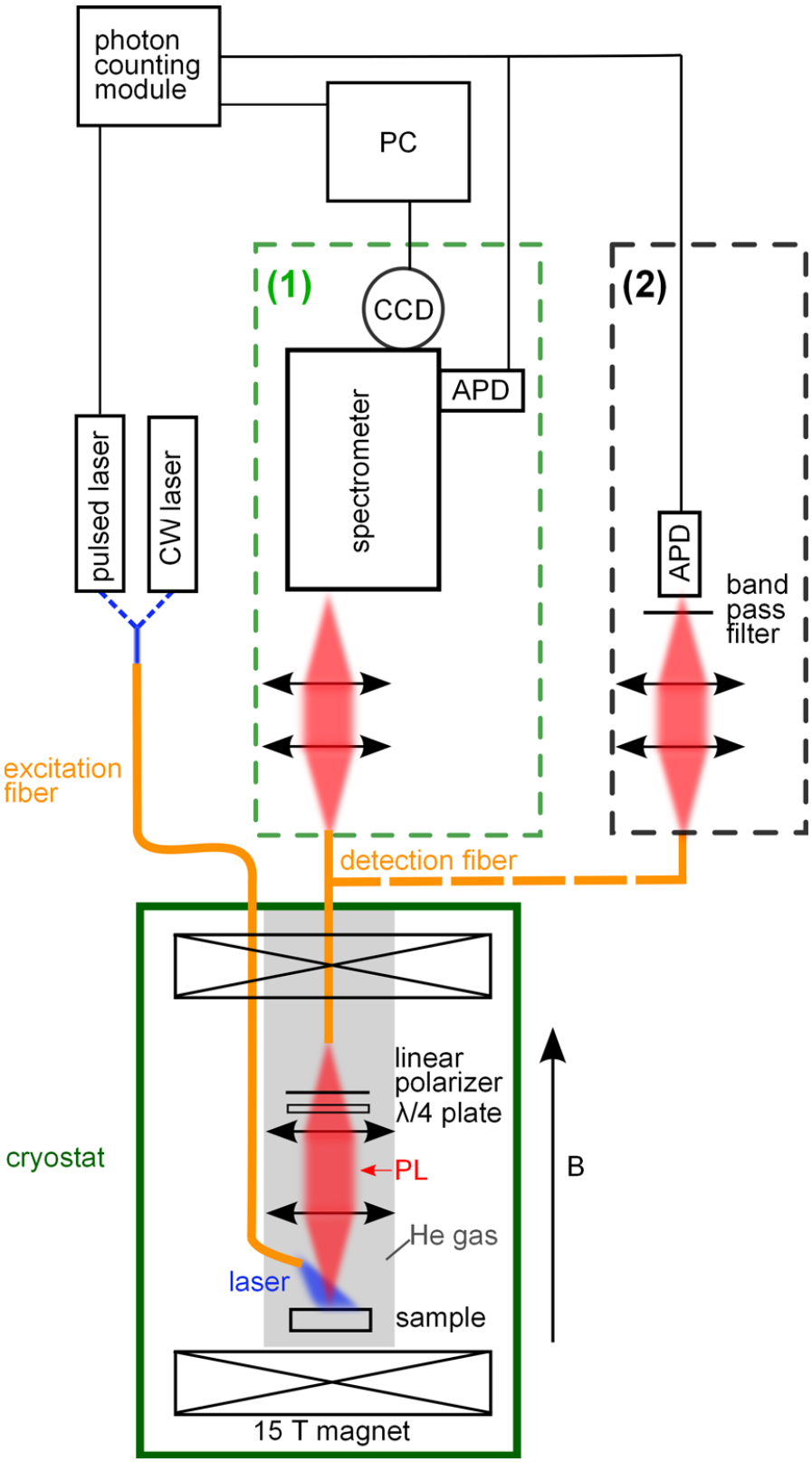

Figure 3-1: The experimental setup for the polarization-resolved magneto-PL and polarization-resolved PL decay technique.

energy transfer process, in colloidal nanostructures. Firstly, by measuring the PL decay the radiative decay time τ_r, that characterizes how fast exciton complexes recombine, can be evaluated. Furthermore, the bright-dark splitting energy of excitons can be extracted from the temperature dependence of τ_r (see Sec. 2.3). Secondly, the spin relaxation time which characterizes how long exciton complexes are able to keep their spin on one state can be extracted from measuring the polarization-resolved PL decay (see Sec. 2.5). Thirdly, in combination with the spectrally resolved technique, this method is also a powerful tool to investigate the Förster energy transfer process in closely packed colloidal nanostructures.

The experimental setup for the polarization-resolved PL decay technique is shown in Fig. 3-1. The sample located in the 15 T cryostat was excited by an unpolarized pulsed diode laser (photon energy 3.06 eV, pulse width 50 ps, repetition rate: 0.2 Hz to 5 MHz). The PL was either filtered out from scattered laser light by a band-pass filter (full width at half maximum (FWHM) of transmission was 50 nm, i.e. about 150 meV) with center wavelength at the PL maximum of colloidal nanostructures (see the area in the black dashed rectangular) or dispersed with a 0.55 m spectrometer (see the area in the green dashed rectangular). Finally the PL was detected by an avalanche photodiode connected to a conventional time-correlated single-photon counting setup (PicoHarp 300, highest time resolution: 4 ps). The time resolution of the setup was limited by modal dispersion in the fiber. The instrumental response function of the setup was 0.8 ns at FWHM.

The working principle of the time-correlated single-photon counting setup is as follows: The single-photon counting module has two channels. The first channel receives the trigger signal from the laser controller. The second channel receives the signal from the avalanche photodiode. The single-photon counting module counts the time interval between the trigger signal and the signal from the avalanche diode. Once the single-photon counting module received the signal from the avalanche diode, the counting stops until the arrival of the next trigger signal. This circle repeats many times depending on the total accumulation time and the time resolution of the setup. The graph of the sum of the total number of photons detected at specific time delay versus the time corresponds to the decay of the PL (see Fig. 3-2). The radiative decay time of the exciton complex can be extracted by fitting the PL decay with exponential functions.

3.4 Fluorescence-line-narrowing technique

Usually, PL spectra of an ensemble of colloidal nanocrystals measured with non-resonant excitation are rather broad (FWHM of $\sim$ tens of meV[25,60]) compared with that of a single NC (FWHM $<$ 1 meV[27]) due to the size dispersion. This size dispersion of NCs limits the possibility to accurately determine the Zeeman splitting . This problem can be overcome by exciting the sample resonantly. Under

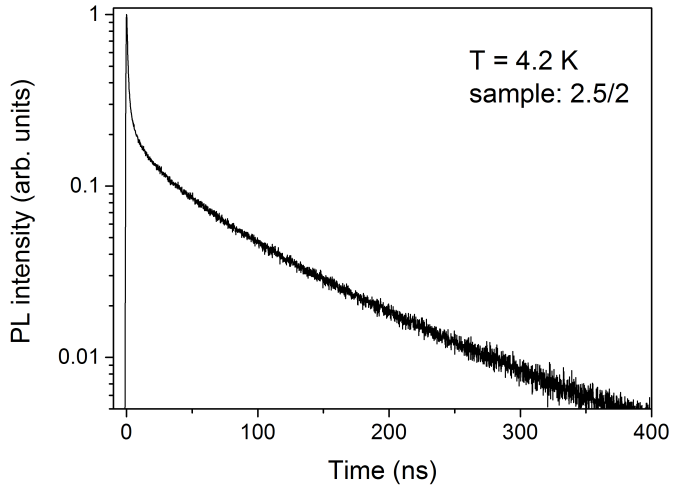

Figure 3-2: The PL decay of thin-shell CdSe/CdS NCs measured at $T = 4.2$ K. Core radius: 2.5 nm. Shell thickness: 2 nm.

resonant excitation, only a small portion of colloidal NCs with quite small size dispersion limited by the width of the excitation laser are excited. In comparison to the non-resonant excitation, the spectra obtained under resonant excitation are much narrower, therefore, this PL measurement with resonant excitation is also named as fluorescence-line-narrowing (FLN). The FLN technique is a powerful tool to study optical orientation, and with sufficiently high spectral resolution, even exciton fine structure can be directly observed from an ensemble of colloidal NCs.

Figure 3-3 shows the scheme of the experimental setup for the FLN technique. The sample was mounted in a 10 T cryostat in Faraday geometry with direct optical access through windows and excited resonantly with a circularly polarized laser beam generated by a dye laser. The PL was sent into a triple spectrometer (spectral resolution: ~ 30 μeV for for all three stages in the additive mode) through a cross slit and recorded by a CCD camera. Since the laser line was quite close to the zero-phonon line, a triple spectrometer was required to suppress the scattered laser light. The reliability of the optical orientation measurement strongly depended on to what extent the scattered laser light could be suppressed. The cross slit allowed us to spatially select specific sample areas and further filter out scattered laser light. σ^+ and σ^- polarized PL could be selected by the linear polarizer and $\lambda/4$ plate in the detection path.

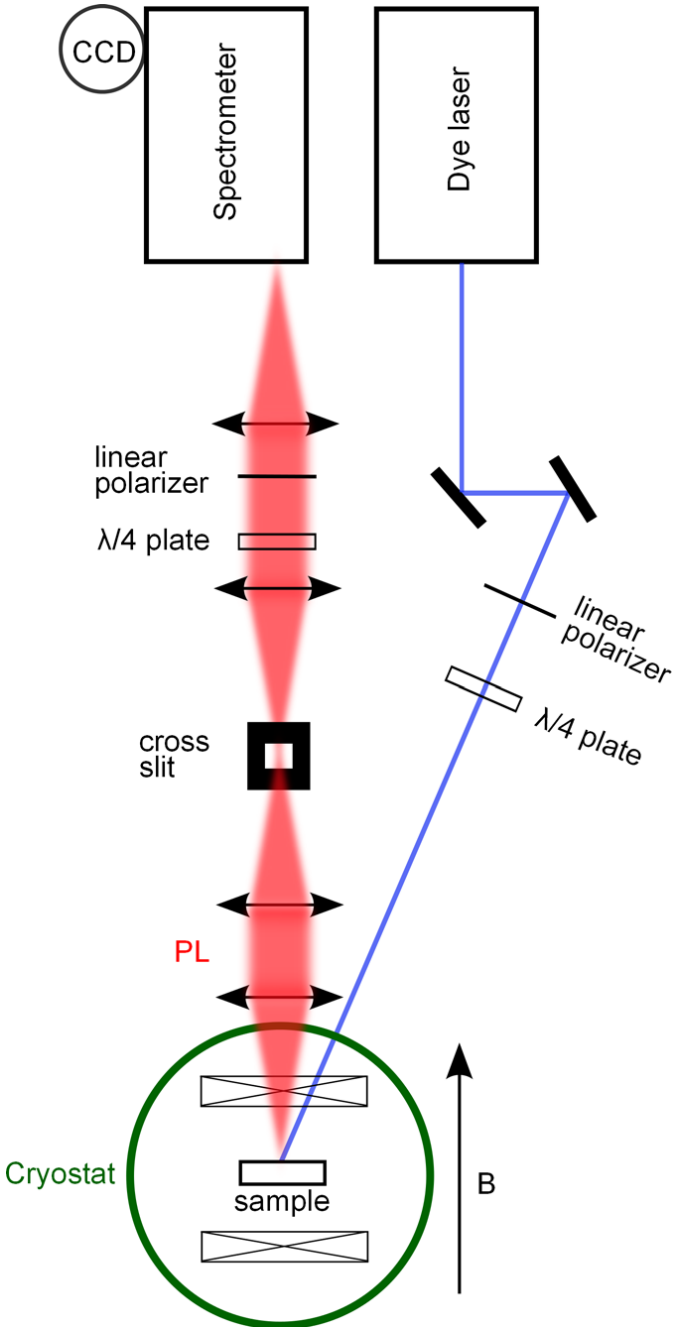

Figure 3-3: Experimental setup for fluorescence-line-narrowing technique.

Chapter 4

Spin dynamics of negative trions in CdSe/CdS colloidal nanocrystals

The study on colloidal nanostructures was started from a new type of thick-shell CdSe/CdS colloidal nanocrystals (NCs). Compared with conventional thin-shell colloidal NCs, whose practical applications are limited by the intermittency of the photoluminescence intensity (or blinking), the blinking in thick-shell CdSe/CdS NCs is almost completely suppressed[13,16] and the photoluminescence (PL) is never completely quenched[15].

There is consensus today that under illumination all NCs can become charged (or ionized), and subsequently neutralized. One of the photoexcited carriers (electron or hole) may be ejected from the NC. At some later time, the ejected carrier can return to the NC restoring charge neutrality. This process is seen in the blinking of single NCs, for which the non-radiative Auger recombination is faster than the radiative recombination of charged excitons (trions)[67]. In NCs with suppressed Auger processes the charging/neutralization processes do not result in blinking, but it causes intermittency of the PL decay times[68].

The NC neutralization, however, takes sometimes hours as measured in CdS NCs embedded in a glass matrix[69], so that for all practical reasons such ionized NCs can be considered as permanently charged. It was demonstrated that optical excitation creates positive charge in (Cd,Zn)Se/ZnSe alloyed NCs[70] and negative charge in CdSe/CdS core/shell NCs in vacuum[18]. Permanent charge can be induced in NCs also by applying a bias voltage[71,72]. This electro-chemical method leads to negative charging of CdSe/CdS NCs[16,73]. The less controllable optical charging method developed for CdSe/ZnS NCs[74,75] leads mainly to positive charging[76].

Magneto-optical spectroscopy is a powerful tool for investigating the energy levels and selection rules of excitons, trions, and biexcitons responsible for the band-edge PL in semiconductors[77,78,79]. Such measurements have allowed one to

understand the basic optical properties of uncharged core/shell CdSe/ZnS colloidal NCs[20,24,25,26,27,28] and more generally the fine structure of excitons and their PL properties in quasi-spherical NCs composed of direct band semiconductors[20]. In quasi-spherical wurtzite CdSe NCs, the lowest eight-fold degenerated exciton states are split into five energy levels by the crystal field of the hexagonal lattice and the electron-hole exchange interaction[20]. The dependence of the band-edge exciton fine structure on the shape and size of the NC is well established theoretically[20,21,22,23]. Most importantly, the ground exciton state is an optically passive dark state with total angular momentum projection on the hexagonal axis of ± 2. The PL at low temperatures originates from phonon-assisted recombination of dark excitons or the mixing of bright- and dark-exciton states by magnetic impurities or by dangling bonds at the NC surface[24,25,80]. The dark exciton can be also activated by an external magnetic field, which mixes it with the bright-exciton states[24,25,80].

While trion lines are commonly seen in the PL of epitaxial quantum dots (QDs), fast non-radiative Auger recombination of trions does not allow measurement of PL from charged colloidal CdSe or CdSe/ZnS NCs. Only by pump-probe time-resolved Faraday rotation techniques, which do not require a finite time for signal formation as in case of the PL, two important characteristics of charged NCs could be measured, namely the size dependence of the electron g-factor and its spin dephasing time[62,81]. These measurements, however, do not provide information on the fine structure of the trion levels and the mechanisms of trion thermalization in NCs. The situation has changed with the growth of CdSe/CdS core/thick shell NCs in which the trion demonstrates strong PL efficiency. Indeed, it has been shown recently that the long-lived resident charge created optically in CdSe/CdS core/thick shell NCs is the electron and the PL of these NCs arises from negatively charged trions[18].

In this chapter we focus on the spin dynamics in thick-shell CdSe/CdS NCs. The structure of this chapter is as follows: firstly by analyzing the recombination dynamics and FLN spectra, we prove that the emission of thin-shell NCs is contributed by neutral excitons, while for thick-shell NCs it is dominated by charged excitons. Secondly, using the sign of the PL polarization, we unambiguously demonstrate that these trions are negatively charged. Thirdly, based on A. V. Rodina's model of the PL polarization in an ensemble of randomly oriented NCs (see Sec. 2.5), the hole g-factor in CdSe/CdS NCs is evaluated. Fourthly, from direct measurements of the spin relaxation rate dependences on magnetic field and temperature we identify the mechanism of the negative trion spin relaxation as two-phonon-assisted Raman scattering between the hole spin sublevels mixed by the applied magnetic field. Finally, we show that the rise time of the degree of PL circular polarization can be used as a criterion to distinguish neutral NCs and charged NCs.

4.1 Experimentals

The core/shell CdSe/CdS NCs were synthesized by a method similar to the one described in Refs. 13, 82. The initially fabricated zinc-blende CdSe cores with radius of 2.5 nm were overgrown by wurtzite CdS shells with thicknesses varying from 2 to 10 nm. As defined in the previous chapter, these samples are referred as "C/S", where C is the CdSe core radius and S the CdS shell thickness, both in nanometers.

Figure 4-1(a) shows a transmission electron microscopy (TEM) image of thick-shell CdSe/CdS colloidal NCs. The shape of NCs is rhombohedral rather than spherical. NC shape asymmetry are generally expected to reduce the symmetry of the electronic level structure of CdSe/CdS NCs, lifting, for examples, degeneracies.

The samples were prepared for ensemble measurements by drop casting the CdSe/CdS NC solution on a quartz plate. For magneto-optical experiments at low temperatures the sample was mounted in Faraday geometry (external magnetic field B perpendicular to the quartz plate and parallel to the light wave vector) in the core of a superconducting solenoid generating magnetic fields up to 15 T. The sample was in contact with helium gas so that the bath temperature could be varied from $T = 2.4$ up to 20 K.

For time-integrated measurements, the PL was excited through a multimode optical fiber, using a continuous wave (CW) diode laser (photon energy 3.33 eV), and collected through a detection fiber. A circular polarizer inserted between the sample and the detection fiber allowed us to detect the σ^+ and σ^- polarized PL by alternating the magnetic field direction. The collected signal was dispersed with a 0.55 m spectrometer and detected by a liquid-nitrogen-cooled charge-coupled device camera.

For time-resolved measurements the excitation laser was replaced by a pulsed diode laser (photon energy 3.06 eV, pulse width 50 ps, repetition rate 1 MHz). The PL was filtered from scattered excitation light by a band-pass filter (full width at half maximum (FWHM) 50 nm, i.e. about 150 meV) with center wavelength at the PL maximum of NCs, and detected by an avalanche photodiode connected to a conventional time-correlated single-photon counting setup. The time resolution was limited by modal dispersion in the fiber, the instrumental response function of the setup was 0.8 ns at FWHM. All measurements were performed at low excitation density of 0.1 mW/cm^2 to suppress any multiexcitonic contribution in the emission spectra.

Figure 4-1(b) shows normalized PL spectra of thin-shell (2.5/2) and thick-shell (2.5/10) CdSe/CdS NCs measured at $T = 4.2$ K. The FWHM of the PL spectra are $\sim$ 57 meV corresponding to 3% size dispersion of the NCs. The thin-shell NC spectrum is shifted to higher energy by 12 meV with respect to the PL of the thick-shell NCs. Inhomogeneously broadened structure-less PL spectra do not

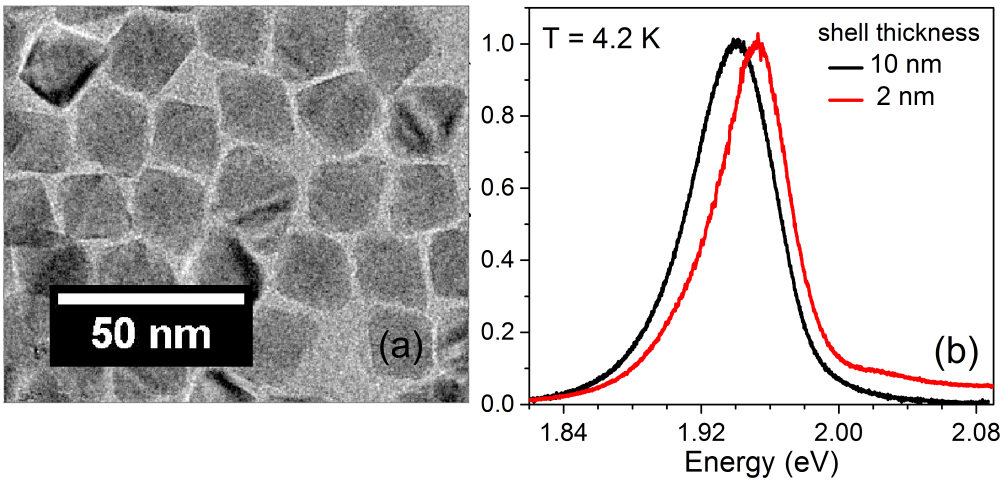

Figure 4-1: (a) Transmission electron microscopy image of 2.5/10 CdSe/CdS colloidal NCs. The image was taken on a JEOL 2010 field electron gun microscope operated at 200 keV. (b) PL spectra of thin-shell (2.5/2) and thick-shell (2.5/10) CdSe/CdS NCs under CW excitation.

allow identification what excitons are responsible for the PL, namely, whether neutral or charged excitons dominate the emission. There may be differences for NCs with varying shell thickness, as the photocharging mechanisms, based on e.g. the carrier capture at a surface state, can critically depend on this thickness. We address this problem by investigating the temporal dependence of the low temperature PL intensity and the polarization degree as functions of temperature and in external magnetic field. Here we focus on results for the NCs with the thinnest (2 nm) and the thickest (10 nm) fabricated shells, which demonstrate very different behaviors in recombination and spin dynamics.

4.2 Charged versus neutral NCs

The PL decays of the thin-shell and thick-shell CdSe/CdS NCs measured at different temperatures and magnetic fields are shown in Fig. 4-2. At $T = 4.2$ K, the PL decay of the thin-shell (2 nm) NCs shows a biexponential behavior with an initial fast decay occurring within our temporal resolution (<1 ns) and a subsequent slow decay with about 100 ns time constant. When rising the temperature to 20 K, the contribution of the fast decay vanishes and the slow decay shortens to about 20 ns. Additionally, when applying a magnetic field at $T = 4.2$ K, the slow component shortens to 30 ns at 15 T (see insert in Fig. 4-2(c)).

Such magnetic field and temperature behavior of the PL is well known for NCs. It has been observed in the PL of neutral excitons of the heavily studied wurtzite CdSe NCs, and was explained considering the spin and radiative properties of the exciton levels. In these NCs the crystal field and shape anisotropy split the four-fold degenerate hole ground state with total momentum $|\boldsymbol{K}| = 3/2$ into two states

with projections $M = \pm 3/2$ (heavy holes) and $\pm 1/2$ (light holes) onto the low-symmetry (quantization) axis[20]. The neutral exciton formed from the ground hole sublevels with $M = \pm 3/2$ is further split by electron-hole exchange interaction into optically forbidden (dark) states, $|\mathrm{F}\rangle$, with momentum projection ± 2 and optically allowed (bright) states, $|\mathrm{A}\rangle$, with momentum projection ± 1 (see Figure 4-2(a)).

We note, that despite the cubic crystal structure of the CdSe core, several factors can reduce the symmetry of the electronic level structure in our CdSe/CdS NCs and lead to a splitting Δ_{LH} between light- and heavy-hole states. Among these factors are (i) anisotropic strain induced by the CdS wurtzite shell, and (ii) NC shape asymmetry as suggested in Ref. 76 and as seen in Fig. 4-1(a). This allows us to assume that the exciton fine structure in our CdSe/CdS thin shell NCs is similar to the fine structure of wurtzite CdSe NCs. In this case we relate the fast component of the PL decay at 4.2 K seen in Fig. 4-2(c) to rapid thermalization of the excitons from the $|\mathrm{A}\rangle$ to the $|\mathrm{F}\rangle$ state at a rate γ_0, while the long component corresponds to the dark exciton recombination rate Γ_{F}. With increasing temperature the dark excitons are activated to the bright states and relax back via absorption or emission of phonons. In the case of one-phonon process, the rate is given by $\gamma_0 N_B$, where $N_{\mathrm{B}} = 1/[\exp(\Delta E/k_{\mathrm{B}}T) - 1]$ is the Bose-Einstein phonon number at temperature T. For $\gamma_0 N_B \gg \gamma_0$ both states contribute to the PL and the PL decay rate is determined by their thermally-equilibrium population tending to $(\Gamma_{\mathrm{A}} + \Gamma_{\mathrm{F}})/2$ at high temperatures[27,59,83,84,85]. The shortening of the slow PL component with magnetic field in this model is caused by the admixture of the bright to the dark-exciton state by a magnetic field perpendicular to the NC quantization axis[25,28,60,80,84]. Therefore, we conclude that for our experimental conditions the PL in the thin-shell NCs is dominated by recombination of neutral excitons.

Considerably different recombination dynamics are observed for the 10 nm thick-shell NCs shown in Fig. 4-2(d). The initial decay with 8 ns time constant at $T = 4.2$ K is much longer than the one in the thin-shell NCs. This short-termed decay contributes to approximately 90% to the PL intensity in the studied temperature range. The decay time only slightly increases with temperature and is independent of the magnetic field, see insert of Fig. 4-2(d). This behavior is typical for trion emission[86] and cannot be explained within the framework of the bright-dark exciton model just discussed. The slow PL component in the thick-shell NCs, which behaves very similar to the slow decay in the thin-shell NCs, i.e. shortens with increasing temperature and magnetic field, we assign to the exciton recombination in a small portion of neutral NCs. The lowest trion states consist of singlet configurations of either two electrons and a hole (negative trion) or of two holes and an electron (positive trion). These states are always optically allowed and have short radiative lifetime, which are almost independent of temperature and magnetic field[75,86]. Worthwhile to note that the thermal or magnetic-field-induced mixing of the trion states with $|M| = 3/2$ and $1/2$ would not result in

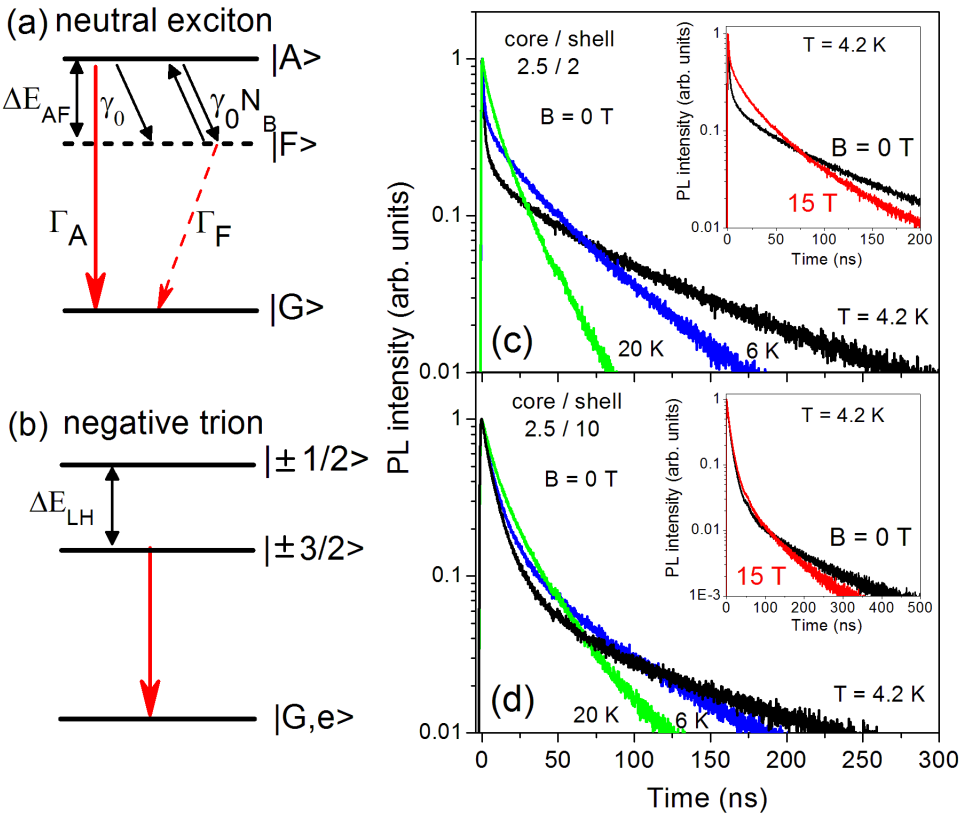

Figure 4-2: Energy level schemes of (a) neutral excitons and (b) negative trions. $|\mathrm{A}\rangle$, $|\mathrm{F}\rangle$ and $|\mathrm{G}\rangle$ denote bright exciton, dark exciton and ground states, respectively. ΔE_{AF} is the bright-dark splitting. γ_0 is the spin-relaxation rate from the bright to the dark-exciton state. $\gamma_0 N_B$ is the spin-relaxation rate between bright- and dark-exciton states induced by thermal mixing. Γ_{A} and Γ_{F} are recombination rates of bright and dark excitons. $|\pm 1/2\rangle$ and $|\pm 3/2\rangle$ are negative trion states with $M = \pm 1/2, \pm 3/2$. $|\mathrm{G,e}\rangle$ is the ground state of the negative trion, which is a resident electron in the CdSe core. ΔE_{LH} is the splitting between heavy-hole and light-hole. (c), (d) Temperature dependences of normalized PL decay of CdSe/CdS NCs with shell thicknesses of 2 and 10 nm at $B = 0$ T. Insets: normalized PL decay at $B = 0$ and 15 T for $T = 4.2$ K.

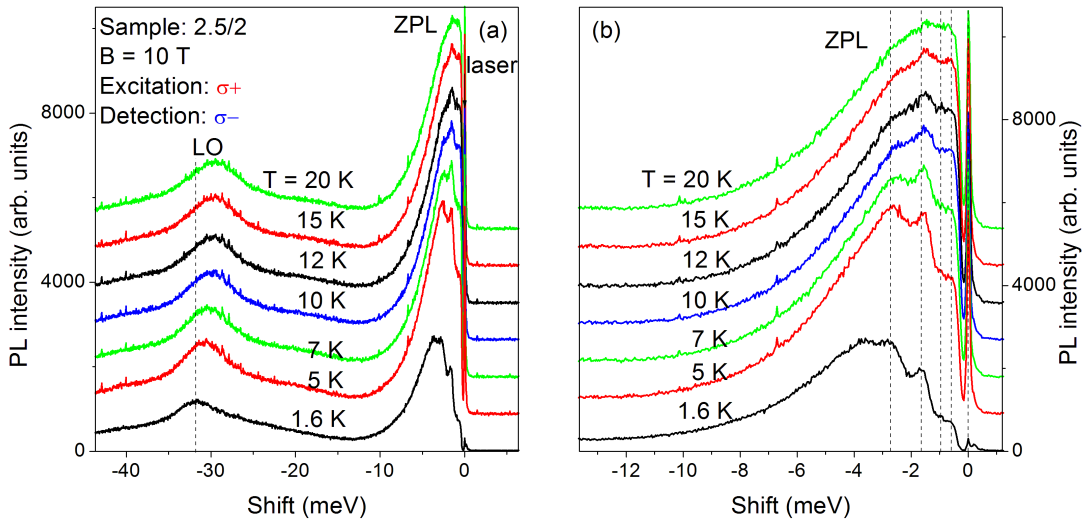

Figure 4-3: (a) Temperature dependence of FLN spectra of thin-shell (2 nm) CdSe/CdS NCs measured at $B = 10$ T from 1.6 to 20 K. (b) Enlarged zero-phonon lines shown in (a). The x-axis is the energy shift with respect to the laser line. The sample was excited with $\sigma+$ polarized laser light, and $\sigma-$ polarized PL was detected.

changing trion recombination time, as these states have the same radiative rate[86]. Fig. 4-2(b) shows schematically the level structure of a negative trion with lowest state $|\pm 3/2\rangle$ determined by the heavy hole. From the recombination dynmics, one can conclue that the PL emission of thick-shell CdSe/CdS NCs is dominated by the recombination of trions. This assumption is further justified by the fluorescence-line-narrowing (FLN) measurement.

Figure 4-3(a) shows FLN spectra of thin-shell (2 nm) CdSe/CdS NCs measured at $B = 10$ T from T =1.6 to 20 K. At 1.6 K, the zero-phonon line shows rich features which are shown more clearly in Fig. 4-3(b). These rich features originate from different bright- and dark-exciton states (see Fig. 2-2). With the increase of temperature, these features merges with each other due to the thermal mixing of bright- and dark-exciton states. It can be seen in Fig. 4-3(a) that the first optical phonon line consisted of optical phonon lines originating from various bright- and dark-exciton states shows a blue shift at higher temperature. This is not because the band structure changes with temperature, at least not in such small temperature range, but due to the thermal mixing between the lowest dark-exciton states and higher states.

Different behaviors of thin- and thick-shell CdSe/CdS NCs are seen in the magnetic field dependence of FLN spectra. As shown in Fig. 4-4(a), by applying magnetic field, zero-phonon line of thin-shell CdSe/CdS NCs shifts to lower energy and more features appears due to the mixing between the lowest dark-exciton states and higher states. By contrast, the zero-phonon line of thick-shell CdSe/CdS NCs keeps as a single peak at all magnetic field (see Fig. 4-4(b)). This behavior

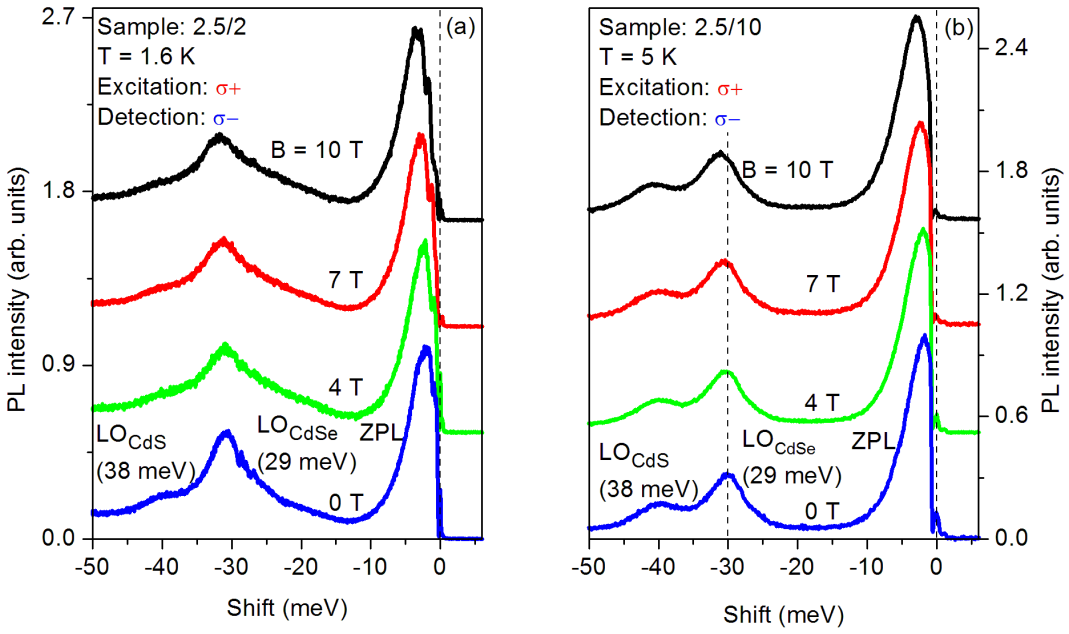

Figure 4-4: Magnetic field dependence of FLN spectra of (a) thin-shell (2 nm) and (b) thick-shell (10 nm) CdSe/CdS NCs. The x-axis is the energy shift with respect to the laser line. The sample was excited with $\sigma+$ polarized laser light, and $\sigma-$ polarized PL was detected.

evidences that the PL of thick-shell CdSe/CdS NCs is dominated by trions which have only one bright state. Additionally, optical phonon lines originating from the recombination of trions with the assistant of phonons from both CdSe core and CdS shell are observed (see the blue line). The optical phonon energy of CdSe and CdS is 29 meV and 38 meV, respectively. It is worth mentioning that the ratio between the intensity of LO_{CdS} phonon line and that of the LO_{CdSe} phonon line can be used as a tool to evaluate the shell thickness. It can be seen that compared with thin-shell NCs, the intensity of LO_{CdS} phonon line relative to that of LO_{CdSe} phonon line in thick-shell NCs is stronger, which indicates a larger shell thickness.

Based on the magnetic field and temperature dependence of the PL dynamics and FLN spectra, we conclude that the PL in the thick-shell NCs is dominated by recombination of trions. The recombination dynamics and FLN spectra however are not sufficient to identify the type of trion. This information can be obtained uniquely from measurements of the degree of circular polarization (DCP) in an external magnetic field, as demonstrated in Ref. 18. We will discuss the connection between the charge of the trion and the sign of PL polarization in detail below and will show that the PL in our thick shell CdSe/CdS NCs is dominated by the emission of negative trions.

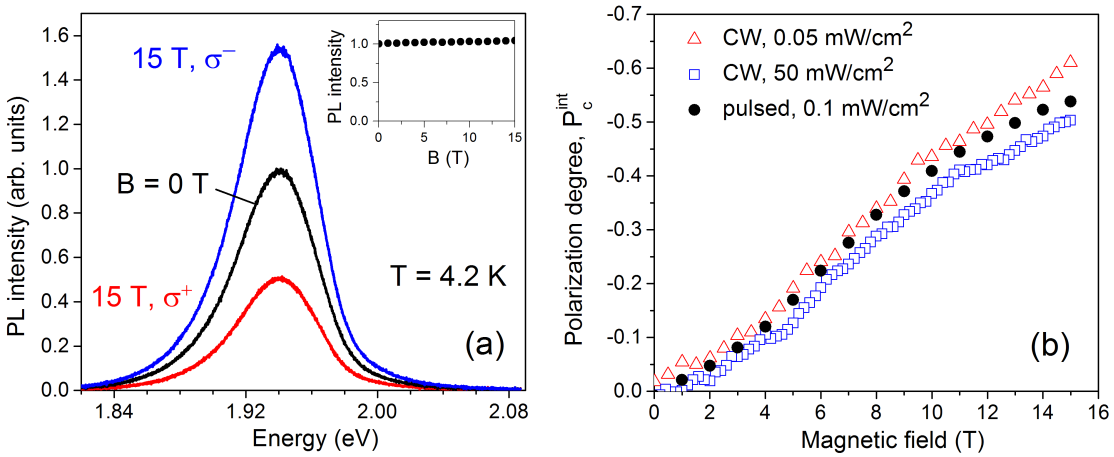

Figure 4-5: (a) Polarized PL spectra of thick-shell 2.5/10 CdSe/CdS NCs at $B = 0$ and 15 T measured under CW excitation with 50 mW/cm^2 power. Insert: Magnetic field dependences of the integral PL intensity summed over both polarizations ($I^+ + I^-$). (b) Magnetic field dependence of the time-integrated DCP measured for CW (triangles and squares) and pulsed (circles) excitation on thick-shell 2.5/10 NCs. $T = 4.2$ K.

4.3 Determination of the resident carrier sign

Figure 4-5(a) shows polarization-resolved PL spectra of thick-shell CdSe/CdS NCs at $B = 0$ and 15 T. The external magnetic field polarizes the PL enhancing its σ^- component. The same sign of circular polarization was reported for CdSe/ZnS NCs[25]. The integral PL intensity summed over both polarizations does not change with the magnetic field, see insert, which substantiates the conclusion of Ref. 18, that non-radiative recombination plays a minor role for the CdSe/CdS NCs we study.

There is no spectral dependence of the PL polarization degree, P_c, for the studied NCs which allows us to present in the following the PL intensity spectrally integrated over the whole PL line or spectral range of the band-pass filter without any loss of information. Figure 4-5(b) shows the spectrally integrated DCP measured under various excitation conditions and evaluated according to Eq. (2.25). One sees that the DCP measured under CW excitation (red triangles) and pulsed excitation (black circles) using similar low excitation powers almost coincide. The DCP shows a slightly nonlinear dependence on magnetic field for $B < 10$ T, and for higher fields it has the tendency to saturate. A high polarization degree of -0.60 is achieved at $B = 15$ T.

The DCP only slightly decreases with increasing the CW excitation density by three orders of magnitude up to 50 mW/cm^2 (blue squares). This implies that the lattice and spin temperatures do not change notably and the trion emission remains dominant for the excitation densities we use. Besides, already a very low excitation density is sufficient to provide photocharging of the CdSe core for the majority of thick-shell CdSe/CdS NCs[18]. The sign of the resident charge responsible for the

trion PL in CdSe/CdS NCs can be unambiguously determined from the sign of PL polarization. This identification tool was first reported in semiconductor quantum wells, considering different combinations of electron and hole g-factor values[65,66].

The spin structure of negative and position trions in CdSe/CdS NCs subject to a magnetic field is determined by the g-factor of hole and electron respectively. In CdSe/CdS NCs, the g-factor of electron is positive. In bulk CdSe $g_e = +0.68$[87] and g_e increases with the quantum confinement in NCs reaching $g_e = +1.2$ for wurtzite CdSe NCs with core radius 2.5 nm[62]. A slightly smaller g_e value can be expected for our cubic core NCs, which have smaller confinement energy (optical transition at 1.95 eV instead of 2.05 eV for wurtzite NCs)[88,89]. The hole g factor was found to be negative both theoretically, $g_h = -1.09$, as a result of calculations using the effective mass parameters of bulk CdSe[20], and experimentally -0.73 as a result of fitting of the exciton effective g-factor in CdSe NCs[62]. The spin level structures in CdSe/CdS NCs is shown in Fig. 2-7. It is clear from the scheme of Fig. 2-7 that the negative DCP measured in our experiments directly identifies the trion in CdSe/CdS NCs as negatively charged. This allows us to conclude that the electron is the resident carrier in the CdSe core as a result of the NC photocharging.

4.4 Spin dynamics of negative trions in thick-shell NCs

4.4.1 Time-resolved DCP

It is generally known that the degree of PL polarization can significantly deviate from the thermal equilibrium value which is determined solely by the thermal populations of the two emitting spin sublevels[78]. The equilibrium population in many cases cannot be reached due to the competition between spin relaxation time and radiative decay time. A convenient way to study that is to measure the temporal dependence of the degree of PL polarization. The idea of this experiment is illustrated in Fig. 4-6 and shows the decay of the σ^+ and σ^- polarized PL intensities measured for thick-shell NCs at $B = 5$ T as well as the DCP time evolution calculated based on Eq. (2.24).

The DCP increases rapidly after pulsed excitation at zero time delay and then saturates at a level of -0.32, which corresponds to the equilibrium polarization of negatively charged trions in the randomly oriented NC ensemble (see Fig. 4-6). On the 100 ns time scale the populations $N_{3/2}$ and $N_{-3/2}$ of the trion spin sub-levels $|+3/2\rangle$ and $|-3/2\rangle$ should reach thermal equilibrium.

The temporal dependence of the experimentally recorded ensemble PL polar-

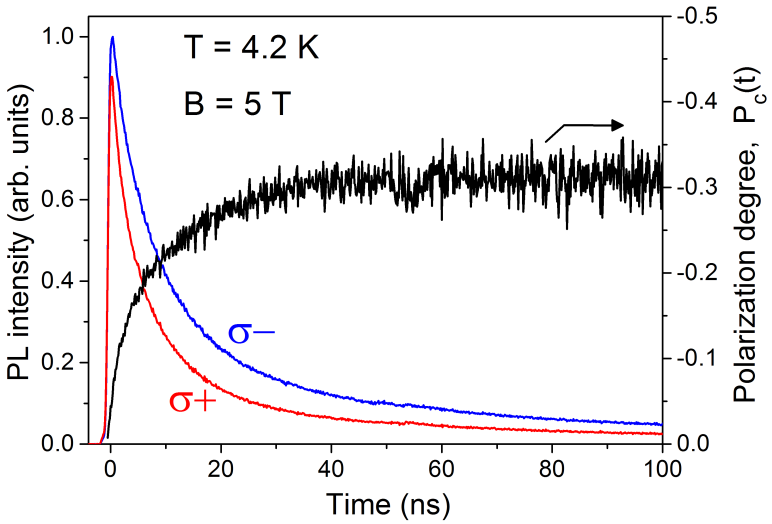

Figure 4-6: Polarization-resolved PL decay and time-resolved DCP for thick-shell 2.5/10 CdSe/CdS NCs measured under pulsed excitation with density 0.1 mW/cm^2.

ization can be described using the following empirical expression :

$$P_{\mathrm{c}}(B,t) = \{1 - \exp[-t/\tau_{\mathrm{s}}^{\mathrm{exp}}(B)]\} P_{\mathrm{c}}^{\mathrm{eq}}(B) \tag{4.1}$$

where $\tau_{\mathrm{s}}^{\mathrm{exp}}$ is the experimentally measured spin relaxation time in the NC ensemble. Note, that this is an averaged characteristic quantity, as the spin relaxation time in individual NCs depends on θ. Fitting of the experimental data in Fig. 4-6 with Eq. (4.1) gives $\tau_{\mathrm{s}}^{\mathrm{exp}} \approx 12\,\mathrm{ns}$ at $B = 5\,\mathrm{T}$.

Figure 4-7(a) shows the magnetic field dependences of the time-resolved DCP of thick-shell CdSe/CdS NCs. With increasing magnetic field the DCP saturation level increases up to -0.60 at $B = 15$ T, and also the rise time of the DCP shortens considerably. It should be noted, that the DCP rise time in thick-shell NCs is much longer than the one of conventional thin-shell NCs (< 1 ns)[60]. Figure 4-7(b) shows the temperature dependences of time-resolved DCP at $B = 5$ T. The spin relaxation time $\tau_{\mathrm{s}}^{\mathrm{exp}}$ becomes shorter for elevated temperatures. Additionally, the temperature increase reduces the DCP saturation level, as expected from the reduction of the equilibrium spin polarization $M^{\mathrm{eq}} \propto \rho_0(B,x,T)$, see Eq. (2.45).

The magnetic field dependences of the spin relaxation and radiative recombination times extracted from the time-resolved data of Fig. 4-7(a) are collected in Fig. 4-8(a). Here the DCP rise time $\tau_{\mathrm{s}}^{\mathrm{exp}}$ is compared with the trion lifetime τ_{r} evaluated by fitting the PL decay during the initial 50 ns by a single exponential decay function. The trion lifetime is almost independent of the magnetic field at a value of $\tau_{\mathrm{r}} = 8$ ns. On the other hand, $\tau_{\mathrm{s}}^{\mathrm{exp}}$ decreases strongly from 58 ns at $B = 1$ T down to 1 ns at 15 T. It is important, that with increasing magnetic field the system turns over from a regime where $\tau_{\mathrm{s}}^{\mathrm{exp}} >> \tau_{\mathrm{r}}$ to a regime with $\tau_{\mathrm{s}}^{\mathrm{exp}} << \tau_{\mathrm{r}}$. As a result, in weak magnetic fields equilibrium spin polarization is not reached

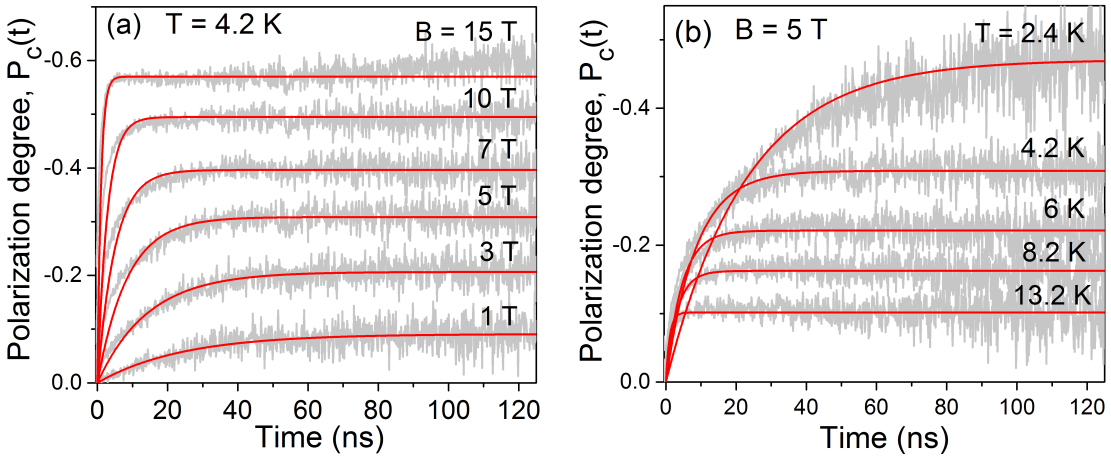

Figure 4-7: Time-resolved DCP of thick-shell 2.5/10 CdSe/CdS NCs: (a) at different magnetic fields and $T = 4.2$ K, and (b) at different temperatures and $B = 5$ T. Red lines are fits according to Eq. (4.1).

during trion lifetime, but it is reached in high fields.

The magnetic field dependences of $1/\tau_s^{exp}$ at different temperatures and its temperature dependences at different magnetic fields are shown in Fig. 4-9. Remarkably, the rise of $1/\tau_s^{exp}$ with increasing magnetic field for each temperature is proportional to B^2. Further, at each magnetic field the temperature dependence of the spin relaxation rate is proportional to T^2.

The strong deviation of the trion spin system from equilibrium is seen directly in Fig. 4-10, where the $P_c^{eq}(B)$ values (open circles) evaluated from the saturation level of $P_c(B,t)$ are compared with the time-integrated DCP, $P_c^{int}(B)$, determined for ensemble according to the definition Eq. (2.25) (closed circles). The finite spin relaxation time causes the reduction of $P_c^{int}(B)$ from the maximum value equal to $P_c^{eq}(B)$. The relative difference between these values is large in weak magnetic fields and decreases with growing field.

The experimental results presented in this section allow us to evaluate the hole g-factor g_h, which determines the Zeeman splitting of spin sublevels and the polarization of the negative trion, as well as the magnetic field dependence of the spin relaxation times in individual NCs. This requires, however, a model, which takes into account the distribution of the NC axes relative to the magnetic field direction which is presented in Sec. 2.5. Based on this model, the hole g-factor g_h can be extract by fitting the magnetic field dependence of DCP shown in Fig. 4-10. The red line in Fig. 4-10(a) shows the theoretical fit of experimental data for the thermal equilibrium DCP measured at $T = 4.2$ K using Eq. (2.47). The hole g-factor $g_h = -0.54$ is obtained as only fit parameter. To further justify the model, DCPs measured at various temperature are fitted using Eq. (2.47) with the same g-factor (-0.54) (see Fig. 4-11). It can be seen that the calculated DCP (red lines) fit the experimental data quite well. Note, that this is the direct measurement of

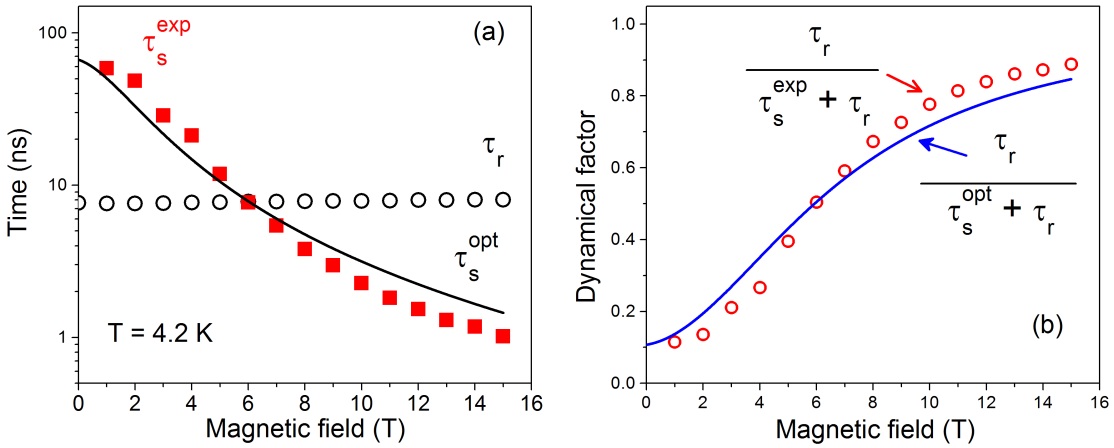

Figure 4-8: (a) Magnetic field dependences of the DCP rise time τ_s^{exp} (red squares) and PL decay time τ_r (black circles) for the thick-shell 2.5/10 CdSe/CdS NCs. Black line shows the evaluated optimal spin relaxation time τ_s^{opt} in NCs, which give the maximum contribution to the dynamical spin polarization. (b) Magnetic field dependence of the dynamical factors: $\tau_r/(\tau_s^{exp}+\tau_r)$ and $\tau_r/(\tau_s^{opt}+\tau_r)$ at $T = 4.2$ K.

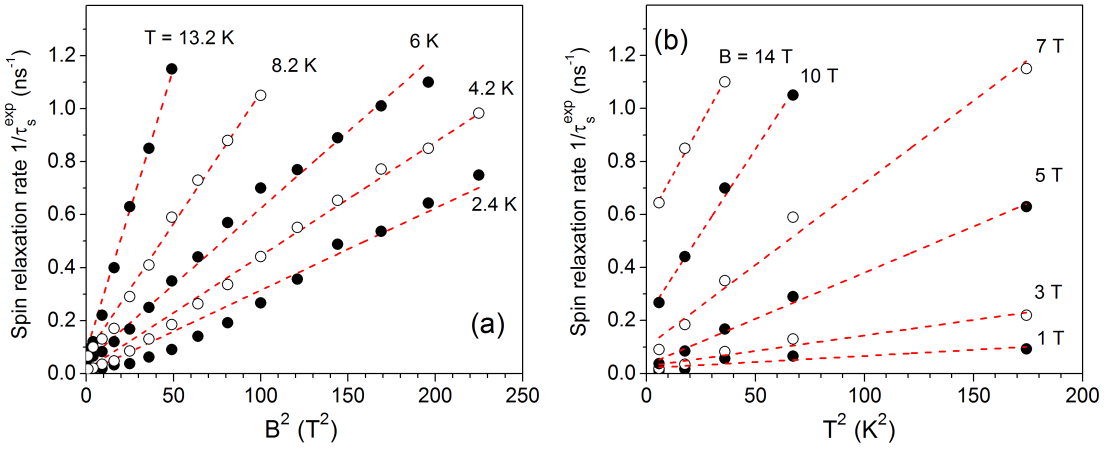

Figure 4-9: (a) Magnetic field and (b) temperature dependences of the ensemble spin relaxation time of trions, τ_s^{exp} (circles). Red lines are guides for the eye.

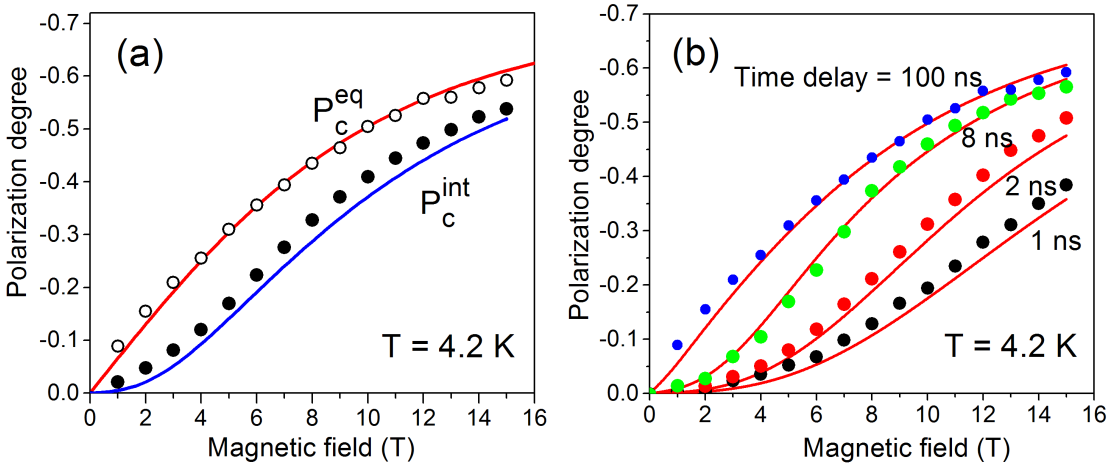

Figure 4-10: (a) Magnetic field dependences of the equilibrium DCP, P_c^{eq} (open circles), and time-integrated DCP, P_c^{int} (closed circles), measured for thick-shell 2.5/10 CdSe/CdS NCs at $T = 4.2\,\mathrm{K}$. The red and blue lines show the results of calculations based on Eqs. (2.47) and (2.49), respectively, with $g_h = -0.54$. (b) Magnetic field dependences of the time dependent DCP, $P_c(t)$ measured for 2.5/10 CdSe/CdS NCs at time delays of $t = 1, 2, 8$ and 100 ns. Solid lines show the results of calculations after Eq. (2.48) with $\tau_s(B, x, T)$ from Eq. (2.51).

the hole g-factor in CdSe NCs. The value is in reasonable agreement with previous experimental and theoretical estimates of g_h [20,62].

4.4.2 Spin relaxation mechanism

Let us consider now the mechanism responsible for the spin relaxation of the negative trion in the thick shell CdSe/CdS NCs. The observed slow spin relaxation is connected with the absence of spin-orbit perturbations, which directly mix the $+3/2$ and $-3/2$ hole states. In addition, phonons with angular momentum, $l = 3$, which are required for direct transitions between these spin sublevels, do not couple with them[64]. The important clue comes from the square dependence of the spin relaxation rate $1/\tau_s^{exp}$ on magnetic field and temperature shown in Fig. 4-9.

Angular and magnetic field dependence

The square dependence of the spin relaxation rate on magnetic field suggests that the relaxation mechanism is controlled by the mixing of the heavy-hole states $M = \pm 3/2$ with light-hole states $M = \pm 1/2$, induced by the component of the magnetic field perpendicular to the NC quantization axis. According to this suggestion, the spin relaxation rate can be written as Eq. (2.51) according to A. V. Rodina's model (see Sec. 2.6). To determine $\alpha(T)$, the coefficient that describes the phonon-assisted spin relaxation of hole from $M = \pm 1/2$ states to $\mp 2/3$ states, we fit the DCP rise dynamics at different magnetic fields using Eqs. (2.48, 2.51) at each

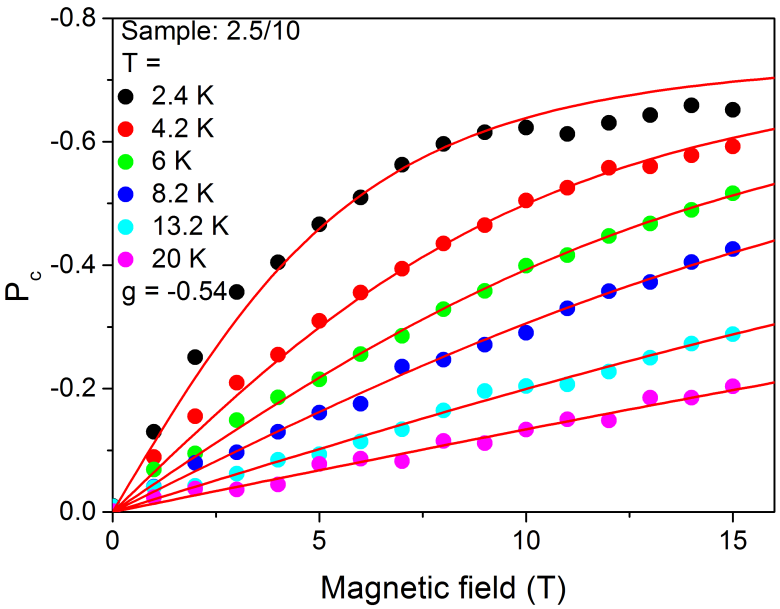

Figure 4-11: Magnetic field dependences of the equilibrium DCP, P_c^{eq} measured for thick-shell 2.5/10 CdSe/CdS NCs measured from $T = 4.2$ to 20 K. Red lines show the results of calculations based on Eq. (2.47) with $g_h = -0.54$.

temperature. At $T = 4.2$ K these time dependences are shown in Fig. 4-7(a). The magnetic field dependence of the spin relaxation rate $1/\tau_s(x, B, T)$ estimated at various temperatures for $x = 0$ is shown in Fig. 4-12.

Similarly to the spin relaxation rate $1/\tau_s^{exp}$ extracted according to the empirical model (see Fig. 4-9), $1/\tau_s$ also shows square magnetic field dependence at all measured temperatures but with larger value. The difference of the value between $1/\tau_s^{exp}$ and $1/\tau_s$ results from the random orientation of quantization axis in an ensemble of NCs. The empirical model assumes that all NCs have the same spin relaxation rate. Since the spin relaxation rate is actually dependent on the angle between the quantization axis and magnetic field, $1/\tau_s^{exp}$ can be considered as a sort of averaged spin relaxation rate. This "averaged" spin relaxation rate must be smaller than the fastest possible spin relaxation rate in NCs with quantization axis perpendicular to magnetic field ($x = 0$). Being extracted at different magnetic fields the parameter $1/\tau_{s0}$ and $\alpha(T)$ have some dispersion and we take its average value. At $T = 4.2$ K this procedure gives $1/\tau_{s0} = 0.015 \pm 0.007$ ns^{-1} and $\alpha = 0.014 \pm 0.001$ ns^{-1}T^{-2}.

The fastest spin relaxation occurs in NCs oriented perpendicular to the magnetic field direction ($x = 0$). Figure 4-14 shows the magnetic field dependence of $\tau_s(\theta = 90°)$ calculated according to Eq. (2.51) with α obtained by fitting for each magnetic field (red squares). The red curve shows the $\tau_s(\theta = 90°)$ magnetic field dependence calculated with the averages $\alpha = 0.014$ ns^{-1}T^{-2} using Eq. (2.51). One sees, that $\tau_s(\theta = 90°)$ decreases from 44 ns at $B = 1$ T down to 0.3 ns at 15 T. Note that here 0.3 ns is evaluated time, therefore it is not limited by the time

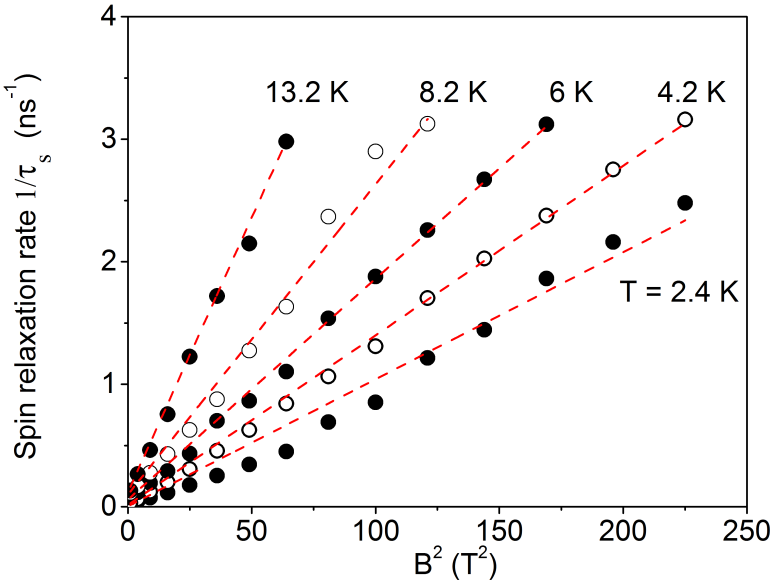

Figure 4-12: The magnetic field dependence of the calculated spin relaxation rate $1/\tau_s(x,B,T)$ in thick-shell (2.5/10) CdSe/CdS NCs estimated at various temperatures for $x = 0$. Symbols are calculated spin relaxation rate according to Eq. (2.51) with $x = 0$. $1/\tau_{s0}$ and α were obtained by fitting the time-resolved DCP (e.g. see Fig. 4-7) with Eqs. (2.48, 2.51). Being extracted at different magnetic fields, $1/\tau_{s0}$ and $\alpha(T)$ have some dispersion. Dashed lines show fitting of the magnetic field dependence of τ_s according to Eq. (2.51) with a constant $1/\tau_{s0}$ and α.

resolution of experimental setup (0.8 ns), as in fact longer times are measured.

The maximum trion polarization can be reached in NCs, which are oriented along the magnetic field. In these NCs, however, the magnetic field does not shorten the spin relaxation time, which stays equal to τ_{s0}. As a result, in the studied thick shell CdSe/CdS NCs with $\tau_{s0} \gg \tau_r$ the equilibrium trion polarization is never reached. On the other hand, in NCs oriented perpendicular to the magnetic field, which have the shortest spin relaxation time, there is no Zeeman splitting of the trion spin sublevels and the trions do not become polarized in these NCs.

Figure 4-13 shows the dependences of $\tau_r/[\tau_s(B,x,T)+\tau_r]$, $\rho_0(B,x,T)$ and of their product $\rho_s(B,x,T)$ as function of θ for $T = 4.2$ K and $B = 15$ T. One can see that the maximum contribution to dynamical spin polarization $-(3/2)\rho_s(B,x,T)$ (see Eq. (2.50)) comes from NCs oriented at the angle $\theta^{opt} \approx 39°$ ($x^{opt} \approx 0.78$). In Fig. 4-14 we show also the magnetic field dependence of τ_s^{opt} calculated according to Eq. (2.51) with $x = x^{opt}(B)$ determining the orientation of the NCs that give the largest contribution to the DCP at each magnetic field. The black line gives an accurate approximation of this dependence and is also shown for comparison in Fig. 4-8. The magnetic field dependence of τ_s^{opt} reproduces the empirically obtained magnetic field dependence of τ_s^{exp} with very high accuracy.

We note, that the admixture of the hole states with $M = \pm 1/2$ to the states with $M = \pm 3/2$ may lead also to a small nonzero splitting of the trion sublevels

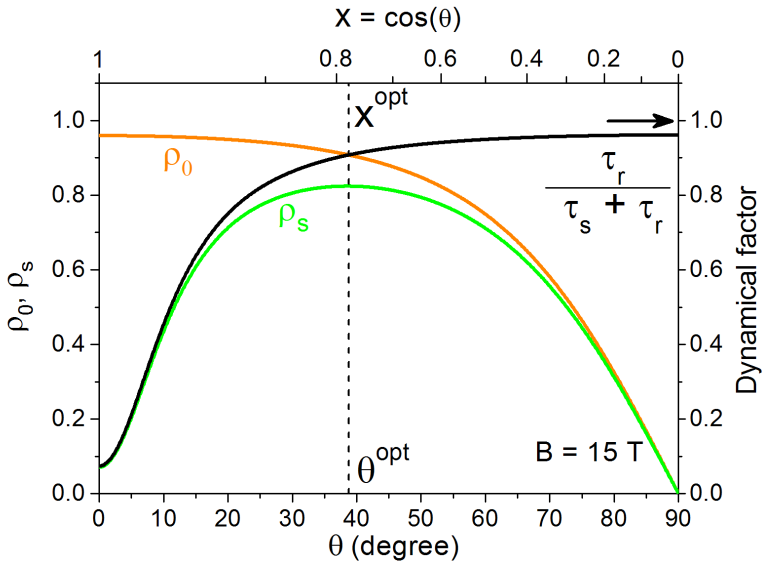

Figure 4-13: Dependences of $\tau_r/[\tau_s(B,x,T)+\tau_r]$, $\rho_0(B,x,T)$ and their product $\rho_s(B,x,T)$ on the angle θ (lower axes) and $x=\cos\theta$ (upper axes) calculated for $T=4.2$ K and $B=15$ T.

in the NCs oriented perpendicular to the magnetic field which is not taken into account in $\rho_0(B,x,T)$. We assume however, that the admixture is weak and the respective corrections to the Zeeman splitting are small, given by the parameter $|V_{\pm 3/2,\pm 1/2}|^2/\Delta_{\rm LH}^2 \ll x/(1-x)$ already for very small x. Accounting for these corrections would modify the dependence of the product $\rho_s(B,x,T)$ shown in Fig. 4-13 only in a narrow region near $x=0$ and is not important for the presented analysis. Our assumption is supported by the fact that the magnetic field dependencies of the saturation value of $P_c^{\rm eq}(B,T)$ are well fitted with the same value of g_h, that is independent of B and T.

Using Eq. (2.49) with α and τ_{s0} determined at $T=4.2$ K, we are able to reproduce the time-integrated DCP, $P_c^{\rm int}(B)$, shown in Fig. 4-10(a). The theoretical curve in Fig. 4-10(a) shown by the blue line is in good agreement with the experimental data. We emphasize, that this agreement is achieved without any fit parameters. The decay and spin relaxation times, τ_r and $\tau_s(B,x,T)$, used in the calculations, were measured experimentally in the polarization-resolved PL decay experiments and the g-factor ($g_h=-0.54$) was obtained by fitting the saturation value of the time-resolved DCP (see red line in Fig. 4-10(a)).

One can see in Fig. 4-10(a), that $P_c^{\rm int}(B)$ is always smaller than $P_c^{\rm eq}(B)$. Comparison of Eqs. (2.47) and (2.49), which define these two DCPs, shows that this difference is controlled by the dynamical factor $\tau_r/[\tau_s(B,x,T)+\tau_r]$. At low magnetic fields, the ensemble average $\tau_s^{\rm exp}$ is longer then τ_r, as shown in Fig. 4-8(a). In this case, trions will be in nonequilibrium state for a long time during the trion lifetime, which significantly reduces $P_c^{\rm int}$, e.g., at $B=4$ T to -0.12 compared to $P_c^{\rm eq}=-0.26$. By contrast, at high magnetic fields $\tau_s^{\rm exp} \ll \tau_r$. In this case, the

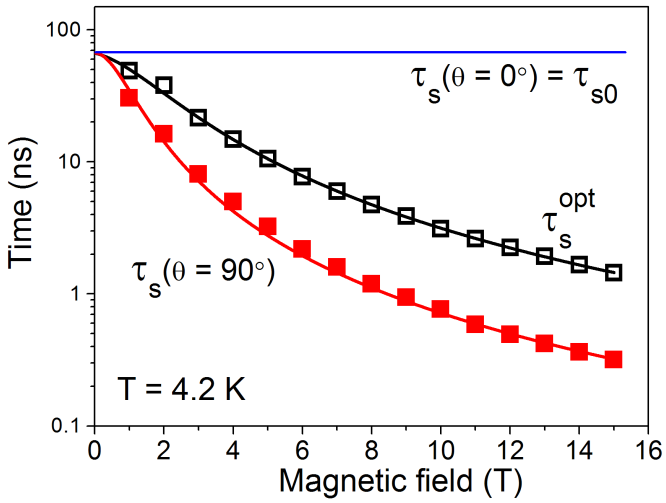

Figure 4-14: Calculated magnetic field dependence of spin relaxation times: red squares for NCs with fastest spin relaxation rate, $\tau_s(\theta = 90°)$; and black squares for NCs, which give the maximum contribution to the dynamical spin polarization, τ_s^{opt}. Blue line shows the magnetic field independent spin relaxation time in NCs oriented along magnetic field $\tau_s(\theta = 0°)$). Red line shows the magnetic field dependence of $\tau_s(\theta = 90°)$ calculated using Eq. (2.51) using fit parameters described in the text. Black line shows the polynomial approximation of the τ_s^{opt} dependence on magnetic field.

majority of the trions is in thermal equilibrium at the beginning of the PL decay. As a result, P_c^{int} at high magnetic fields is very close to P_c^{eq}, see Fig. 4-10(a).

In addition, in Fig. 4-10(b) we show the magnetic field dependences of the time-resolved DCP measured at delays of $t = 1, 2, 8$ and 100 ns. At 100 ns (blue circles) the DCP is well reproduced by the equilibrium model because $t \gg \tau_s$. At smaller delays the magnetic field dependence of the DCP is a complex function of the magnetic-field-dependent spin relaxation time and the radiative decay time. These complicated dependences, however, are well reproduced by Eq. (2.48) with $\tau_s(B, x, T)$ from Eq. (2.51) and the previously determined parameters τ_{s0} and α. This agreement is a strong confirmation of the correctness of the suggested spin relaxation model.

Temperature dependence

We turn now to the discussion of the strong temperature dependence of the experimental spin relaxation time, $\tau_s^{exp}(B, T)$, shown in Fig. 4-9(b). In A. V. Rodina's model (see Sec. 2.6) the temperature dependence is determined by the $\alpha(T)$ and $1/\tau_{s0}(T)$ parameters of the spin relaxation time $\tau_s(B, x, T)$ defined in Eq. (2.51). We extracted $\alpha(T)$ and $1/\tau_{s0}(T)$ from the temperature-dependent time-resolved DCP shown in Fig. 4-7 using Eq. (2.48) and plot the obtained values in Fig. 4-15.

$\alpha(T)$ and $1/\tau_{s0}(T)$ and, consequently, the spin relaxation rate, which is proportional to them, increase rapidly with temperature as T^2. This temperature

behavior indicates that the spin relaxation process of the hole in the negative trion is assisted by two-phonon scattering[90,91]. In a Raman two-phonon scattering process, the initial hole spin state is promoted to a virtual intermediate state by absorption (or emission) of one phonon and then from the virtual state to the final state by emission (or absorption) of the second phonon[63]. This process requires presence of phonons and the probability to find the phonons rapidly increases with temperature.

In contrast to one-phonon relaxation processes, two-phonon processes occur even when the initial and final states are degenerate. The relaxation rate is proportional to the product of two Bose-Einstein occupation probabilities because the relaxation is accomplished by absorbing one phonon and emitting another one. The energies of the phonons differ by the value of the hole Zeeman splitting. We neglect this difference and fit the temperature dependences of $\alpha(T)$ and $1/\tau_{s0}(T)$ in Fig. 4-15 using the following expression:

$$\alpha(T) = A_\alpha + B_\alpha \frac{\exp(E_\alpha/k_B T)}{[\exp(E_\alpha/k_B T) - 1]^2} \tag{4.2}$$

$$\frac{1}{\tau_{s0}(T)} = A_0 + B_0 \frac{\exp(E_0/k_B T)}{[\exp(E_0/k_B T) - 1]^2} \tag{4.3}$$

The fit parameters are $A_\alpha = 0.015$ ns^{-1}T^{-2} and $B_\alpha = 0.0138$ ns^{-1}T^{-2} for α and $A_0 = 0$ ns^{-1} and $B_0 = 0.003$ ns^{-1} for $1/\tau_{s0}$. Note that $A_\alpha \neq 0$ describes spin relaxation mechanisms which are different from the two phonon assisted process considered above. The fit also gives the energies of the phonons $E_\alpha = 0.6$ meV and $E_0 = 0.2$ meV participating in the spin relaxation process.

The small energies of the phonons participating in the spin relaxation suggest that these phonons are quantized acoustical phonons of the CdS shell. One can estimate the energy of these phonons assuming that they are vibrational eigenmodes of the CdS sphere with 12.5 nm radius[76,92]. We neglect effects of the CdSe core since it represents less than 1% of the NC volume. Using a longitudinal sound velocity of CdS: $c_l = 4289\,\mathrm{m{\cdot}s^{-1}}$, we find 0.67 meV and 0.25 meV for the $l = 0$ and $l = 2$ eigenmodes, respectively. These energies are in good agreement with the activation energies extracted from the fit. The spin relaxation rate described by Eq. (2.51) with coefficients $\alpha(T)$ and $1/\tau_{s0}(T)$ evaluated from Eq. (4.3) indeed reproduces ther measured T^2 dependence when $k_B T \gg E_\alpha > E_0$.

4.5 Shell thickness dependence

Finally, we discuss methods to distinguish neutral and charged NCs. The transition from neutral NCs to charged NCs can be clearly seen from the shell thickness dependence of PL decay and time-resolved DCP. Figure 4-16 shows the PL decay

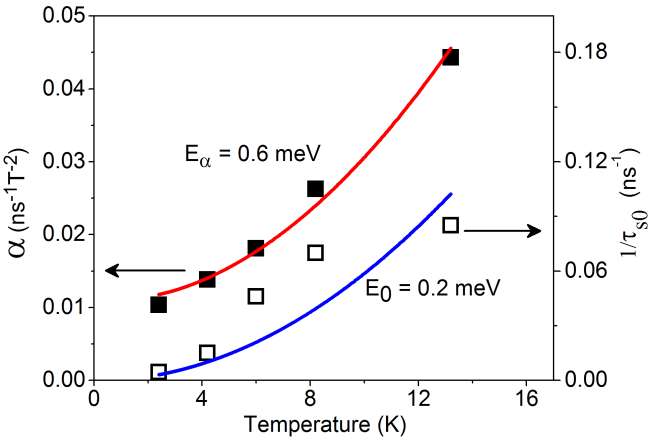

Figure 4-15: Temperature dependences of $\alpha(T)$ (closed squares) and $1/\tau_{s0}(T)$ (open squares) that determine the spin relaxation time τ_s in thick-shell 2.5/10 CdSe/CdS NCs. Red and blue lines show temperature dependences calculated according to Eqs. (4.2) and (4.3), respectively. Calculations were done using activation energies of $E_\alpha = 0.6\,\text{meV}$ and $E_0 = 0.2\,\text{meV}$. Other fit parameters are given in text.

of CdSe/CdS NCs with a core radius of 2.5 nm and shell thicknesses from 2 nm to 10 nm at $T = 4.2$ K. It can be seen that PL decays of all samples consist of a fast component and a slow component. With the increase of the shell thickness, the slow component (~ 100 ns) originating from the recombination of dark excitons in neutral NCs remains constant for any shell thickness, while the short component lengthens from < 1 ns to 6 ns (see the insert). Since the short component in PL decay of samples with thinnest shell (black line) and thickest shell (blue line) is from bright excitons and trions respectively. The evolution of the short component with the increase of shell thickness reflects the increasing probability that a NC is charged. Such evolution can also be seen from the shell thickness dependence of time-resolved DCP.

Figure 4-17(a) shows the time-resolved DCP of CdSe/CdS core/shell NCs with different shell thicknesses measured at $B = 3$ T and $T = 4.2$ K. The DCP rise time of thin-shell (< 5 nm) NCs is quite short (< 3 ns). With increasing shell thickness, the rise time becomes significantly longer (32 ns for the 10 nm shell). Figure 4-17(b) shows the shell-thickness dependence of τ_s^{exp} for the CdSe/CdS NCs at different magnetic fields.

Two types of spin relaxation behavior can be identified from Fig. 4-17. The first one is seen when the shell thickness is less than 5 nm. In this case, the DCP rise time is quite fast (< 3 ns) and increases slowly with increasing shell thickness. The second regime occurs when the shell thickness is larger than 5 nm. Here the DCP rise time is much longer and increases much faster with increasing shell thickness. Since NCs with thin shell (2 nm) are neutral and NCs with thick shell (10 nm) are charged, as we have proved in this paper, it can be concluded that permanent charging of NCs occurs when the shell thickness is between 4 and

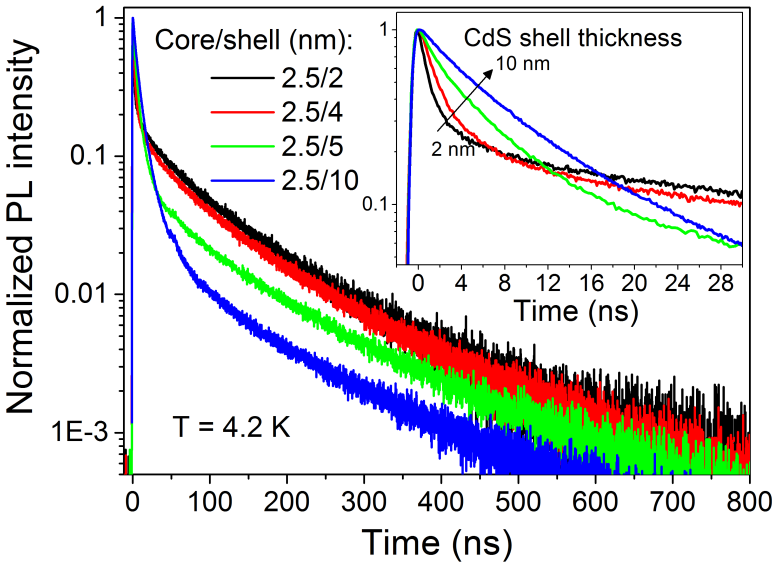

Figure 4-16: Shell thickness dependences of the PL decay of CdSe NCs at $T = 4.2$ K. Insert: PL decays in the first 30 ns.

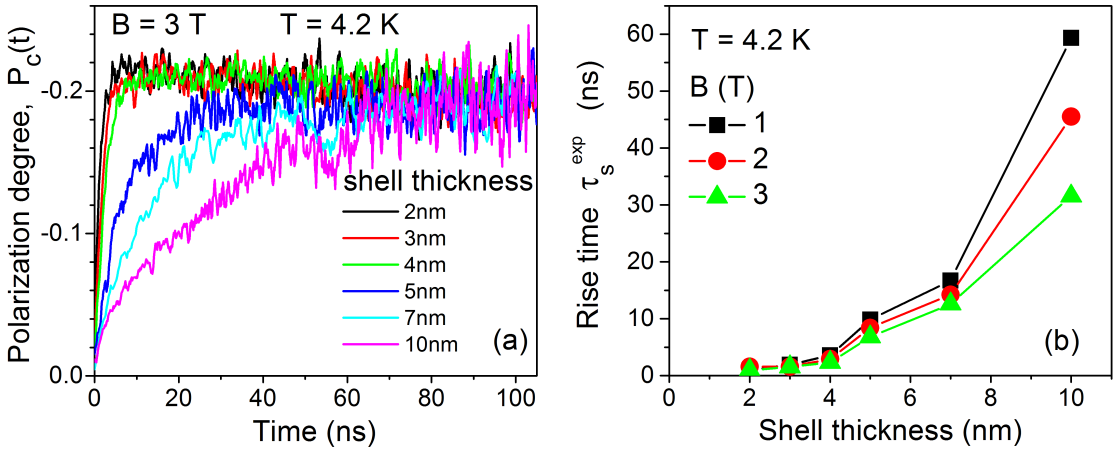

Figure 4-17: (a) Time-dependent DCP of CdSe/CdS NCs with shell thicknesses varying from 2 to 10 nm, NC core radius is 2.5 nm. (b) Dependence of DCP rise time, τ_s^{exp}, on the shell thickness at magnetic fields $B = 1, 2$ and 3 T.

5 nm. The majority of NCs with thin shell are neutral and characterized by a short DCP rise time. By contrast, the majority of NCs with thick shell are charged and have much longer DCP rise time. Therefore, the DCP rise time can be used as a criterion to distinguish neutral NCs and charged NCs.

The conclusion such a short rise time of DCP is a characteristic property of neutral excitons is in complete agreement with previous measurements of DCP in CdSe/ZnS NCs[25,60]. It is well known that PL in these NCs is controlled by neutral excitons. The rise of the DCP measured in these NCs after a short unpolarized pulse excitation occurs on the time scale less than 1 ns at low temperatures and become unmeasurable above 40 K[60].

4.6 Summary

To summarize, we have measured the polarization-resolved PL and PL decay of CdSe/CdS colloidal NCs in high magnetic fields at various temperatures. By comparing the recombination dynamics and FLN spectra of thin-shell and thick-shell CdSe/CdS NCs, we demonstrate that the PL of thick-shell NCs arises from charged excitons. The negative sign of the trion charge is identified by means of magneto-optical studies. A theory for describing the temporal dependence of the PL polarization degree for ensemble of randomly oriented NCs has been developed and provides an excellent description of the experimental data. Comparison of the experimental data with theory shows that ensemble measurements of the time dependent polarization provide an independent access to NCs with arbitrary oriented crystal axes.

We also report on a direct measurement of the spin relaxation rate of negatively charged excitons in thick-shell CdSe/CdS NCs. The spin relaxation rate increases quadratically with magnetic field and temperature. A two-phonon-assisted spin-flip relaxation mechanism between hole spin sub-levels mixed by a magnetic field is suggested for explanation of the observed phenomena. The mechanism provides a complete description of the magnetic field and temperature dependences of the spin relaxation time and suggests that confined phonons of the CdS shell are responsible for the trion spin relaxation. Finally, we show that the rise time of DCP can be used as a criterion to distinguish neutral NCs and charged NCs, which could be useful for NC fabrication.

Chapter 5

Magneto-optical properties of CdTe colloidal nanocrystals

Following the study of core/shell CdSe/CdS nanocrystals (NCs), to understand how materials influence optical properties of colloidal NCs, cubic CdTe NCs were investigated using similar experimental techniques. In this chapter, firstly we focus on spin relaxation of excitons between two Zeeman-split levels in CdTe NCs. The spin relaxation time was measured by polarization-resolved PL decay technique and compared with that of CdSe NCs. Then, spin relaxation mechanisms are discussed. Additionally, the observed low PL polarization degree of CdTe NCs in high magnetic field is explained based on a model involving two types of CdTe NCs with different geometries. Furthermore, in the study of spin dynamics in CdTe NCs, we observed the Förster resonant energy transfer (FRET) between CdTe NCs. A detailed study of the effect of magnetic field on the Förster resonant energy transfer in CdTe NCs was performed. By fitting the magnetic field dependence of photoluminescence (PL) decay of CdTe NCs based on a model proposed by A. V. Rodina (see Sec. 2.7), it is found that the Förster energy transfer was enhanced by external magnetic field.

5.1 Experimentals

Thiol-capped CdTe colloidal NCs were synthesized as described in Ref. 10. The average core diameter of the two studied sample is 3.4 and 3.7 nm respectively. For the optical experiments performed at cryogenic temperatures the solvent with CdTe NCs was drop-casted on a glass slice and dried. The resulting film composed of ensemble of NCs has inhomogeneous concentration of NCs, and selecting different places on the sample with the focused laser beam ensembles with various NC densities can be studied. Information on the relative changes in NC concentration in different places can be received from the photoluminescence intensity.

The glass slice was mounted in a sample holder and inserted into a cryostat equipped with a 15 T superconducting magnet. Magnetic field, **B**, was applied in the Faraday geometry, it was perpendicular to the glass slice and parallel to the light wave vector. A circular polarizer inserted between the sample and the detection fiber allowed us to detect the σ^+ and σ^- polarized PL by alternating the magnetic field direction. The sample was in contact with helium gas so that the bath temperature could be varied from $T = 4.2$ up to 300 K.

Photoluminescence was excited and collected through multimode optical fibers. The collected signal was dispersed with a 0.55 m spectrometer. Time-integrated PL spectra were measured under continuous-wave (CW) laser excitation with a photon energy of 3.33 eV (wavelength 372 nm) and detected with a liquid-nitrogen-cooled charge-coupled-device camera. We denote them as steady-state PL spectra.

For time-resolved measurements the sample was excited by a picosecond pulsed laser (photon energy 3.06 eV, wavelength 405 nm, pulse duration 50 ps, repetition frequency 150 to 500 kHz). PL signal was sent through spectrometer and detected by an avalanche photodiode (time response 50 ps) connected to a conventional time-correlated single-photon counting module. Instrument response function of this setup was limited by the optical fiber dispersion to 800 ps. All measurements were performed at low excitation density of 0.1 mW/cm^2 to suppress any multiexcitonic contribution in the emission spectra.

5.2 Spin dynamics in CdTe colloidal NCs

Photoluminescence bands of 3.4 nm CdTe NCs measured under unpolarized CW excitation at low temperature of 4.2 K are shown in Fig. 5-1(a). At a zero magnetic field the band maximum has an energy of 1.988 eV and a full width at half maximum (FWHM) of the band caused by the size dispersion of nanocrystals is 120 meV.

In external magnetic fields the PL becomes circular polarized with the intensity redistribution in favor of the σ^- polarized component, i.e. the sign of the circular polarization degree defined by Eq. (2.25) is negative. This polarization is caused by exciton thermalization on the Zeeman-split levels and it reaches a value of $P_c^{\rm int} = -0.28$ at $B = 15$ T. Spectral dependence of $P_c^{\rm int}$ shown in Fig. 5-1(b) is about constant having some increase only for the high energy tail of the PL band and in magnetic fields exceeding 6 T.

Figure 5-1(c) shows the magnetic field dependence of the PL band peak position for σ^+ and σ^- polarizations. The energy splitting between two components reaches 2.3 meV at $B = 15$ T. The unusual here is the fact that the σ^- component that has stronger intensity is higher in energy. Such a behavior has been observed also for CdSe NCs[60,80], but the plausible explanation is still missing and further studies are

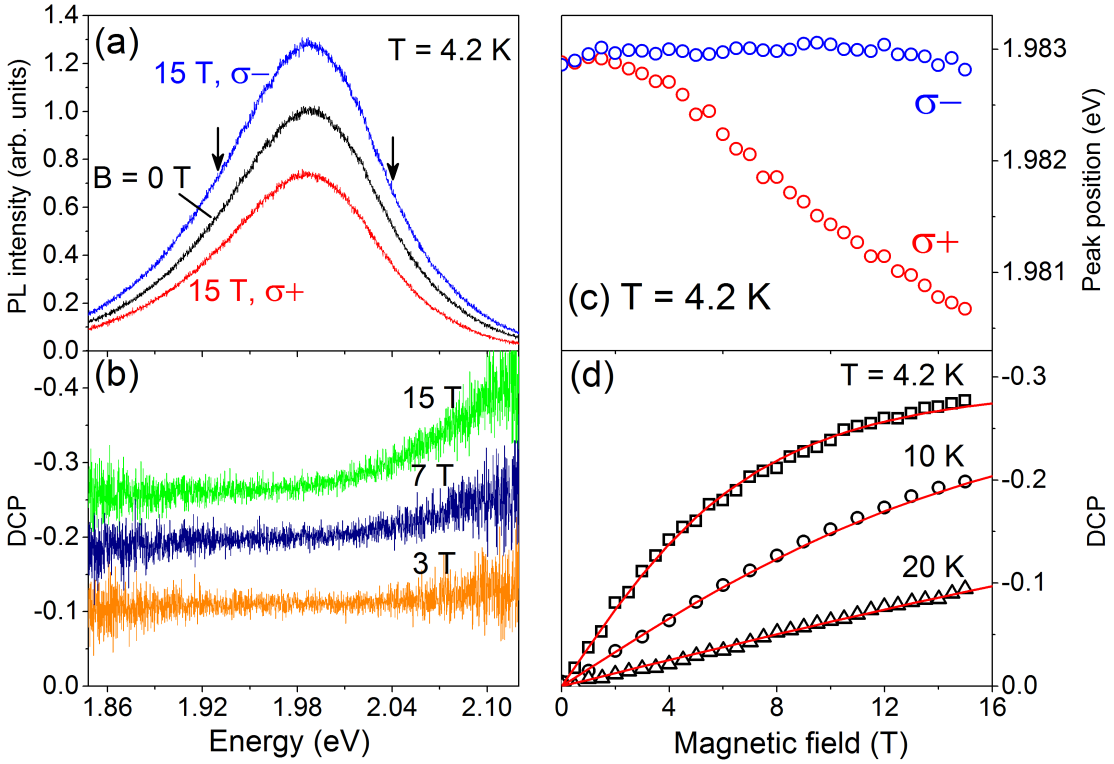

Figure 5-1: (a) Polarization-resolved PL spectra of 3.4 nm CdTe NCs at $B = 0$ (black) and 15 T (red for σ^+ polarization and blue for σ^-). Black arrows indicates positions where the PL decay shown in Fig. 5-9 was measured. (b) Spectral dependence of DCP at $B = 3$, 7 and 15 T and $T = 4.2$ K. (c) Magnetic field dependence of peak position of the σ^+ and σ^- components of the PL spectrum. (d) Magnetic field dependence of the spectrally integrated DCP measured at $T = 4.2$, 10 and 20 K.

needed. Tentative mechanism might be related to the spin flip processes involving dangling bonds on NC surface.

Magnetic field dependences of the spectral- and time-integrated degree of circular polarization (DCP) measured at three different temperatures are given in Fig. 5-1(d). They have a typical behavior for the field-induced DCP with linear increase in low magnetic fields and saturation in a high magnetic field limit, the later is clearly seen for $T = 4.2$ K. Decrease of the DCP at elevated temperatures is also typical, as the occupation of Zeeman levels is controlled by a ratio of the Zeeman splitting to $k_B T$[78]. It should be noticed that although the DCP at 4.2 K already saturate at 15 T, the saturation level (-0.3) is much lower than theoretically calculated saturation level of DCP of an ensemble of randomly oriented spherical or prolate CdTe NCs with cubic structures (-0.75).

One possible explanation for the low saturation level of DCP involves a model proposed by Rodina which takes into account the influence of shape anisotropy on exciton fine structure. Assume the ensemble of CdTe NCs consist of NCs with different shapes. It can be seen from the exciton fine structure of cubic CdTe NCs (Fig. 2-3) that the spin of the ground state of oblate CdTe NCs is 0. In this

case, the ground state does not split in external magnetic field and the PL circular polarization degree from this type of NCs is 0. By contrast, the ground state of prolate NCs is ± 2 which does spit in external magnetic field and give non-zero PL circular polarization degree. The low saturation level of DCP results from the zero PL circular polarization degree of oblate CdTe NCs.

According to this model, the exciton g-factor can be extracted by fitting the magnetic field dependence of DCP. To fit the DCP, one has to take into account the contribution from both of two types of NCs. Here we ignore the contribution from spherical NCs because practically perfectly spherical NCs are rather rare. In non-spherical CdTe NCs with cubic crystal structure, the total momentum of hole is aligned along a quantization axis originating from the shape anisotropy. Due to the exchange interaction between hole and electron, the electron spin is also pined along this quantization axis. Therefore, the Zeeman splitting is not only dependent on the g-factor of excitons but also dependent on the angle between the quantization axis and magnetic field. Furthermore, since the quantization axis is randomly oriented, the DCP of an ensemble of NCs has to be integrated overall angles. The time-integrated DCP of an ensemble of randomly oriented prolate CdTe NCs with cubic crystal structures has the same form as that of an ensemble of oblate CdSe NCs with hexagonal crystal structures (see Eq. (2.43)). As one can see from Eq. (2.43), the DCP depends on both the dynamical factor $\tau_\mathrm{r}/(\tau_\mathrm{r}+\tau_\mathrm{s})$ and on the equilibrium spin polarization $\rho_0 = \tanh(\Delta E/2k_\mathrm{B}T)$, where τ_r is the radiative decay time of excitons and τ_s is the spin relaxation time. Time-resolved experiments presented below show that in the studied CdTe NCs $\tau_\mathrm{s} \ll \tau_\mathrm{r}$ and, therefore, the equation for time-integrated DCP $P_\mathrm{c}^\mathrm{int}(B)$ of prolate CdTe NCs is reduced to the equation for thermal equilibrium DCP $P_\mathrm{c}^\mathrm{eq}(B)$ (see Eq. (2.44)). Since the ground state of oblate CdTe NCs does not split in magnetic field, oblate NCs only contribute to the total PL intensity. Based on the discussion above and take into account the non-radiative channel, the time-integrated DCP $P_\mathrm{c}^\mathrm{int}(B)$ of an ensemble of randomly oriented cubic CdTe NCs with oblate and prolate shape can be written as:

$$P_\mathrm{c}^\mathrm{int}(B,T) = -\frac{\int_0^1 2x\rho_0(B,x,T)\eta_\mathrm{p}(B,x)dx}{(1+q\eta_\mathrm{o}(B,x))\int_0^1(1+x^2)\eta_\mathrm{p}(B,x)dx} \tag{5.1}$$

where q is the ratio of the number of oblate NCs to that of prolate NCs. $\eta_\mathrm{o,p} \propto (1+\tau_\mathrm{r}/\tau_\mathrm{nr})^{-1}$ is the quantum efficiency of oblate NCs and prolate NCs[25]. Next, we discuss two extreme cases. Firstly, in the limit of high quantum yield ($\tau_\mathrm{r} << \tau_\mathrm{nr}$), $\eta_\mathrm{o,p}$ is independent on magnetic field and consequently independent on x, so Eq. (5.1) is reduced to:

$$P_{\mathrm{c}}^{\mathrm{int}}(B,T) = -\frac{\int_0^1 2x\rho_0(B,x,T)dx}{(1+q^*)\int_0^1(1+x^2)dx} \tag{5.2}$$

where $q^* = q\eta_{\mathrm{o}}/\eta_{\mathrm{p}}$. The time-integrated DCP measured at three temperatures can be well fitted with a fixed q^* and variable g-factor using Eq. (5.2) (see red lines in Fig. 5-1(d)). The fitting gives a g-factor of 2.4 at 4.2 K, 2.5 at 10 K and 1.9 at 20 K. The g-factor at 4.2 K most probably corresponds to dark-exciton g-factor. The decrease of the g-factor at high temperature may be due to the thermal mixing of bright- and dark-exciton states. The fitted factor q^* is 1.5.

Secondly, in the limit of low quantum yield ($\tau_{\mathrm{r}} >> \tau_{\mathrm{nr}}$), $\eta_{\mathrm{o,p}}$ is proportional to $\eta^*_{\mathrm{o,p}}(1-x^2)$[25], and Eq. (5.1) has the following form:

$$P_{\mathrm{c}}^{\mathrm{int}}(B,T) = -\frac{\int_0^1 2x\rho_0(B,x,T)(1-x^2)dx}{(1+q^{**})\int_0^1(1+x^2)(1-x^2)dx} \tag{5.3}$$

where $q^{**} = q\eta^*_{\mathrm{o}}/\eta^*_{\mathrm{p}}$. The fitting with Eq. (5.3) gives a similar g-factor as that with Eq. (5.2). The g-factor is 2.9 at 4.2 K, 3 at 10 K and 2.3 at 20 K. The fitted factor q^{**} is 1. By comparing these two cases, it can be concluded that the exciton g-factor of 3.4 nm-diameter CdTe NCs at low temperature (4.2 K) is in the range from 2.4 to 2.9. It is noteworthy that by knowing the ratio of the quantum efficiency of oblate NCs to that of prolate NCs, the ratio of the number of oblate NCs to that of prolate NCs can be obtained from q^* and q^{**}. Therefore fitting the magnetic field dependence of DCP provides a simple optical method to evaluate the ratio of oblate NCs to prolate NCs in an ensemble of CdTe NCs.

Another possible explanation of the low DCP is that we only have prolate dots with lowest dark ± 2 state, but this state can be also coupled to the optically active 0^U exciton state by phonons (see exciton fine structure in Fig. 2-3(c)). Then the respective transitions only give contribution to the total intensity but not to the polarization. The total intensity is $2\int_0^1(1-x^2)dx = 4/3$ – the same as $\int_0^1(1+x^2)dx$. So for the first limit case $\eta_{\mathrm{o,p}}$ = constant the results will be the same as in the model with oblate NCs, but q will be the ratio of the coupling parameter multiplied by the oscillator strength for the 0^U state and the sum of two optically active 1^L and 1^U states.

Next, let us present the experimental data for the exciton recombination dynamics. In order to exclude from consideration effects related to the Förster resonant energy transfer we measured the spectrally integrated recombination dynamics in the CdTe NCs, see Fig. 5-2. It is known that FRET modifies the spectral dependences of the emission dynamics[36,48,49,50], such appearances have been found for the studied sample and will be reported elsewhere.

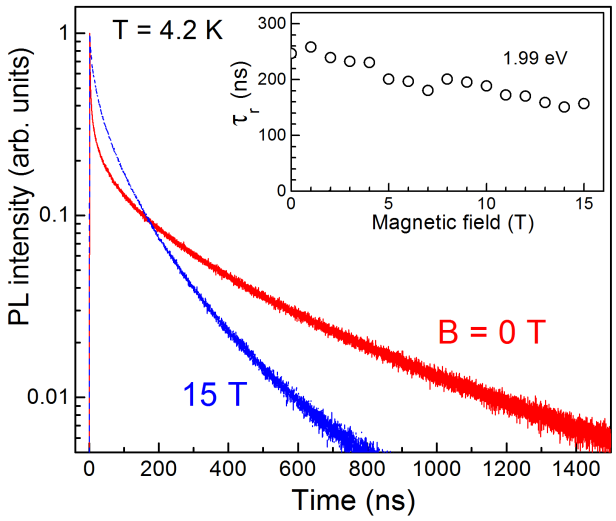

Figure 5-2: Dynamics of spectrally integrated PL intensity of 3.4 nm CdTe NCs in different magnetic fields. Magnetic field dependence of the recombination time for the slow component measured at the central position 1.99 eV of PL spectra is shown in insert.

At zero magnetic field and $T = 4.2$ K the exciton PL dynamics shown by a red color in Fig. 5-2 has a multiexponential decay. Its fast initial component with a characteristic time of 2 ns is dominated by the exciton thermalization from bright into dark state. And its slow component with a time of about 260 ns corresponds to the lifetime of dark excitons, which recombination is partially allowed due to a weak mixing of the dark and bright-exciton states, e.g. caused by NC imperfections and surface states. Note, that the PL intensity amplitude of the slow component is smaller than that for the fast component, but being integrated at much longer time interval its provides the dominating contribution to the time-integrated PL. Therefore, it is the decay of the slow component that should be taken into account for the evaluation of the time-integrated DCP.

With increasing magnetic fields up to 15 T the slow decay component measured at the central position (1.99 eV) of the PL spectra steadily shortens from 260 down to 150 ns, see insert in Fig. 5-2, and the fast component reduces in amplitude to vanishing. Such a behavior is characteristic for colloidal NCs and is due to the magnetic-field-induced mixing of the bright- and dark-exciton states[25,60,84].

Experimental results for the exciton spin dynamics are collected in Fig. 5-3. Here recombination dynamics of two circularly polarized components measured at the PL band maximum (1.99 eV) at $B = 15$ T are shown in panel (a). One can see that the intensity difference between the components is established shortly after the excitation pulse and then both components decay about parallel to each other. The initial dynamics during 40 ns is given in more detail in Fig. 5-3(b) together with the DCP dynamics calculated with Eq. (2.24). Small rise in PL intensity visible for the σ^- polarization during initial 10 ns is due to the energy transfer (ET), see Sec. 5.3 for details. The DCP has a fast initial increase from a zero level

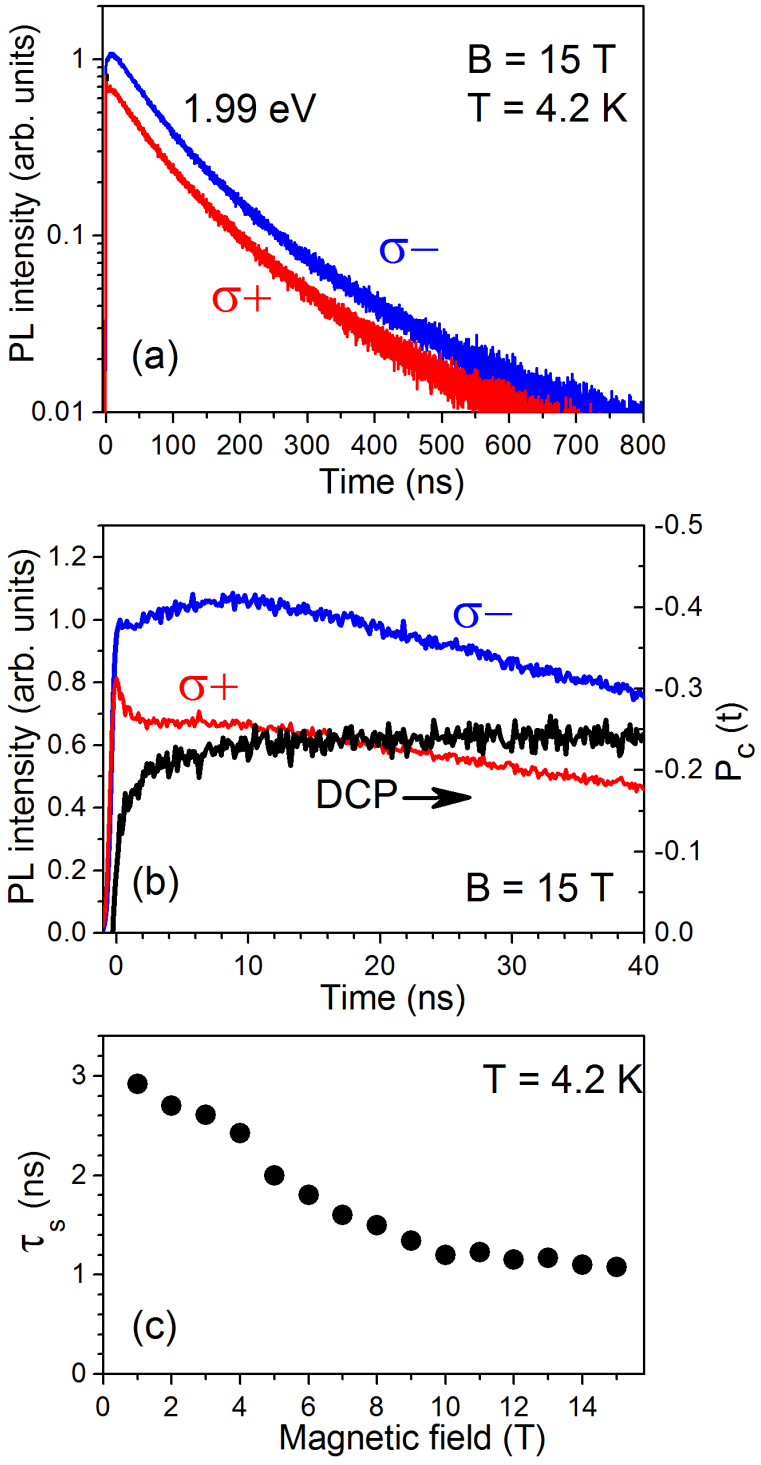

Figure 5-3: Exciton spin dynamics of 3.4 nm CdTe NCs. Recombination dynamics of two circular polarized components measured at PL maximum at $B = 15$ T (a) in logarithmic scale at large time interval and (b) in linear scale at initial times also with calculated DCP. (c) Magnetic field dependence of the exciton spin relaxation time evaluated from the DCP dynamics.

to about −0.20 during 4 ns and then slower saturation at −0.25 on which it stays for further delays up to one microsecond.

The rise time of time-resolved DCP is related to the spin relaxation time of excitons thermalized on the Zeeman-split spin levels. Being fitted with the following function:

$$P_{\mathrm{c}}(t) = P_0\,[1 - \exp(-t/\tau_{\mathrm{s}})] \tag{5.4}$$

where P_0 is the saturation level of time-resolved DCP, it allows us to evaluate the exciton spin relaxation time τ_{s}. Figure 5-3(c) shows the magnetic field dependence of τ_{s}. Being 3 ns at $B = 1$ T it gradually decreases down to 1 ns at 15 T. Note that the spectral dependence of τ_{s} was rather weak, e.g. at $B = 15\ T$ it varies from 0.9 ns at a high energy side up to 1.7 ns at a low energy side of the PL band.

The measured values of the exciton spin relaxations times in CdTe NCs are similar to the one reported earlier for CdSe/ZnS NCs[25,60], where the times shorter than one ns have been found in $B = 12$ T and to neutral CdSe/CdS NCs with CdS shells thinner than 4 nm (see Fig. 4-17), which may suggests that spin relaxation mechanisms of excitons are the same in neutral CdSe and CdTe NCs. Note that in CdSe/CdS NCs with the shells thicker than 5 nm emission is dominated by negatively charged excitons (trions) having rather long spin relaxation up to 60 ns at $B = 1$ T and $T = 4.2$ K.

It is also interesting to compare colloidal NCs with epitaxial quantum dots (QDs) grown by molecular-beam epitaxy. Contrary to our observation of decreasing τ_s with growing magnetic fields, considerably shorter times have been measured for epitaxial CdTe quantum dots, which increasing from 40 ps at zero field to 300 ps at $B = 10$ T[93]. Such a behavior has been attributed to hyperfine interaction of the exciton spin with the nuclear spins. The different behavior observed in CdTe colloidal NCs may be explained as follows: In small neutral colloidal NCs, the spin relaxation of excitons between $S = \pm 1$ states is mainly driven by long-range electron-hole exchange interaction and additionally exciton-phonon interaction[94,95,96]. One phonon-assisted spin flip of excitons requires that the energy of phonon matches the energy difference between two Zeeman-split levels. Since the Zeeman splitting increases with magnetic field and the phonon density in CdTe increases with the phonon energy, it is easier for excitons to find phonons with suitable energy to flip the spin in larger magnetic field. Therefore, the spin relaxation rate increases with the increase of magnetic field.

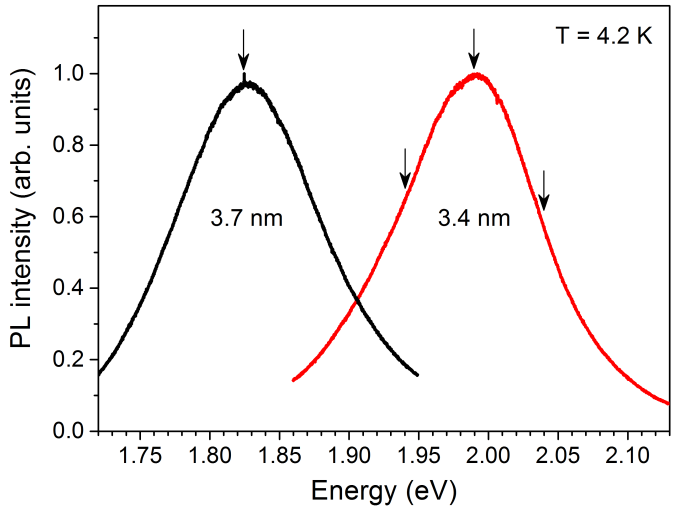

Figure 5-4: Normalized steady-state PL spectra of 3.4 nm and 3.7 nm CdTe NCs measured at $T = 4.2$ K. Arrows indicate positions where PL dynamics shown in Figs. 5-10 and 5-11 is measured.

5.3 Förster energy transfer in an ensemble of CdTe NCs

In the study of spin dynamics of CdTe NCs, it was found that the PL decay at different spectral positions from an ensemble of closely packed CdTe NCs showed dramatic different behavior across the PL band. This results from the Förster resonant energy transfer between CdTe NCs (see also Sec. 2.7). In this section, we present the results of a detailed study of the effect of magnetic field and temperature on energy transfer in an ensemble of CdTe NCs.

5.3.1 Magnetic field and temperature dependence of PL dynamics

Steady-state PL spectra of 3.4 and 3.7 nm CdTe NCs measured under CW excitation at $T = 4.2$ K are shown in Fig. 5-4. Their peak positions are at 1.83 eV for 3.4 nm NCs and 1.99 eV for 3.7 nm NCs. The spectra of both samples are rather broad with a full width at a half maximum (FWHM) of ~ 120 meV, which evidences the considerable NC size dispersion.

Exciton recombination dynamics in NCs is well characterized by the spectrally integrated time-resolved PL. Note, that for CdTe NCs no dispersion of the recombination dynamics has been found in ensemble of noninteracting NCs, where the energy transfer has been absent[48]. Figure 5-5 shows the integral PL decay obtained by summing the PL decay measured at about 20 spectral energies across the whole PL band of 3.4 nm NCs. At a room temperature the PL decay can be fitted by biexponential functions ($\tau_{\mathrm{rf}} = 6$ ns, $\tau_{\mathrm{rl}} = 22$ ns). The shorter com-

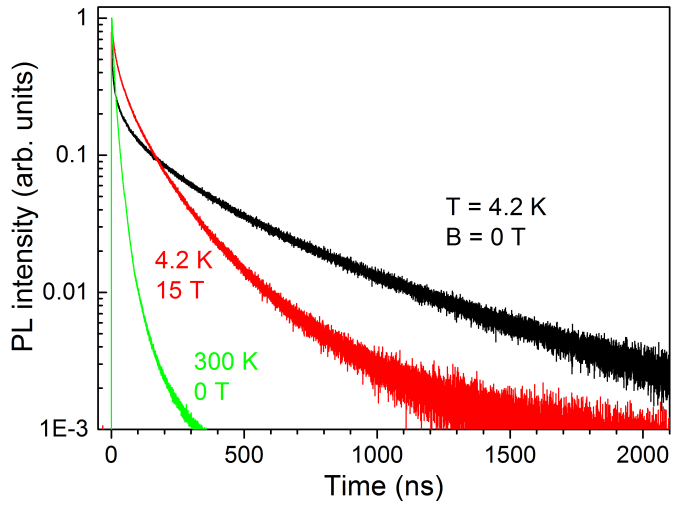

Figure 5-5: Recombination dynamics of spectrally integrated PL intensity in 3.4 nm CdTe NCs measured at various temperatures and magnetic fields.

ponent reflects the influence of energy transfer. The longer component originates from thermally mixed bright- and dark-exciton states. The latter is evidenced by the fact that the PL decay at the very low energy side can be fitted by a single exponential function ($\tau_r = 26$ ns). With the temperature decrease down to 4.2 K the decay shows multiexponential behavior due to excitons thermalization in the optically-forbidden (dark) state, which is the lowest exciton state in NCs. It is well established that the very fast initial decay with a time of $\tau_{rf} \sim 2$ ns is related to the optically-allowed (bright) exciton and is dominated by the fast scattering from the bright to dark state and has some contribution of the radiative recombination of the bright exciton[27,59,84]. The slow decay process with the time of 230 ns is due to recombination of the dark excitons. Being optically forbidden in electric-dipole approximation, the dark excitons have a finite recombination rate provided by weak admixing of the bright-exciton state due to structural and surface imperfections or by coupling to bright states via phonons.

An external magnetic field induces mixing of the bright- and dark-exciton states, which results in the vanishing of the fast decay component and the shortening of the slow component. Such a behavior, well established for CdSe and CdTe NCs[25,84] is observed for the studied sample. In a magnetic field of 15 T the fast component vanishes and the slow component shortens down to 142 ns.

We turn now to the experimental results which evidences the presence of the energy transfer in the studied CdTe NC solids. Figure 5-6 compares the steady-state (solid lines) and time-resolved (dots and lines) PL spectra measured at a zero time delay just after the excitation pulse in 3.4 nm NCs. Results for two sample areas with high concentration (red curves) and low concentration (black curves) are shown. Relative PL intensity in these points differs by 2.5 times. Time-resolved spectra from high- and low-concentration areas are similar to each other,

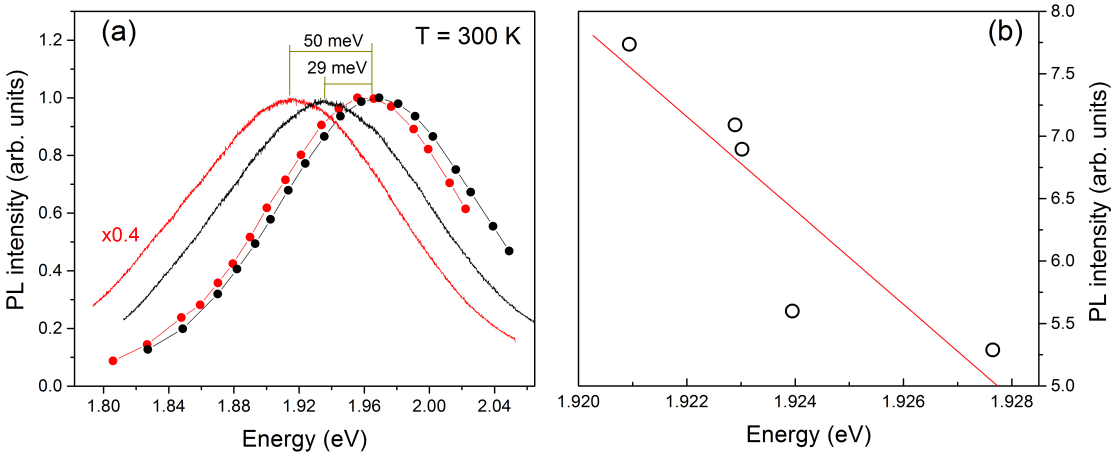

Figure 5-6: (a) Normalized time-resolved (dots and lines) and steady-state (solid lines) PL spectra measured at high-concentration (red) and low-concentration (black) areas of sample with 3.4 nm CdTe NCs. (b) PL intensity versus the peak position of the steady-state PL spectra measured at areas with different concentrations of CdTe NCs. Line is linear interpolation.

indicating the same NC size dispersion in these areas. Note, that these spectra, being measured at very short delays, are not contributed by the energy transfer and give us the information on the density of states in the ensemble of NCs.

Steady-state PL spectra, however, are shifted to the lower energies from the time-resolved ones. And this shift is larger in the area with higher NC concentration reaching 29 and 50 meV in low- and high-concentration areas, respectively. In general, such a shift can be induced by the energy transfer, but also by the spectral dependence of PL dynamics across the emission band. As the second reason is not actual for CdTe NCs[48], we attribute this shift to the energy transfer. Higher concentration of NCs corresponds to smaller distance between them. Therefore, the higher the concentration is, the more efficient the Förster energy transfer and, consequently, the lager shift between time-resolved and steady-state PL spectra is expected.

A systematic correlation between NC concentration and the shift value of the steady state PL measured at different sample areas is shown in Fig. 5-6(b). Here the PL intensity of is plotted against the peak energy. One can see that the stronger PL intensity corresponds to the areas with lower peak energy, i.e. with larger shift. This correlation agrees with the Förster mechanism for the energy transfer and is in line with the experimental results of Ref. 49.

Time evolution of PL spectra measured at different time delays is presented in Fig. 5-7 for two temperatures of $T = 4.2$ and 300 K. Strong spectral shift with increasing delay is very prominent for both temperatures. For comparison the steady-state PL spectra are also shown by a solid red lines. At $T = 4.2$ K emission intensity decreases with time monotonically and the maximum of the spectrally resolved PL spectra shifts from 2.05 eV at $t = 0$ ns to 2.01 eV at 70 ns, see

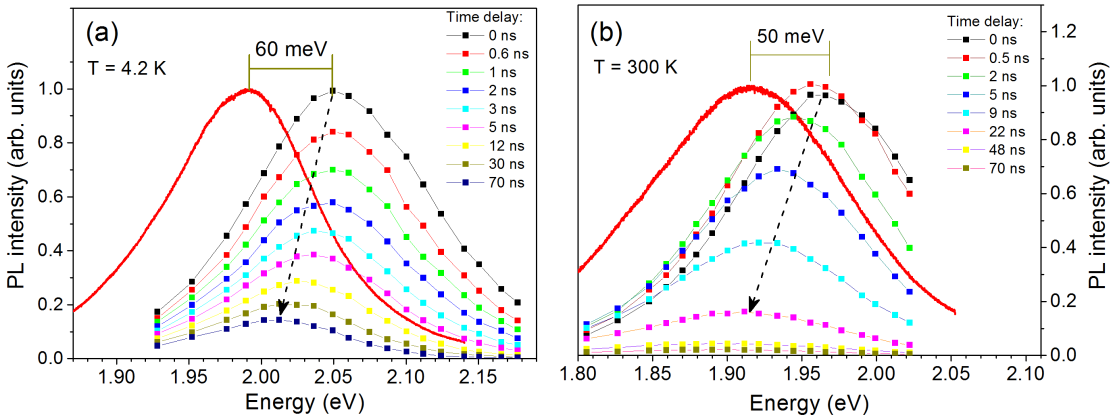

Figure 5-7: Steady-state PL spectra (solid red lines) and time-resolved PL spectra (dots and lines) of 3.4 nm CdTe NCs measured at (a) $T = 4.2$ K and (b) 300 K.

Fig. 5-7(a). Similar behavior is observed at a room temperature, the time-resolved spectra shifts from 1.96 eV at 0 ns to 1.92 eV at 70 ns. An important appearance related to the energy transfer is seen at a room temperature in Fig. 5-7(b). Namely, the PL intensity varies nonmonotonically at the low energy tail of the emission band. It increases during the several nanoseconds after the excitation and only then turn to decay. In more detail this behavior will be shown below in the PL dynamics measured at different spectral energies.

Figure 5-8 shows temporal shifts of PL maxima measured at two sample areas having similar PL intensities. Due to the sample inhomogeneity various experimental sets have been measured at different sample areas, while the characteristic behavior was well reproducible for all areas. For the area 1 the PL spectrum shifts by 47 meV during the first 70 ns at $T = 4.2$ K, see Fig. 5-8(a). The shift becomes larger with the temperature increase and reaches 75 meV at 300 K, indicating more efficient energy transfer. In both cases the fast initial energy shift during first 10 ns is then gradually slows down with a tendency to saturation.

It can be seen from Fig. 5-8(b), that application of the external magnetic field also enhance the energy transfer. The PL shift during the first 70 ns measured at $B = 15$ T (51 meV) is larger than that measured at 0 T (40 meV). The peak position shows fast redshift during the first 10 ns, and then gradually slows down due to the vanishing of energy transfer with time. It is important to note, that the magnetic field enhances the carrier localization and shrinks the exciton wave function. Therefore, the energy transfer mechanisms involving tunneling of the excitons or carriers between NCs are expected to be slowed down in a magnetic field. But not the FRET, which can be enhanced by e.g. magnetic field induced increase of the exciton oscillator strength.

Figure 5-9 shows spectrally resolved PL dynamics of 3.4 nm CdTe NCs measured at $T = 4.2$ K. At a zero magnetic field the PL shows multiexponential decay behavior. At high energy side of emission band, e.g. at 2.08 eV (black line),

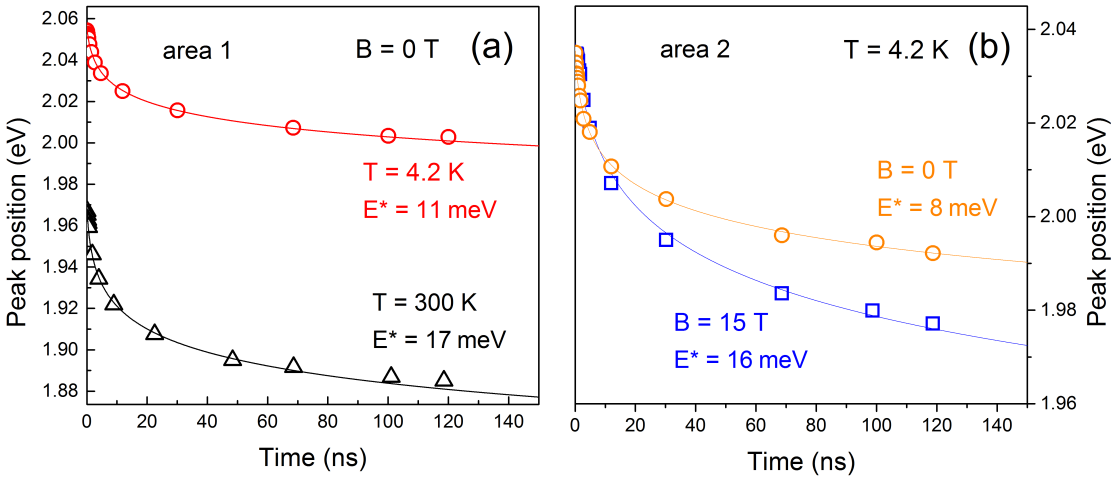

Figure 5-8: Time shift of PL maximum in 3.4 nm CdTe NCs measured for two sample areas at different temperatures and magnetic fields. Experimental data are shown by symbols. Lines are fits according to Eq. (5.8) with characteristic energy E^*.

the decay starts with a very fast component ($\tau_{\mathrm{rf}} \sim 4$ ns) and then followed by a muitiexponential intermediate component finally turning to a very slow component ($\tau_{\mathrm{rl}} \sim 321$ ns). The weight of the intermediate component decreases for lower spectral energies, whereas the slow components is about spectral independent. The fast component can be attributed to bright excitons, their radiative recombination and scattering to the dark states. The intermediate component is most likely related to the FRET from smaller NCs to larger NCs. And the slow component is due to recombination of the dark excitons.

These dynamics change considerably in external magnetic fields, compare Figs. 5-9(a) and 5-9(b). In magnetic field bright- and dark-exciton states are mixed, which results in the vanishing of the fast component and the shortening of the slow one. For example, the slow component of the PL decay at 2.08 eV (black line) shortens from $\tau_{\mathrm{rl}} = 321$ to 123 ns. Compared with the PL dynamics measured at the high energy side of PL spectra, the PL decay measured at low energy side shows qualitatively different behavior. The PL dynamics at 1.88 eV (blue line) has a small initial rise and then decays. This rise can be explained only by the energy transfer process in which lager NCs are fed by smaller NCs.

Figure 5-10 shows PL dynamics measured in different magnetic fields at three spectral energies of 3.4 nm NCs, compare with Fig. 5-4. For clarity, Figs. 5-10(d-f) enlarge the initial 50 ns of PL dynamics and show them in linear scale. PL decay at high energy position shows typical for colloidal NCs behavior, see Figs. 5-10(a,d). With increasing magnetic field the fast component vanishes and the slow component shortens due to the mixing of bright- and dark-exciton states. Different behavior is observed at the maximum of PL spectra, see Figs. 5-10(b,e). The PL dynamics at 0 T shows decay in $t \in (5\text{ ns}, 15\text{ ns})$, which slows down with increasing magnetic field and turns into the rise at $B = 15$ T. Such unusual behavior is even

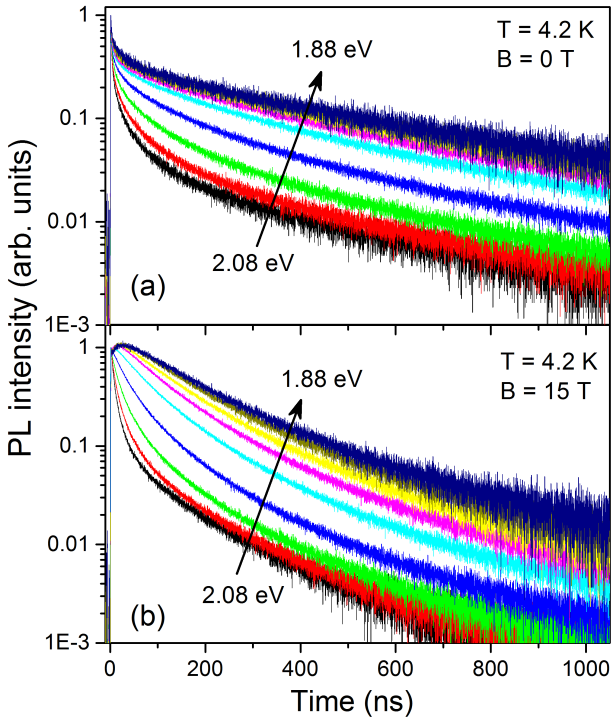

Figure 5-9: Spectrally resolved PL decay of 3.4 nm CdTe NCs measured at (a) $B = 0$ T and (b) 15 T. Spectral range is varied from 1.88 to 2.08 eV. Signals are normalized on there intensities at zero delays, i.e. just after the excitation pulse.

more prominent at the low energy position, see Figs. 5-10(c,f). At $B = 15$ T the PL intensity at $t = 12$ ns is larger than one at $t = 0$ ns.

Qualitatively very similar behavior has been found in 3.7 nm NCs, which PL dynamics during the initial 50 ns measured at the PL maximum of 1.82 eV is presented in Figure 5-11. In panels (a-c) PL dynamics measured at fixed temperatures are compared for different magnetic fields. At $T = 4.2$ K the PL dynamics shows decay behavior at $B = 0$ T. At higher fields the PL intensity in the region in $t \in (5\text{ ns}, 15\text{ ns})$ starts to grow, and at 15 T the decay turns into rise. This behavior is more pronounced at higher temperatures, see Fig. 5-11(b). At 10 K, the decay turns to rise already at $B = 5$ T. At even higher temperature, the fast decay component within the first 5 ns, which can be seen in Figs. 5-11(a,b) disappears and only a slow rise is visible during the first 10 ns. The rise time increases for stronger magnetic fields. In addition to magnetic field, the shape of PL decay is also strongly influenced by temperature. As it is shown in Fig. 5-11(d), PL dynamics at 4.2 K and 10 K starts with a fast decay component, while this fast component becomes invisible at 15 K. Instead, the PL dynamics starts with a rise of PL intensity. At $B = 5$ T the rise of PL intensity becomes more prominent, see Fig. 5-11(e). At $B = 15$ T the PL dynamics at all temperatures shows a rise during the first 15 ns. The fast decay component presented at 4.2 K and 10 K disappears at 15 K, see Fig. 5-11(f).

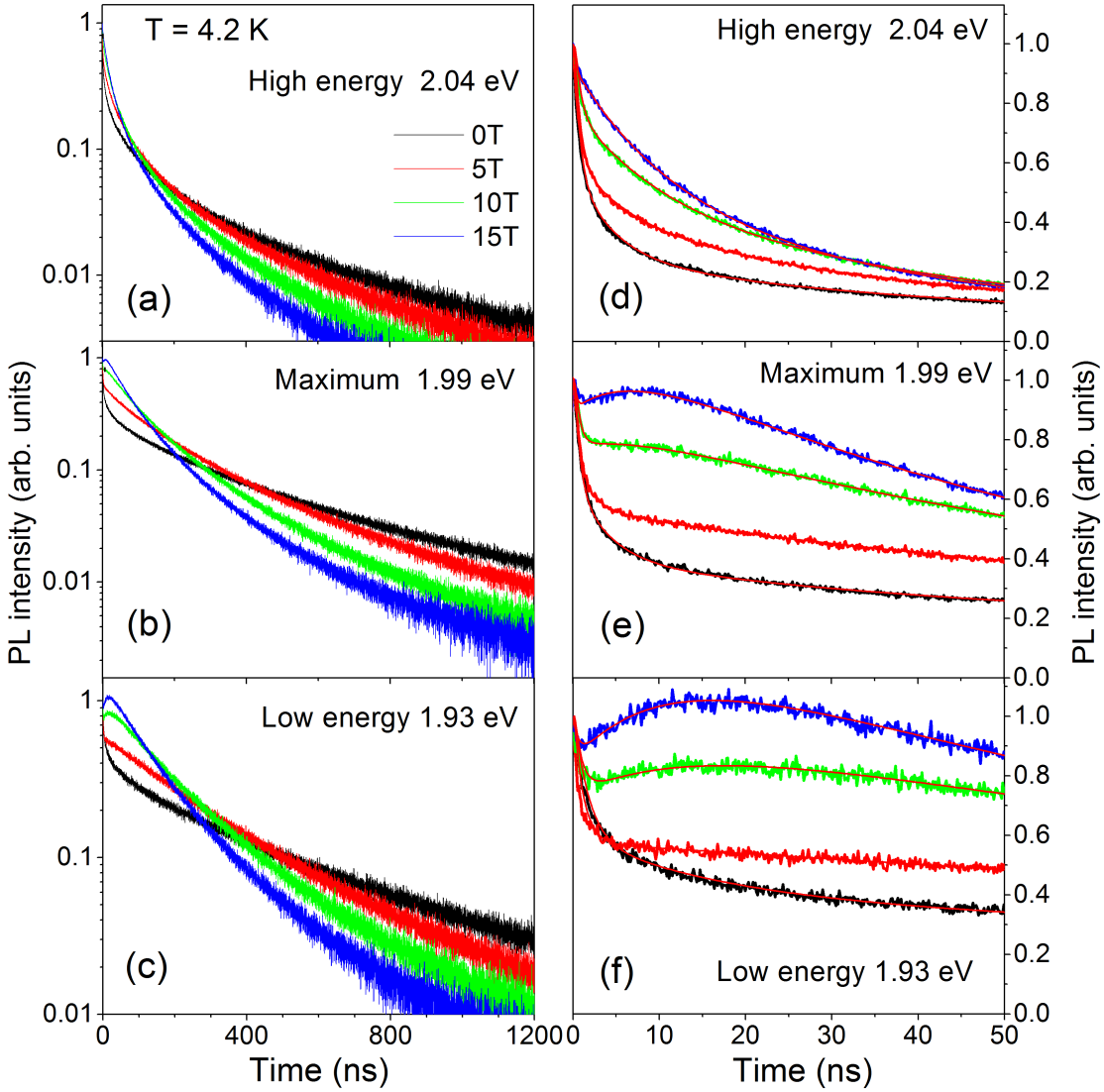

Figure 5-10: PL dynamics of 3.4 nm CdTe NCs measured at different spectral energies (see Fig. 5-4) and different magnetic fields. Panels (d-f) detail the PL dynamics during the initial 50 ns. Thin red lines in the right column are fittings according to Eq. 5.5.

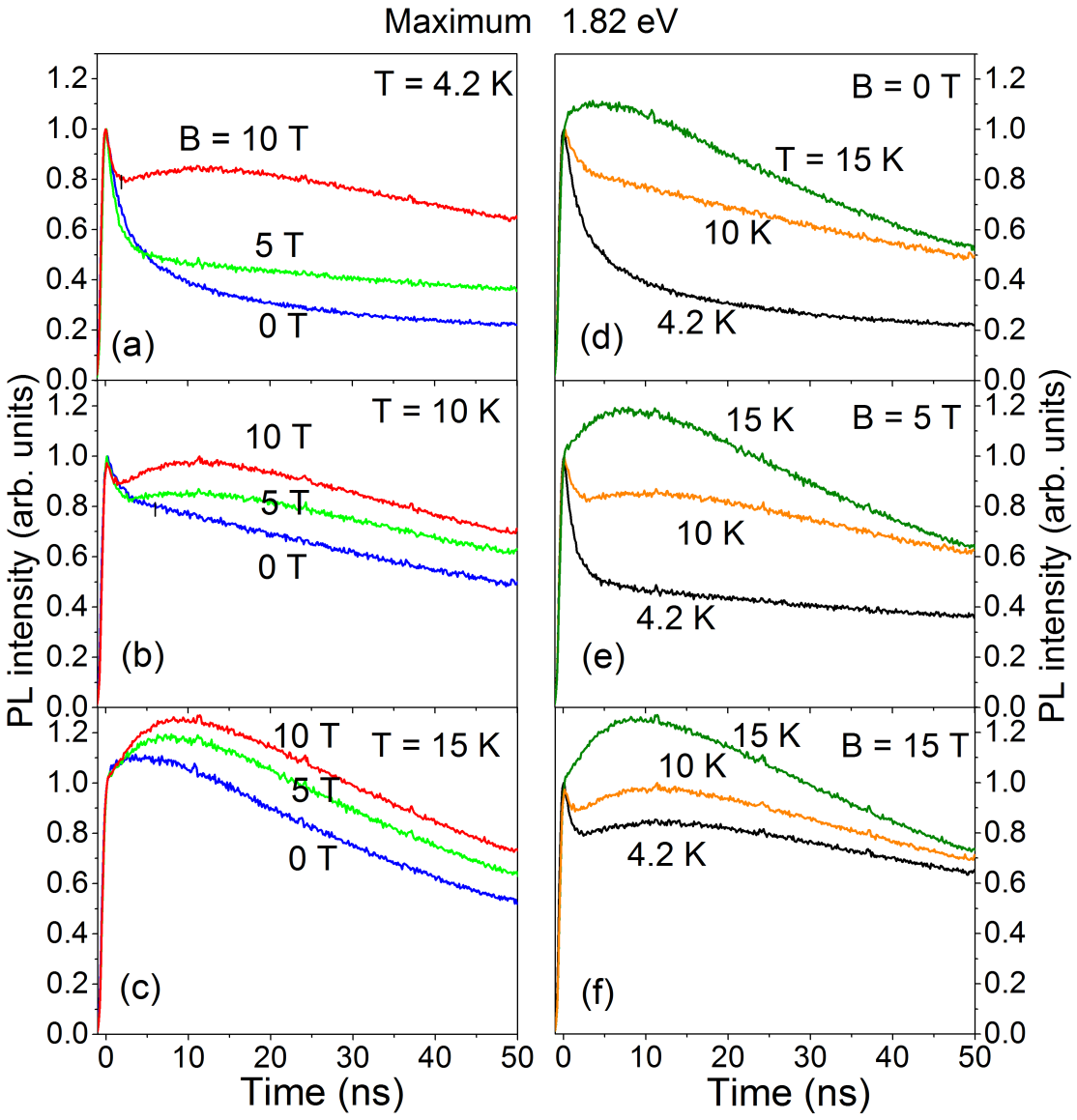

Figure 5-11: PL dynamics of 3.7 nm CdTe NCs measured at the maximum of PL band at 1.82 eV for various magnetic fields and temperatures. In the left column signals for fixed temperatures are compared, while in the right column for fixed magnetic fields.

Figure 5-12 shows the spectral dependence of PL decay time of 3.4 nm CdTe NCs at $B = 0$ T and 15 T at $T = 4.2$ K. The PL decay time is obtained by fitting the spectrally resolved PL decay shown in Fig. 5-9 with a multiexponential function:

$$I_{\mathrm{PL}}(t) = \sum_{i=0}^{5} \frac{A_i g_i}{2} \exp(-g_i t) \left[1 + Erf\left(\frac{t - t_0}{\sqrt{2}\sigma_0} - \frac{g_i \sigma_0}{\sqrt{2}}\right)\right] \tag{5.5}$$

where Erf is the error function. The negative amplitude A_0 corresponds to the first initial fast growth of the intensity and $g_0 = 13$ ns^{-1} was fixed the same for all PL dynamics. The small $g_5 < 0.005$ ns^{-1} was fixed for each decay curve individually to fit the curve tale at the range of $I_{\mathrm{PL}}(t)/I_{\mathrm{PL}}(0) < 0.001$. The moment $t = 0$ was set for each curve to correspond to the PL maximum, $t_0 < 0$ ($|t_0| < 1$ ns) and $I_{\mathrm{PL}}(t_0) = 0$. The four rates $g_i > 0$ and amplitudes A_i (i=1,2,3,4) were varying during the fitting procedure performed with the help of the hand made C^{++} code. The positive amplitudes $A_i > 0$ always correspond to the decaying component while the negative amplitude $A_i < 0$ allow to describe the rising component in magnetic field at the low energy side of the spectrum.

In Fig. 5-12(a) green triangles correspond to the very fast component observed at the very beginning of PL decay. The decay time is related to the relaxation time of excitons from bright states to dark states. Black closed diamonds correspond to the longest component originating from dark excitons. Blue open triangles are most probably related to the Förster energy transfer. Red circles appearing only at high energy side is most likely related to energy transfer from bright-exciton states. It can be seen that at $B = 0$ T all these components show no obvious spectral dependence. Open squares in Fig. 5-12(b) correspond to the rise component induced by the energy transfer. This component is only visible at the low energy side of PL spectra, because only larger NCs with lower emission energy are effectively fed by smaller NCs with higher emission energy. Compared with 0 T, two new components (red stars and orange circles) appears at the high energy side. Considering the similarity of the time scale of these two components with that of the rise component observed at low energy side (open squares), these two new components may be related to new ET paths activated by magnetic field.

Figure 5-13 shows the magnetic field dependence of PL decay time of 3.4 nm CdTe NCs measured at 1.93 eV and $T = 4.2$ K. The shortest component (green triangles) is related to the bright-dark relaxation time. The longest component (black closed diamonds) originating from dark excitons shortens by a factor of ~ 2 for the magnetic field increased from 0 to 15 T. The component represented by blue triangles has the same origin as that in Fig. 5-12(a) which is most probably related to the Föster energy transfer and disappears with the increase of magnetic field. Open squares correspond to the rise of PL intensity induced by the energy transfer.

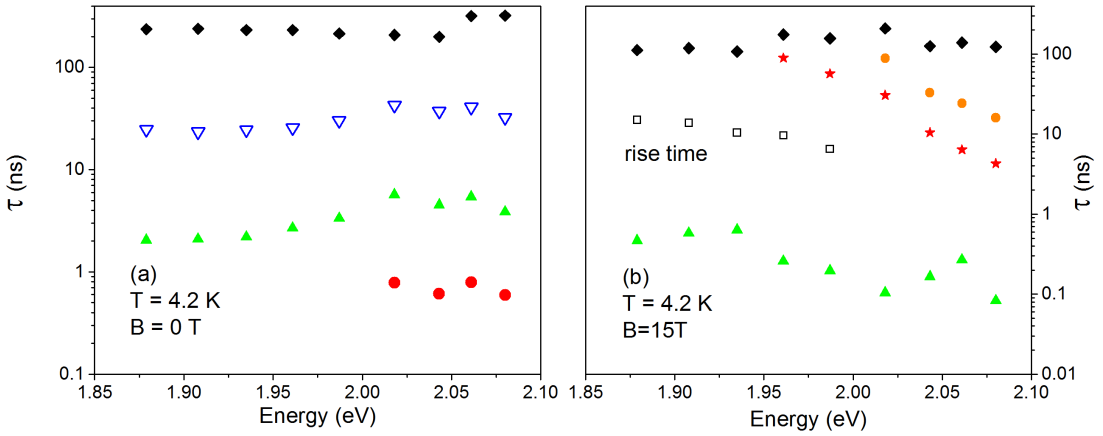

Figure 5-12: Spectral dependence of PL decay time of 3.4 nm CdTe NCs at (a) $B = 0$ T and (b) 15 T at $T = 4.2$ K. Open squares in (b) show the rise time of the unusual rising component (e.g. see the blue line in Fig. 5-10(f)). The PL decay time is obtained by fitting the spectrally resolved PL decay shown in Fig. 5-9 with a multiexponential function (see Eq. (5.5)). The rising component has the negative amplitude $A < 0$.

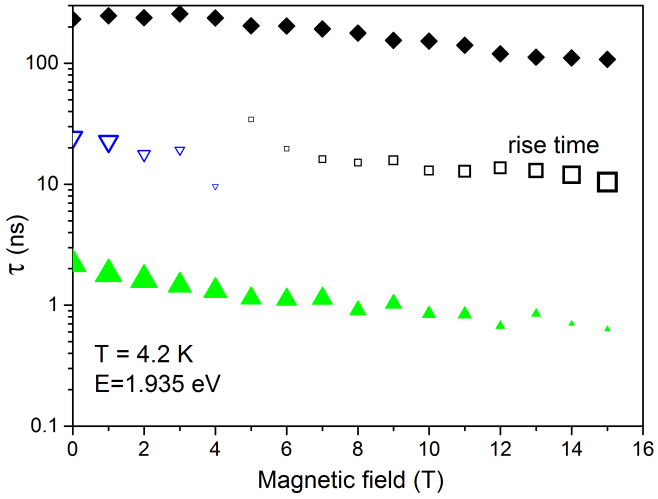

Figure 5-13: Magnetic field dependence of PL decay and rise times of 3.4 nm-diameter CdTe NCs measured at 1.935 eV and $T = 4.2$ K. The PL decay is fitting with a multi-exponential function (see Eq. (5.5)). The rising component has the negative amplitude $A < 0$. The size of symbols, except black diamonds, is proportional to the amplitude $|A|$ of corresponding components.

5.3.2 Simulation of the energy transfer in an ensemble of NCs

Let us assume that PL spectrum from our NCs ensemble just after photoexcitation (in our approximation at $t = 0$) reflects the size distribution of the dots on the ensemble. It has the maximum energy E_0 and can be described by the Gaussian function

$$I_{\mathrm{PL}}(E, E_0) = \frac{1}{\sigma\sqrt{2\pi}} \exp\left[-\frac{(E - E_0)^2}{2\sigma^2}\right] \tag{5.6}$$

where σ corresponds to the line width as FWHM $= 2\sigma\sqrt{2\ln 2}$. The initial maximum position E_0 is nearly independent on the sample area. After the initial excitation two process start simultaneously: the decay of the PL with time and the energy transfer of the excitation from the NCs of the smaller size to the NCs of the larger size. As the result of the energy transfer process the position of the PL spectrum maximum $E_{\mathrm{c}}(t)$ redshifts with time. We assume that the shape of all spectra at each time as well as the shape of the CW spectrum are still described by the same Gaussian function Eq. (5.6) with E_0 replaced by $E_{\mathrm{c}}(t)$ or by the maximum energy of the CW spectrum E_m respectively. From fitting the CW spectrum we obtained the value $\sigma = 50$ eV for our ensemble. During the energy transfer process the particular NCs can play a role of the donor NC for the larger dots and to be acceptors for the smaller dots at the same time. However it is clear that the NCs with energies around E_0 and larger are more effective donors than acceptors while the NCs with energies around E_m and below are more effective acceptors than donors.

The shift of the PL spectrum peak position $E_{\mathrm{c}}(t)$

Our aim now is to describe the shift of the PL maximum $E_{\mathrm{c}}(t)$ observed at different conditions. Let us start from the modeling of the energy shift rate dE_{c}/dt. At the beginning of the process, just after the excitation, the population of the NCs emitting at the giving energy reflects the size distribution. Its maximum is in the energy range of the potential donor NCs and the shift rate is maximal. This rate decreases with time as the effective donor NCs (NCs of the small sizes) become depopulated and saturates when the maximum of the population lays within the range of the large NCs which are effective acceptors. Such situation can be modeled by the following expression:

$$\frac{dE_{\mathrm{c}}(t)}{dt} = -s_0 \exp\left[\frac{E_{\mathrm{c}}(t) - E_0}{E^*}\right] \tag{5.7}$$

where s_0 is the shift rate at $t = 0$ and E^* is the characteristic energy. While $|E_{\mathrm{c}} - E_0| \ll E^*$, the most of the effective donor NCs (small NCs with PL energy

area	condition	E_0 (meV)	E^* (meV)	s_0 (meV/ns)
area 1	4.2 K, 0 T	2.055 ±0.4	11 ±0.3	14 ±1.2
area 1	300 K, 0 T	1.968 ±0.7	17 ±0.4	27 ±2.7
area 2	4.2 K, 0 T	2.035 ±0.4	8 ±0.2	12 ±1.2
area 2	4.2 K, 15 T	2.037 ±0.7	16 ±0.7	6.5 ±0.9

Table 5-1: Fitting parameters for the fitting of time evolution of PL spectra maximum according to Eq. (5.8) shown in Fig. 5-8. Area 1 and 2 corresponds to two different sample positions with different NC concentrations.

around E_0 are still populated and the energy transfer process is effective. When $|E_c - E_0| \approx E^*$ or larger, small NCs become depopulated, the energy transfer is not efficient anymore and the shift rate saturates. $E_c(t)$ can be obtained by solving Eq. (5.7):

$$E_c(t) = E_0 - E^* \ln\left(\frac{s_0 t}{E^*} + 1\right) \tag{5.8}$$

One can see, that the parameter s_0 gives the constant rate of shift at small $t \ll E^*/s_0$, while at $t \gg E^*/s_0$ the rate of shifts drops like E^*/t. The fitting for the peak position of time-resolved spectra according to Eq. (5.8) is shown in Fig. 5-8. The fitting parameters are listed in Table 5-1.

Thus, the suggested model of the PL maximum shift well reproduces the experimental data. Further proof that the energy maximum shift is related to the energy transfer process and not to just the spectral dependence of the exciton recombination rate will be given in the next section by the phenomenological simulation of the PL decay dynamics.

Phenomenological simulation of the PL decay dynamics

The PL decay of CdTe colloidal NCs at specific energy positions can be modeled by combining the decay of PL intensity and the spectral diffusion according to the following equation:

$$I(E,t) = I_{PL}(E, E_c(t)) I_{int}(t) \tag{5.9}$$

where $I(E,t)$ is the PL intensity of time-resolved PL spectra at specific energy and time, $I_{PL}(E, E_c(t))$ is the PL spectrum of Eq. (5.6) with the time-dependent maximum $E_c(t)$ described by Eq. (5.8), and $I_{int}(t)$ is the decay of the PL intensity integrated over the whole spectrum (shown in Fig. 5-5 for $T = 4.2$ K and $B = 0$ T and $B = 15$ T and $T = 4.2$ K and $B = 0$ T).

Figure 5-14 shows the simulated PL decay at low PL energy of 3.4 nm CdTe NCs in different conditions according to Eq. (5.9). In this simulation, all parameters are obtained from the experimental data. $\sigma = 50$ meV is obtained by fitting

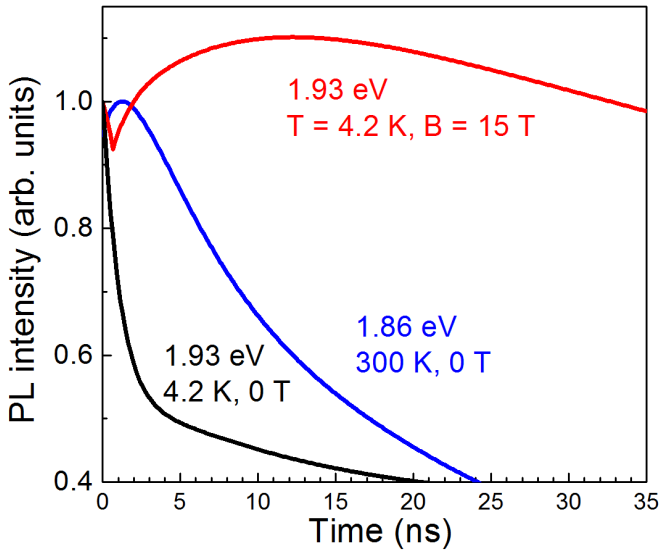

Figure 5-14: Phenomenological simulation of the PL dynamics at the low energy side of the PL band of 3.4 nm CdTe NCs at different temperatures and magnetic fields. At low temperature, 1.93 meV is at the low energy side, but at room temperature, and the spectra shift to lower energy, 1.93 meV is no longer at the low energy side. Therefore the PL decay at 1.86 eV was chosen for the simulation at 300 K.

the time-resolved spectra at $t = 0$ ns with a Gaussian function. The shift of the peak position $E_c(t)$ is obtained by fitting the time evolution of peak positions of time-resolved PL spectra with Eq. (5.8) (see Fig. 5-8). Fitting parameters are listed in Table 5-1. I_{int} was obtained by fitting the integral PL decay in the first 200 ns (see Fig. 5-5) with three exponential functions. The simulated PL decay reproduces all main features of the measured PL decay. At $T = 4.2$ K and $B = 0$ T, the simulated PL decay decays shows a fast decay component and then a longer decay component. By applying magnetic field, a rise of the PL intensity appears. At room temperature, the very fast component visible at 4.2 K disappear and the PL decay starts with a very slow rise of PL intensity.

The main aim of this modeling is to show that the shift if the maximum PL position is indeed caused by the energy transfer as it allows to reproduce the rise of the PL intensity at the low energy side in magnetic field. The absence of such rise in the decay PL integrated over the spectrum proves that the energy transfer is non-radiative and leads to the decrease of the exciton life time at the high energy side. This was also detected by the fitting of the PL dynamics. In contrast, the radiative energy transfer (emission from the donor NC and reabsorption by the acceptor NC) would not affect the decay of the donor NCs and would lead to the increase of the spectrum integrated intensity as well as to the rising of the PL integrated intensity in the magnetic field similar to the one observed at the low energy side of the spectrum.

Theoretical simulation of PL decay dynamics

Until now, we only discuss the influence of magnetic field and temperature on the efficiency of the energy transfer observed in the ensemble of CdTe NCs indirectly via analyzing the shift of PL maximum (see Sec. 5.3.1). In this section, we directly evaluate the magnetic field dependence of the energy transfer efficiency according to a model describing the non-radiative energy process in an ensemble of NCs proposed by A. V. Rodina (see Sec. 2.7).

From Eqs. (2.67, 2.68, 2.69), one can see that for PL at energy E_{d} there are simultaneous contribution from the fraction $(1-f)$ of NCs not participating in the energy transfer process (with characteristic recombination rate Γ_{F} of the dark exciton) and those participating in the energy transfer (with accelerated rate $\Gamma_{\mathrm{F}}+\Gamma_{\mathrm{ET}}^{\mathrm{F}}$). This explains the existence of at least two long time components in the PL decay at high energy side of the spectrum (see Fig. 5-12). At lower energy side this accelerated dark component is also observed in low magnetic fields but with considerably smaller amplitude. At the same time, the unusual rise component with negative amplitude observed at the low energy side of the spectrum in larger magnetic fields (see Fig. 5-12(b) and Fig. 5-13) also corresponds to the rate $\Gamma_{\mathrm{F}}+\Gamma_{\mathrm{ET}}^{\mathrm{F}}$. However, to describe the PL dynamics of the NCs at low energy side correctly, one has to take into account that (i) these NCs can also participate in the process as the donors for even larger size dots in the ensemble and (ii) many NCs with energy $E_{\mathrm{d}} > E_{\mathrm{a}} + E_{\mathrm{da}}$ contribute to the energy feeding of the NCs with energy E_{a}. In our simulation we neglect the point (i), but include point (ii) as the next step.

Now we are ready to simulate the PL decay of the acceptor NCs at low energy side of the PL spectrum of the ensemble measured under different conditions. While the effect of the temperature is included in the rate equations directly via the account of the temperature induced relaxation rate γ_{th}, the effect of the magnetic field must be taken into account by using the magnetic field dependence of the recombination and relaxation rates, Γ_{F} and γ_0 respectively, as well as possible magnetic field dependence of the energy transfer rates.

Let us discuss now step by step the determination of the parameters and their magnetic field dependences for the simulations. To do this we compare the life times determined by the fitting of the experimental PL dynamics with the analytical expressions (see Eqs. (2.58, 2.59, 2.63, 2.64)). One can see first, that the recombination rate of the dark exciton exciton Γ_{F} and its magnetic field dependence can be directly associated with the longest decay component obtained by the fitting of the experimental PL dynamics and shown by the black diamonds in Figs. 5-12 and 5-13. One can see, that this rate indeed very little depends on the energy while increases nearly by factor 2 with increase of magnetic field till 15 T. This increase is caused by the fact, that despite of the cubic symmetry of the crystal lattice of the CdTe, the NCs posses the anisotropic axis related to their

B	Γ_A	Γ_F	γ_0	ΔE_{AF}	Γ_{ET}^{A}	Γ_{ET}^{F}	σ	E_{da}	f	q
0 T	0.1	0.004	0.36	2.2	1	0.022	50	50	0.15	0.93
5 T	0.1	0.005	0.78	2.2	1	0.023	50	50	0.15	0.93
10 T	0.1	0.007	1.07	2.2	1	0.069	50	50	0.15	0.93
15 T	0.1	0.009	1.48	2.2	1	0.090	50	50	0.15	0.93

Table 5-2: Parameters used in the simulation in Figs. 5-15 and 5-16. Γ_{ET}^{A} and Γ_{ET}^{F} are energy transfer rates from bright- and dark-exciton states, Γ_A, Γ_F and g_0 are recombination rates from bright and dark excitons and the relaxation rate at $T = 0$K (taken to be the same for all donor and acceptor NCs). All rates are given in ns^{-1}. The units for energy parameters ΔE_{AF} (the bright-dark splitting energy), σ and E_{da} are meV. The minimum energy of donor-acceptor separation E_{da}, the fraction of the donors f participating in the process and the ration of the bright to dark exciton quantum efficiency $q = \eta_a/\eta_F$ are determined from the simulating of the PL decay in magnetic field $B = 15$ T at $E_a = 1.93$, 1.91 and 1.88 eV at first 50 ns shown in Fig. 5-15. All other parameters are determined from the previous fitting of the magnetic field and temperature dependences of the experimental PL decays as described in the text.

non-spherical shape. As the result, the magnetic field having nonzero projection on the anisotropic axis mixes the bright and dark exciton similar to the well known situation in the hexagonal CdSe NCs[25].

Next, the bright exciton recombination rate Γ_A and the value of the bright to dark exciton splitting ΔE_{AF} are obtained from the temperature dependence of the PL decay (not shown here). We assume Γ_A to be independent on magnetic field and determine the relaxation rate γ_0 and its magnetic field dependence from the bright exciton life time $\tau_a(B)$ at $E = 1.93$ eV (green triangles in Fig. 5-13) as $\gamma_0(B) = 1/\tau_a(B) - \Gamma_a$. The energy transfer rate Γ_{ET}^{F} is equal to the difference between the accelerated dark exciton rate $\Gamma_F + \Gamma_{ET}^{F}$ and Γ_F. However, the attempts to estimate the accelerated dark exciton rate from the decay components at the high energy (donor) side of the spectrum are complicated by the fact that there are more than one such component in the high magnetic field and their rate in fact depend on the spectral position (see Fig. 5-12(b)). For this reason, we use the rise rates (open squares in Fig. 5-13 and Fig. 5-12(b)) observed at low energy side of the spectrum in magnetic fields $B \geq 4$ T in order to estimate $\Gamma_F + \Gamma_{ET}^{F}$ averaged over spectral position and to obtain the magnetic field dependence of the Γ_{ET}^{F}. For zero magnetic field we use the difference of dark exciton rates at high energy side for Γ_{ET}^{F}. The determination of the energy transfer rate Γ_{ET}^{A} from the bright exciton is more difficult because of the very short life times of the bright exciton. For the magnetic field $B = 15$ T we estimated Γ_{ET}^{A} from the approximate relation $\Gamma_{ET}^{A} \approx (\Gamma_A/\Gamma_F)\Gamma_{ET}^{F} \approx 1$ ns^{-1} and assume it is constant in all magnetic fields in the following simulations. Thus determined parameters for magnetic fields $B = 0$, 5, 10 and 15 T are summarized in the Table 5-2.

Additional parameters are the minimum donor-acceptor energy separation E_{da}, fraction of donor NCs participation in the energy transfer process f and the ratio of

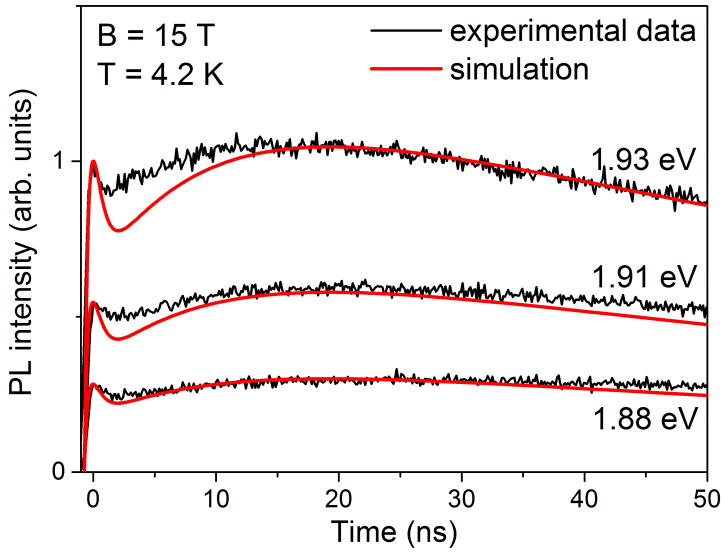

Figure 5-15: Modeling of the PL dynamics at the $E_a = 1.93$, 1.91 and 1.88 eV in 3.4-nm CdTe NCs. Black curves are for the experimental data and red curves are the solutions of the rate equations Eqs. (2.53, 2.55) with the parameters listed in the Table 5-2. The parameters $E_{da} = 50$ meV, $f = 0.15$ and $q = \eta_a/\eta_F = 0.93$ are chosen to give the best simulation of the experimental data while all other parameters are determined from the previous fitting of the magnetic field and temperature dependences of the experimental PL decays as described in the text.

the bright to dark exciton quantum yield $q = \eta_a/\eta_F$ are determined by comparing the simulated PL dynamics with experimental data measured at $T = 4.2$ K in the magnetic field $B = 15$ T of acceptor NCs with the emission energy $E_a = 1.93$, 1.91 and 1.88 eV . The results of such simulation are shown in Figure 5-15 together with the experimental PL dynamics. For these figures the PL intensities are normalized to the maximum PL intensity at $E_a = 1.93$ eV. While the relative rise of PL intensity becomes more pronounced with the decrease of E_a due to the larger value of r_0, the absolute intensity decreases with E_a as N_a decrease. The additional parameters of the model, f, E_{da} and q were varied and chosen to give the better simulation for all three experimental curves in $B = 15$ T simultaneously. The description of the data is the best for the lowest energy. Thus determined value of $f = 0.15$ is in a good agreement with the ratio of the amplitudes of two long decay components at high energy side of the spectrum.

Figure 5-16 shows the simulated PL decay at the energy $E_a = 1.93$ eV at $T = 4.2$ K in the magnetic fields $B = 0$, 5, 10 and 15 T and at $T = 300$ K and $B = 0$ T. Similarly to the simulation based on the phenomenological model, all main features appearing in the measured PL decay are well reproduced by solving the rate equations directly. Parameters used in the simulation are listed in Table 5-2.

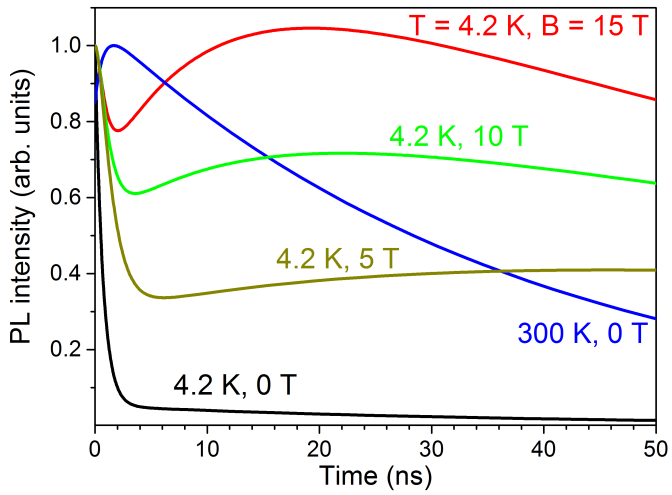

Figure 5-16: Simulation of the PL dynamics of acceptor NCs at $E_a = 1.93$ eV at $T = 4.2$ K and magnetic fields $B = 0$ T (black curve), 5 T (olive curve), 10 T (green curve) and 15 T (red curve) and $T = 300$ K, $B = 0$ T (blue curve). The bright and dark exciton parameters used for the calculations are given in the Table 5-2. The parameters $E_{da} = 50$ meV, $f = 0.15$ and $q = 0.93$ are the same as received from the fitting of the experimental data in Fig. 5-15.

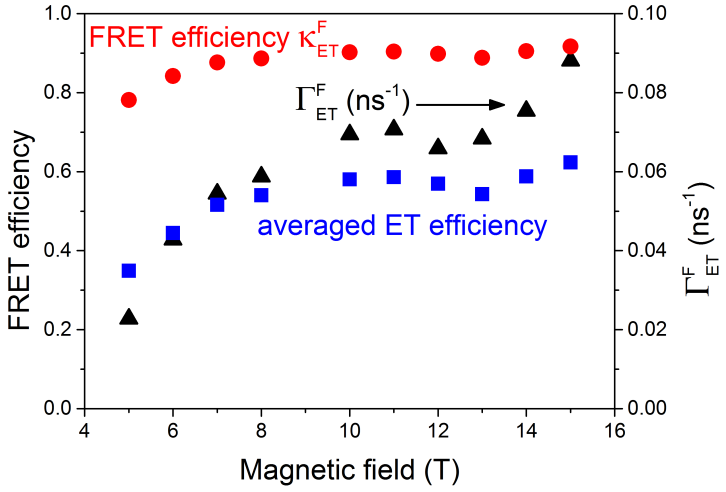

Figure 5-17: Magnetic field dependence of the energy transfer rate of dark-exciton state Γ^F_{ET}, the energy transfer efficiency of the individual NCs $\kappa^F_{ET} = \Gamma^F_{ET}/(\Gamma^F_{ET} + \Gamma_F)$ and the averaged energy transfer efficiency of the ensemble NCs $\langle \kappa^F_{ET} \rangle = \Gamma^F_{ET} f/(\Gamma^F_{ET} f + \Gamma_F)$.

5.3.3 Influence of magnetic field and temperature

The Förster energy transfer is realized via dipole-dipole interaction. Therefore, the efficiency of the Förster energy transfer is dependent on the oscillator strength of dipoles. In colloidal NCs, magnetic field can mix bright- and dark-exciton states, which increases the oscillator strength of dark excitons. So, theoretically, the Förster energy transfer from dark-exciton state in colloidal NCs should be able to be enhanced by magnetic field. The energy transfer from the bright state is less important because of the very short life time of the bright exciton.

Indeed, the enhancement of the energy transfer by magnetic field can be seen already from Fig. 5-8(b). Firstly, the shift of peak position in the first 70 ns at 15 T (51 meV) is larger than that at 0 T (40 meV). Secondly, E^* which characterizes the speed of the shift at 15 T (16 meV) is larger than that at 0 T (8 meV). Since the shift of peak position is related to the energy transfer, we can conclude that energy transfer is enhanced by magnetic field. Moreover, one can see that the time scale on which the PL maximum shift and thus the energy transfer takes place is of the order of 50 ns and thus much longer than the life time of the bright exciton. This fact again indicates the importance of the energy transfer from the dark-exciton state.

The importance of the energy transfer from the dark-exciton state and its acceleration in magnetic field was further directly demonstrated by the modeling of the donor-acceptor rate equations and simulating the PL dynamics at low energy side of the spectrum. It was shown that the unusual rise component in magnetic field can be explained by the energy transfer from the dark-exciton state. The magnetic field dependence of $\Gamma_{\mathrm{ET}}^{\mathrm{F}}$ is shown in Fig. 5-17. One can see, that $\Gamma_{\mathrm{ET}}^{\mathrm{F}}$ increases more than by factor 4 while the dark exciton recombination rate Γ_{F} shown in Fig. 5-13 only increases by a factor of 2. This is because Γ_{F} includes also the non-radiative recombination rate and we may conclude that η_{F} is less than 0.5. The energy transfer efficiency for the NCs participating in the process can be defined as $\kappa_{\mathrm{ET}}^{\mathrm{F}} = \Gamma_{\mathrm{ET}}^{\mathrm{F}}/(\Gamma_{\mathrm{ET}}^{\mathrm{F}}+\Gamma_{\mathrm{F}})$ (see red circles in Fig. 5-17). It seems to be large already in low magnetic fields. However, one has to take into account that only small fraction of all potential donors ($f = 0.15$) participate in the process. The averaged energy transfer efficiency of the ensemble NCs $\langle\kappa_{\mathrm{ET}}^{\mathrm{F}}\rangle = \Gamma_{\mathrm{ET}}^{\mathrm{F}} f/(\Gamma_{\mathrm{ET}}^{\mathrm{F}} f+\Gamma_{\mathrm{F}})$ is also shown in Fig. 5-17. It increases by a factor of 2 in magnetic fields raising from 5 to 15 T.

The effect of the temperature on the energy transfer is due to the thermal mixing of the bright- and dark-exciton states and population of the bright-exciton state. As a result, the long rise of the thermalized bright- and dark-exciton states caused by the energy transfer is observed at room temperature at low energy side of the spectrum as well as the increase of the characteristic energy E^* describing the PL maximum shift at 300 K.

5.4 Summary

In summary, in this chapter we studied the spin dynamics of excitons between two Zeeman-split levels in cubic CdTe colloidal NCs in magnetic field. Similarly to thin-shell CdSe/CdS NCs, a fast spin relaxation time (< 3 ns) was observed in CdTe NCs, which suggests that CdTe NCs and thin-shell CdSe/CdS NCs have similar spin relaxation mechanism. Additionally, a low saturation level of the DCP (-0.3 at 15 T) was observed, which indicates that the sample is a mixture of prolate NCs and oblate NCs. Finally we found and investigated the Förster energy transfer in an ensemble of CdTe NCs. By fitting the magnetic field dependence of spectrally resolved PL dynamics of CdTe NCs according to a model proposed by A. V. Rodina (see Sec. 2.7), it was found that the energy transfer efficiency can be enhanced by a factor of 2 in magnetic fields increasing from $B = 5$ to 15 T at $T = 4.2$ K.

Chapter 6

Recombination and spin dynamics of CdSe-based platelets

In the previous chapter we have shown that the magneto-optical properties of colloidal nanocrystals (NCs) strongly depend on the orientation of magnetic field. This randomization of the orientation of the nanoparticles deposited on the substrate is a strong limitation in applications such as spintronics or quantum optics.

Indeed in experiments performed on ensemble of NCs, the random orientation between magnetic field and the NC quantization axis has to be taken into account. This ensemble averaging has considerably limited studies of optical properties of colloidal NCs under magnetic fields. Up to now, in order to get quantitative values of the Zeeman splitting and the exciton g-factor it has been mandatory to perform experiment at the single dot level. However, in these experiments, the correlation between the orientation and the optical properties remains a delicate task and is time-consuming.

In this chapter we will present the first optical and magneto-optical studies performed on two different kinds of colloidal nanostructures. These two nano-objects represent different approaches in the control of the orientation of the colloidal nanostructures. The first concerns the growth, on a wurtzite spherical CdSe core, of a strongly anisotropic CdS shell. This method allows inducing an anisotropic strain on the core that orients the hexagonal axis perpendicular to the plate. Besides their remarkable orientation properties, these nanostructures have a single-nanocrystal-like behavior allowing a quantitative analysis of the ensemble measurement. These objects will be referred in the following as dot-in-plates (DIPs). In a second part we present results obtained on chemically synthesized quasi-two-dimensional CdSe colloidal nanostructure. These recently-discovered colloidal nanostructures on which the thickness can be controlled at the atomic layer scale, further referred as nanoplatelets (NPLs), are of great interest regarding their optical properties in several fields of applications.

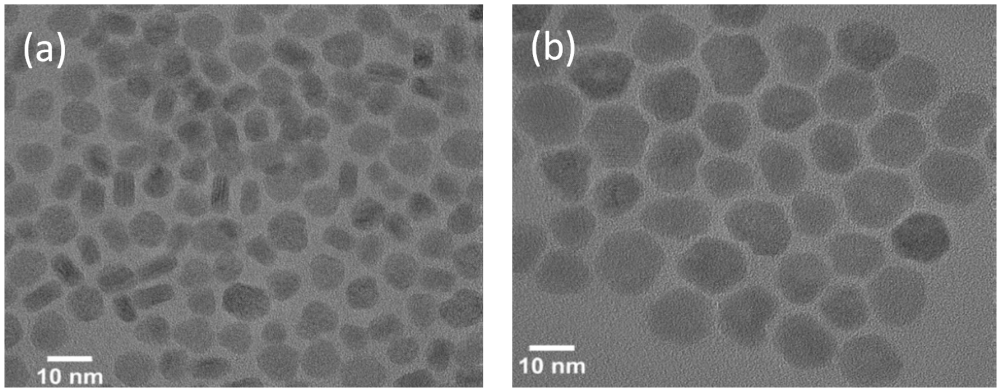

Figure 6-1: Transmission electron microscopy (TEM) images of CdSe/CdS dot-in-plate NCs with (a) 4 monolayers and (b) 8 monolayers of CdS.

6.1 CdSe/CdS dot-in-plate nanocrystals

The CdSe/CdS nanocrystals used in this experiment consist of a wurzite CdSe core of 3.2 nm in diameter surrounded by a CdS shell grown layer by layer with a Successive Ion Layer Adsorption and Reaction method (SILAR). The details of the growth are given in the Ref. 53.

Transmission Electron Microscopy (TEM) images reveal the shape of the nanocrystals. In Fig. 6-1(a), we clearly see a lack of ordering, i.e. DIPs with 4 monolayers (MLs) of CdS lay randomly on the substrate while the sample with 8 MLs (Fig. 6-1(b)) shows uniformity in orientation. Besides interesting orientation effect, the anisotropic growth of the shell provides also new optical properties[53]. Indeed, compared to quasi-spherical NCs, the anisotropic strain on the core in DIPs results in an additional splitting between the light hole (lh) and the heavy hole (hh) valence band as shown in the photoluminescence excitation spectra (see Fig. 6-2).

Although DIP nanocrystals have been intensively studied regarding their structural properties[53,97], almost nothing has been done to investigate their emission properties yet, especially at cryogenic temperature. In this section we present the results of the first study of the magneto-optical properties of DIP samples at low temperature and under magnetic field up to 15 T.

6.1.1 Fine structure of excitons

A comprehensive knowledge of the fine structure of excitons is required in many applications such as spintronics or in quantum optics. The fine structure in colloidal nanostructures is puzzling due to numerous effects that can influence the ordering of the level and energy splittings. In previous studies it has been shown that the temperature dependence and magnetic field dependence of the PL spectra and the PL decay allow determining relevant parameters of the fine structure.

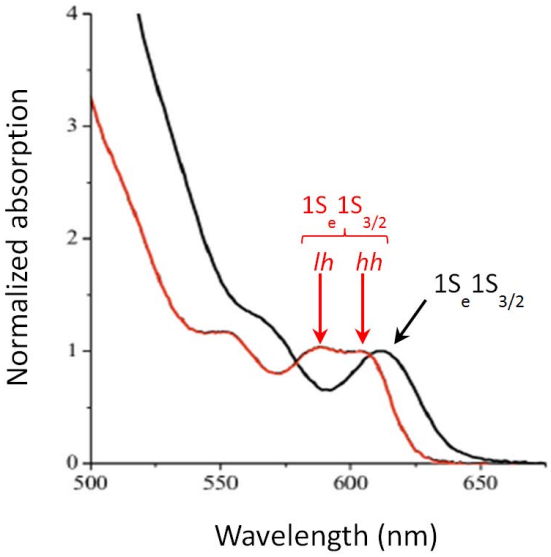

Figure 6-2: Room temperature photoluminescence excitation spectra of CdSe/CdS nanocrystals having 4 monolayers of CdS with spherical shape (black line) and dot-in-plate shape (red line). Adapted from Ref. 97.

Figure 6-3(a) shows the temperature dependence of the spectrally integrated PL decay of an ensemble of DIPs with 4 MLs of CdS. The laser excitation is kept low enough to prevent the creation of multiexcitons. At $T = 4.2$ K, the PL decay is biexponential with a short component around 1 nanosecond and a long component of several hundred of nanoseconds. With the temperature increase, the long component shortens and the weight of short component decreases until its complete vanishing at $T = 30$ K (Fig. 6-3(b)). This well-known behavior is a clear signature of a three level system in which a thermal mixing between a bright state and a dark state occurs with the increase of temperature (see Sec. 2.3).

It should be noticed that the PL decay of an ensemble of DIPs exhibits a single-dot-like behavior since the PL decay can be well fitted with two exponential functions. This property points to a narrow size distribution of DIPs and consequently a small bright-dark energy splittings dispersion. This assumption is supported by the PL spectra. Typically, the size dispersion can be estimated by calculating the ratio $\Delta\lambda/\lambda$. The full width at half maximum (FWHM) of the spectra $\sim$ 15 nm with a wavelength at the maximum position $\sim$ 620 nm gives a size dispersion of about 2% which is more than 2 times smaller than that in regular colloidal NCs[25].

The characteristic energy splitting between the bright and the dark state ΔE_{AF} can be evaluated by fitting the temperature dependence of the long decay rate shown in Fig. 6-4. In addition to ΔE_{AF}, this fitting procedure gives also the decay rate of the bright exciton and the dark exciton. Details of the model are given in Sec. 2.3. The long component of the PL decay Γ_{L} is fitted according to Eq. (2.20). One should note that this expression is valid provided that the spin relaxation

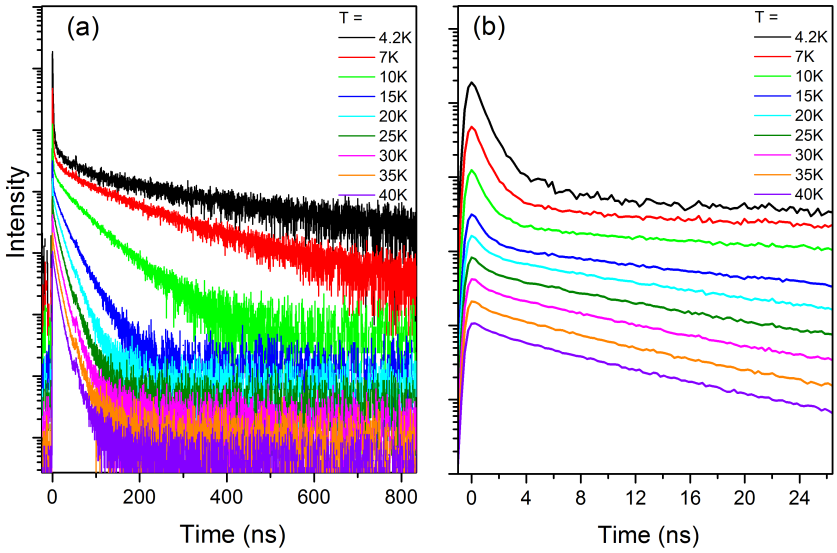

Figure 6-3: (a) Temperature dependence of the PL decay of 4 ML CdSe/CdS dot-in-plate NCs. (b) Same as (a) but for short time scale. PL decays are plotted with an offset for clarity. Laser wavelength: 405 nm. Excitation intensity $<$1mW/cm^2. Repetition rate: 500 kHz.

between the bright and dark states is much larger than other relaxation rates. Additionally the nonresonant excitation leads to an equivalent population of the bright and dark states right after the laser pulse.

The temperature behavior of the long component is well reproduced with the following parameters: $\Gamma_{\mathrm{A}}^{-1} = 3$ ns, $\Gamma_{\mathrm{F}}^{-1} = 1$ μs and $\Delta E_{\mathrm{AF}} = 2.5$ meV. The dark exciton lifetime of 1 μs is typical for quasi-spherical CdSe NCs while a bright exciton lifetime of 3 ns is about 3 times faster than that in quasi-spherical NCs ($\sim$ 10 ns)[20,27]. The energy splitting between the bright and the dark state ($\Delta E_{\mathrm{AF}} = 2.5$ meV) in DIPs is smaller than that in CdSe NCs with the same diameter ($\Delta E_{\mathrm{AF}} = 10$ meV)[20]. This strong decrease of the bright-dark splitting energy is due to the decrease of the electron-hole exchange interaction resulting from the reduction of the electron-hole wave function overlap induced by the electron delocalization in the CdS shell.

6.1.2 Magneto-optical properties of dot-in-plate NC

The DIP samples are of great interest not only regarding the possibility to control their orientation to magnetic field but also to have a better insight of the behavior of the bright- and dark-exciton states. Indeed as we can see in the Fig. 6-2, the light hole band is 70 meV above the heavy hole one, which allows studying the magneto-optical properties in the framework of the three-level system only.

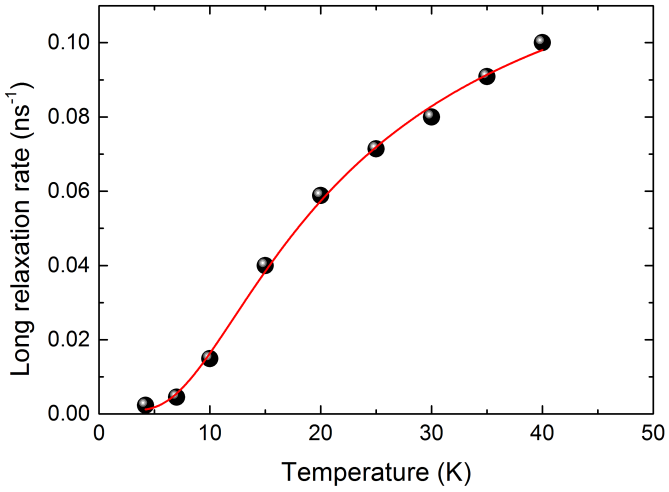

Figure 6-4: Temperature dependence of the long component of the PL decay of CdSe/CdS dot-in-plate sample with 4 MLs of CdS (black dots) fitted (red line) according to the Eq. (2.20) with: $\Gamma_A = 0.33$ ns^{-1}, $\Gamma_F = 0.001$ ns^{-1} and $\Delta E_{AF} = 2.5$ meV.

Fluorescence-line-narrowing experiment under magnetic field: Zeeman splitting

Fig. 6-5 shows the fluorescence-line-narrowing (FLN) spectra of DIPs. In order to cut the laser line from the PL, we have cross-polarized the excitation and the detection. The excitation path is σ^+ polarized while the detection path is σ^- polarized. The FLN spectra is composed of a Zero Phonon Line (ZPL) redshifted by 2 meV from the laser line. This value is in good agreement with the bright-dark energy splitting previously estimated. The FLN spectra also shows Longitudinal Optical (LO) phonon replica redshifted from the ZPL. The strongest line in the LO phonon replica is redshifted by 28 meV and the weakest by 37 meV in good agreement with the shift energy of the bulk LO phonons in CdSe (26 meV) and CdS (37 meV), therefore these peaks can be attributed to the LO phonon replica of CdSe and CdS. The presence of the latter on the FLN spectra also implies that the electron "feels" the CdS plate, confirming the delocalization of the electron over the entire DIP structure.

The accuracy of determining the Zeeman splitting of an ensemble of colloidal NCs by polarization-resolved PL measurement is limited by the size dispersion of the sample. This problem can be easily overcome by FLN measurement which, as shown in Chap. 4, allows reducing by approximately one order of magnitude the homogeneous line width of the PL spectra. The FLN spectra clearly shows a redshift with magnetic field as exemplified in Fig. 6-5. For clarity, the spectra have been normalized to the maximum of the ZPL.

From the splitting between the ZPL we can give a lower bound for the exciton g-factor by assuming a perfect orientation of the DIP (no angle between the c-axis and magnetic field). We find $|g_{exc}| \sim 3$ in good agreements with the dark exciton

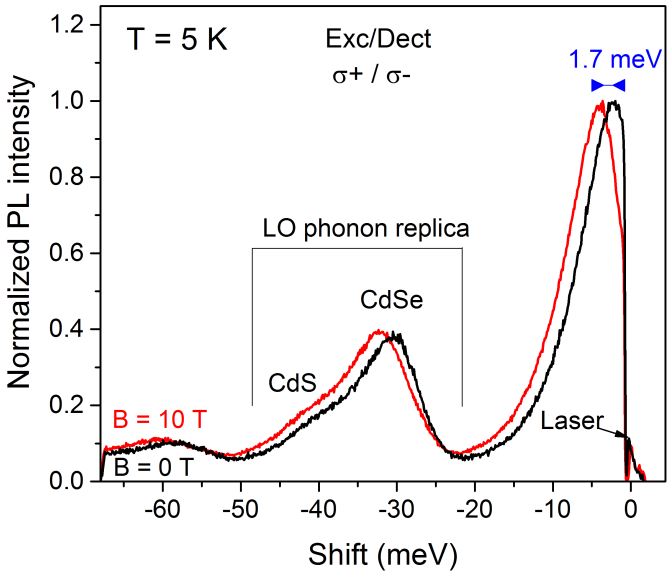

Figure 6-5: FLN spectra of CdSe/CdS dot-in-plate NCs at magnetic field of 0 T and 10 T. The excitation laser is σ^+ polarized and the PL is σ^- polarized.

g-factor determined in a previous study performed on single CdSe/CdZnS NC[28].

Circular polarization degree and spin dynamics

Besides the Zeeman splitting and the exciton g-factor, we have studied the spin dynamic as well as the circular polarization degree of DIPs. For this purpose, we have performed magnetic field dependence of the polarization-resolved PL decay. Figure 6-6 shows the PL decay at 0 T and 15 T for σ^+ and σ^- polarization. From the figure it is clear that magnetic field plays an important role in exciton recombination dynamics.

Indeed when raising magnetic field, the long component of the PL decay becomes shorter. Thus, the long decay shortens from $\sim$ 450 ns at 0 T to 90 ns at 15 T. In agreement with previous experiments on quasi-spherical NCs[20,25,28], this shortening is expected in the case of a coupling between the bright and dark states induced by the transverse component of magnetic field. Additionally this shortening indicates a random orientation of the nanoparticles. The analysis of the polarized PL decays shows that the PL is highly circularly polarized at 15 T.

From the polarization-resolved PL decays, the time-resolved degree of circular polarization at different magnetic fields can be evaluated according to Eq. (2.24) and shown in Fig. 6-7. From the figure we see a shortening of the rise time when increasing magnetic field. Unfortunately the rise time is too close to the resolution of the experimental setup (800 ps) and cannot be reliably quantitatively evaluated. However the behavior of the rise time is qualitatively similar to the behavior of the time-resolved DCP of CdSe/CdS NCs (see Chap. 4) and can be attributed to the spin relaxation due to field induced mixing between valence bands. Nevertheless

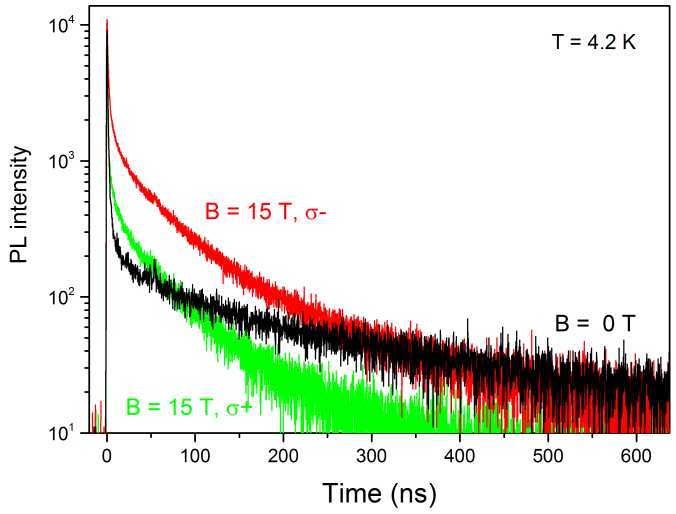

Figure 6-6: Polarization-resolved PL decay of dot-in-plates NCs at 4.2 K at different magnetic fields.

striking behavior occurs on longer time scale at high magnetic field. Indeed as shown in Fig. 6-8, we clearly see a initial rise of the DCP in few hundreds of picoseconds and a second rise time of several hundreds of nanoseconds.

Such a slow rise rate at high magnetic field implies the presence of higher order process in spin relaxation. This slow relaxation process can only occur between Zeeman spin states, thus from nanocrystals whose c-axis is orientated along magnetic field. As exemplified in the inset of Fig. 6-8, several acoustic phonons are required to relax from the upper to the lower spin state. This phenomenon, not observed in "standard" quasi-spherical NCs, indicates that a significant proportion of dot-in-plate NCs have a preferential orientation when deposited on the substrate. This assumption is further confirmed by previous single dot experiment where spin relaxation time between Zeeman sub-levels of the dark exciton of several hundred of nanoseconds have been measured[28].

6.2 Quasi-2D colloidal CdSe nanoplatelets

Colloidal nanoplatelet is a new type of quasi two-dimensional colloidal nanostructure which have been synthesized very recently. The colloidal nanoplatelets studied in this thesis have been grown following the protocols of Ref. 58. This synthesis, made from organometallic precursors of Cd and Se, allows growing colloidal quantum wells with a control on the thickness at the atomic layer scale and lateral dimensions of the order of hundreds of nanometers. Fig. 6-9(a) and (b) show TEM images of nanoplatelets having different thickness (1.9 nm and 2.2 nm respectively).

It is worth to note that within the ensemble, the NPL have exactly the same

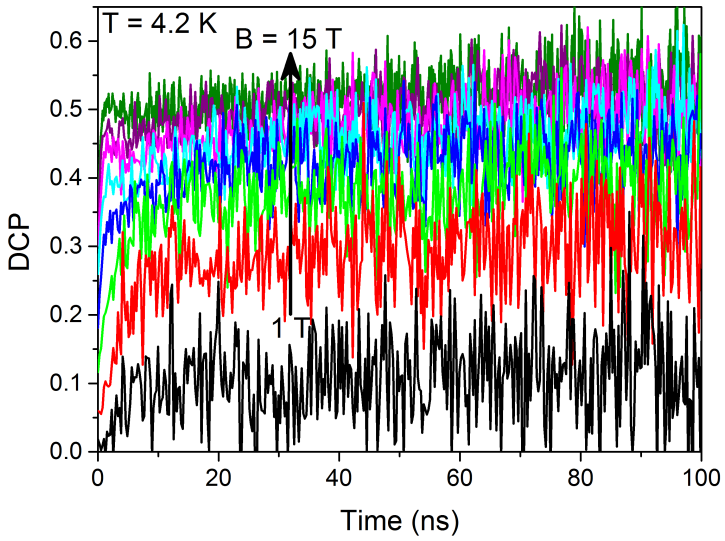

Figure 6-7: Time-resolved circular polarization degree of CdSe/CdS dot-in-plate NCs at different magnetic fields.

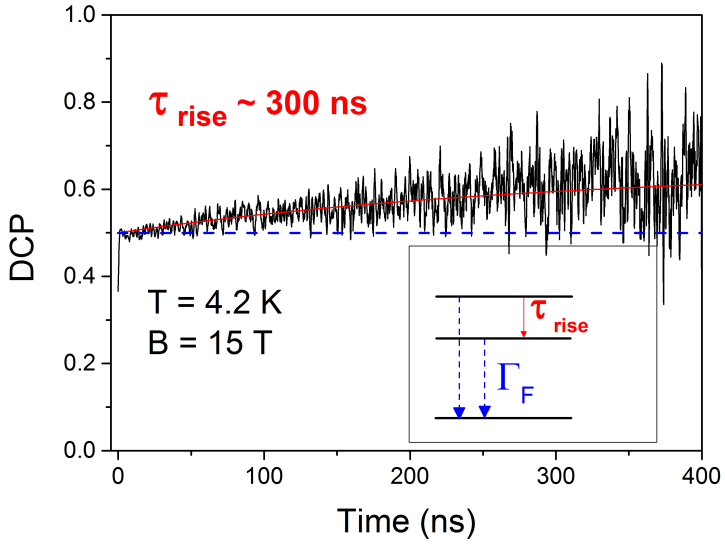

Figure 6-8: Time-resolved DCP of CdSe/CdS dot-in-plate NCs fitted by a single exponential function (red curve).The dashed line represents the DCP after the rapid rise time. Inset: Scheme of the relaxation process of the dark exciton in magnetic field. The spin relaxation process from the upper to lower spin state implies several acoustic phonons.

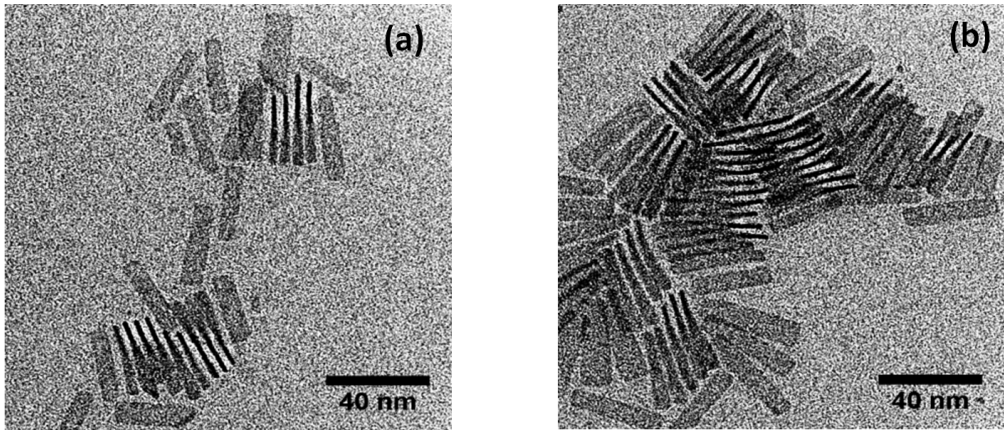

Figure 6-9: TEM images of colloidal NPLs with thickness of (a) 1.9 nm and (b) 2.2 nm.

thickness. This is evidenced by the narrow PL spectra (FWHM $\sim$ 30 to 40 meV) at room temperature which is of the order of $k_{\mathrm{B}}T$ for all the synthesized samples (see Fig. 6-10). Besides these observations, the PL spectra do not evidence other features indicating a high purity of the sample.

Figure 6-11 shows the temperature dependence of the PL spectra of the 2.2 nm thick NPL sample. When the temperature is decreased, an additional peak, denoted as X^{LO}, appears and redshifts by 27 meV from the excitonic peak, X^{0}. The origin of this peak has been studied by Tessier et al. and has been attributed to enhancement of the LO phonon replica induced by the re-absorption of the emission from the Zero Phonon Line[98].

To understand the origin of the ZPL of NPLs at cryogenic temperature, we have performed temperature and magnetic field dependence studies of the PL decay of NPLs. In Fig. 6-12(a), we report the temperature dependence of the PL decay of the 2.2 nm thick NPL sample. We clearly see that at 5 K the PL decay is biexponential with a short component of few tens of picoseconds and a long component of several nanoseconds*. When increasing the temperature, the short component vanishes and the long component shortens from 10 ns at 2 K to 200 ps at 50 K. The shortening of the PL decay with the temperature indicates that in this temperature regime, excitons do not behave as a free 2D excitons because, according to theoretical calculations, the PL decay time would lengthen linearly with the temperature[99]. However, the shortening of the long component of the PL decays has already been observed in CdSe-based NCs and has been interpreted in terms of thermal mixing between a bright state and a dark state and this behavior can be well described by a three-level model[27,59,83] (see also Sec. 2.3).

*This behavior differs from the PL decay observed in the Ref. 54 where a single exponential was ob-served. In fact, a careful check of the temperature on the same cryostat indicates that in the latter paper, the temperature was 30 K instead of 5 K in agreement with our current lifetime measurements.

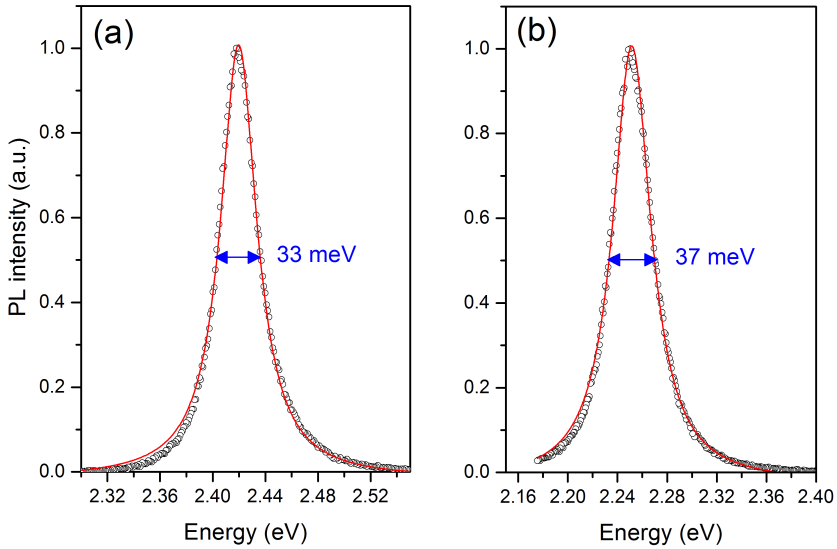

Figure 6-10: PL spectra (open dots) at room temperature of CdSe nanoplatelets with thickness of (a) 1.9 nm and (b) 2.2 nm. Red curves correspond to Lorentzian fit. At room temperature the homogeneous broadening of the PL line shape of an ensemble of nanoplatelets is dominated by the lateral size distribution of nanoplatelets.

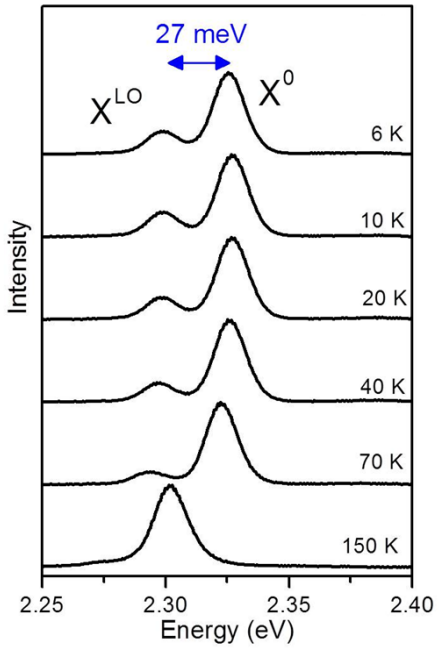

Figure 6-11: Temperature dependence of the PL spectra of the 2.2 nm thick NPL sample. X^{LO} and X^0 correspond to the LO phonon replica and the ZPL respectively.

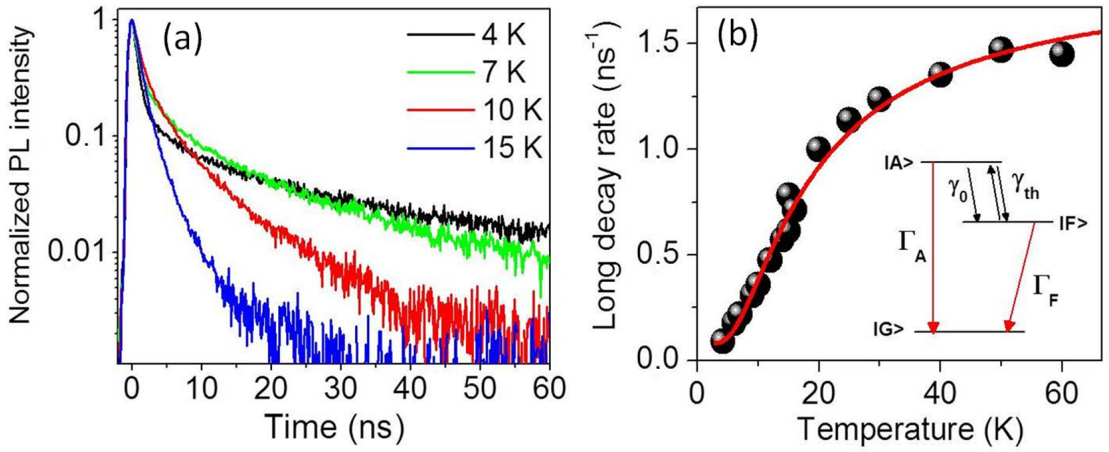

Figure 6-12: (a) Luminescence decay curves of 2.2 nm thick NPLs at various temperatures. The sample was excited at 405 nm with a pulsed laser (1MHz, 50 ps). (b) Decay rate of the long component of the PL decay as a function of the temperature. Solid line is the fit derived from the three-level model (see text) with: $\Gamma_A = 3.6$ ns^{-1}, $\Gamma_F = 0.05$ ns^{-1} and $\Delta E_{AF} = 2$ meV.

In Fig. 6-12(b) we show the long relaxation rate deduced from the monoexponential fit of the tail of the PL decays. By fitting the the temperature dependence of the long component of PL decay with Eq. (2.20), we obtain $\Gamma_A = 3.6$ ns^{-1}, $\Gamma_F = 0.05$ ns^{-1} and $\Delta E_{AF} = 2$ meV for the 2.2 nm thick NPLs and $\Gamma_A = 12$ ns^{-1}, $\Gamma_F = 0.05$ ns^{-1} and $\Delta E_{AF} = 5$ meV for the 1.9 nm thick NPLs (data not shown). The increase of the bright-dark energy splitting as the thickness of the platelets decreases indicates an enhancement of the exchange interaction as in nanocrystals. Remarkably, the bright dark energy splitting in platelets is much smaller than in dots having a radius comparable to the platelet thickness[100]. Indeed the exchange splitting between the bright and the dark state in nanoplatelets ($\sim$ 2 meV) is in-between those of spherical CdSe with comparable dimension ($\sim$ 20 meV)[100] and the CdSe bulk ($\sim$ 0.13 meV)[101]. Interestingly bright-dark energy splitting in colloidal NPL is one order of magnitude higher than typical one for II-VI epitaxial grown quantum wells (QWs)[102]. This large difference can be attributed to the strong dielectric confinement in free-standing colloidal NPL that enhances the electron-hole exchange interaction.

In order to understand the role played by the dark state in the emission of the nanoplatelets, we have studied the time resolved PL of the platelets under magnetic field at 4.2 K. in Fig. 6-13 we clearly see that, the long component dramatically shortens from $\sim$ 20 ns at 0 T to $\sim$ 4 ns at 15 T as a result of the enhancement of the radiative rate induced by magnetic field coupling[24,28]. One should note that the enhancement is not the result of the Landau levels because at least two dimensions of the NPL are smaller than the magnetic length (typically 11 nm at 10 T).

The magnetic field dependence of the ZPL further evidence the coupling be-

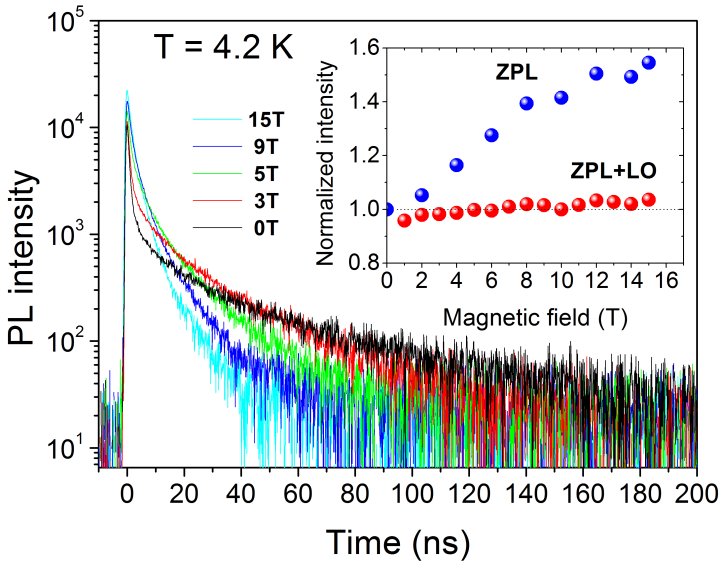

Figure 6-13: Magnetic field dependence of the PL decay of the 2.2 nm thick NPL sample. Inset: evolution with magnetic field of the total intensity of the luminescence (ZPL+LO) (red dots) and of the ZPL (blue dots).

tween the bright and dark states[100]. In inset of Fig. 6-13, we report the total PL intensity (ZPL+LO) of platelets and the ZPL intensity, filtered by a monochromator, with magnetic field. The increase of the ZPL intensity while the total PL intensity (ZPL+LO) remains constant clearly indicates a gain of oscillator strength[24,28]. Therefore the increase of the ZPL line is due to field induced mixing of the bright and dark states that allows the radiative recombination of the dark exciton without assistance of phonon thus reducing the LO phonon line[24,28].

6.3 Summary

In summary, in this chapter we present the results of magneto-optical study of two types of CdSe-based colloidal platelets. By fitting the temperature dependence of PL decay of DIPs according to a three-level model, it is found that the bright-dark splitting energy ΔE_{AF} is much smaller than that in CdSe NCs with the same diameter due to the strong decrease of the electron-hole exchange interaction resulting from the reduction of the electron-hole wave function overlap in DIPs. Surprisingly, the time-resolved degree of circular polarization (DCP) of DIPs shows a rather slow relaxation process ($\tau_{\mathrm{rise}} \sim 300$ ns) which was not observed in quasi-spherical NCs. This extremely slow spin relaxation process is most likely related to higher order process which involves several acoustic phonons.

Through the temperature and magnetic field dependence of the PL decay of NPLs, we prove that the emission of NPLs arises from the thermal mixing between a bright state and a dark state. The energy splitting between the bright and the

dark state is one order of magnitude smaller than in NCs having radius comparable to the NPL thickness. Interestingly the lifetime of the bright and the dark exciton are about two orders of magnitude faster than in NCs suggesting the existence of giant oscillator strength.

Summary

By means of magneto-optical experimental techniques, fundamental properties, such as g-factor, spin dynamics and fine structure of the exciton complex in three types of colloidal nanostructures, including core/shell CdSe/CdS nanocrystals (NCs), Thoil-capped CdTe NCs and CdSe-based colloidal platelets, were characterized at cryogenic temperatures (down to $T = 2.2$ K) and in high magnetic fields (up to $B = 17$ T). Based on these results, mechanisms responsible for different behaviors of exciton spin dynamics observed in thick-shell CdSe/CdS NCs and CdTe NCs were discussed. Additionally, the influence of magnetic field and temperature on the Förster resonant energy transfer in ensembles of CdTe colloidal NCs was investigated and data were analyzed based on a model proposed by A. V. Rodina.

By comparing the recombination dynamics and fluorescence-line-narrowing spectra of thin-shell and thick-shell CdSe/CdS NCs, it was proven that the PL of the new type of thick-shell NCs originates from charged excitons. According to the sign of the PL polarization degree, it was identified that the exciton complex in thick-shell CdSe/CdS NCs is negatively charged. Then, a direct measurement of the spin relaxation rate of negatively charged excitons was performed. The most striking result is that a spin relaxation time of 58 ns at $B = 1$ T is much longer than the previously reported spin relaxation time in CdSe NCs[25,60]. The spin relaxation rate increases quadratically with magnetic field and temperature, which suggests that the spin relaxation of negative trions between hole spin sub-levels is assisted by two confined phonons of the CdS shell. The acceleration of the spin relaxation in magnetic field is due to the mixing of heavy- and light-hole states by the transverse component of magnetic field. A spin relaxation rate of 0.015 ns^{-1} and a g-factor of -0.54 at $T = 4.2$ K were extracted based on a model providing a complete description of the magnetic field and temperature dependences of the spin relaxation time and PL circular polarization degree.

Compared with thick-shell CdSe/CdS colloidal NCs, the spin dynamics of excitons in the CdTe NCs is much faster (< 3 ns), suggesting a one-phonon-assisted spin relaxation mechanism. A low saturation level of the PL circular polarization degree (-0.3 at B =15 T) was observed. This is explained by a mixture of prolate and oblate NCs. Furthermore, we show that by knowing the ratio between the

quantum yield of these two types of NCs, fitting the PL polarization degree provides a simple optical method to evaluate the ratio between the number of these two types of NCs. Finally we explored the Förster energy transfer in ensembles of CdTe NCs. By analyzing the PL dynamics of CdTe NCs according to a model proposed by A. V. Rodina, it was found that the energy transfer efficiency was enhanced by a factor of 2 in magnetic fields increasing from 5 to 15 T at $T = 4.2$ K. This study demonstrates a new way to control the Förster resonant energy transfer efficiency in colloidal NCs.

Finally we characterized two types of CdSe-based colloidal platelets only available very recently. For the CdSe/CdS dot-in-plate structure with four-monolayer shell, a bright-dark splitting energy ΔE_{AF} of 2.5 meV was obtained. This bright-dark splitting energy is much smaller than that in CdSe NCs with the same diameter, which can be explained by the strong decrease of the electron-hole exchange interaction resulting from the reduction of the electron-hole wavefunction overlap in dot-in-plate structures. Moreover, a surprisingly slow relaxation process (~ 300 ns) was observed. This extremely slow spin relaxation process is most likely related to higher order process involving several acoustic phonons. The study on the quasi-two-dimensional colloidal nanoplatelet proves that the PL emission of nanoplatelet arises from the thermal mixing between a bright and dark state. Additionally, it was found that the bright-dark energy splitting was one order of magnitude smaller than that in NCs with a radius comparable to the nanoplatelet thickness.

Bibliography

1. Moore, G. *IEEE Int. Electron Devices Meeting* **21**, 11 (1975).

2. Žutić, I. and Das Sarma, S. *Reviews of Modern Physics* **76**(2), 323–410 (2004).

3. Loss, D. and DiVincenzo, D. *Physical Review A* **57**(1), 120–126 (1998).

4. Pisanello, F., Martiradonna, L., Spinicelli, P., Fiore, A., Hermier, J.-P., Manna, L., Cingolani, R., Giacobino, E., Bramati, A., and De Vittorio, M. In *2009 11th International Conference on Transparent Optical Networks*, 1–4. IEEE, (2009).

5. Colvin, V. L., Schlamp, M. C., and Alivisatos, A. P. *Nature* **370**(6488), 354–357 (1994).

6. García-Santamaría, F., Chen, Y., Vela, J., Schaller, R. D., Hollingsworth, J. A., and Klimov, V. I. *Nano Letters* **9**(10), 3482–8 (2009).

7. Bruchez Jr., M. *Science* **281**(5385), 2013–2016 (1998).

8. Chen, O., Zhao, J., Chauhan, V. P., Cui, J., Wong, C., Harris, D. K., Wei, H., Han, H.-S., Fukumura, D., Jain, R. K., and Bawendi, M. G. *Nature Materials* **12**, 445–451 (2013).

9. Murray, C. B., Norris, D. J., and Bawendi, M. G. *Journal of the American Chemical Society* **115**(19), 8706–8715 (1993).

10. Rogach, A., Franzl, T., Klar, T., Feldmann, J., Gaponik, N., Lesnyak, V., Shavel, A., Eychmuller, A., Rakovich, Y., and Donegan, J. *Journal of Physical Chemistry C* **111**(40), 14628–14637 (2007).

11. Nirmal, M., Dabbousi, B. O., Bawendi, M. G., Macklin, J. J., Trautman, J. K., Harris, T. D., and Brus, L. E. *Nature* **383**(6603), 802–804 (1996).

12. Efros, A. and Rosen, M. *Physical Review Letters* **78**(6), 1110–1113 (1997).

13. Mahler, B., Spinicelli, P., Buil, S., Quelin, X., Hermier, J.-P., and Dubertret, B. *Nature Materials* **7**(8), 659–64 (2008).

14. Chen, Y., Vela, J., Htoon, H., Casson, J. L., Werder, D. J., Bussian, D. A., Klimov, V. I., and Hollingsworth, J. A. *Journal of the American Chemical Society* **130**(15), 5026–7 (2008).

15. Spinicelli, P., Buil, S., Quélin, X., Mahler, B., Dubertret, B., and Hermier, J.-P. *Physical Review Letters* **102**(13), 136801 (2009).

16. Galland, C., Ghosh, Y., Steinbrück, A., Sykora, M., Hollingsworth, J. A., Klimov, V. I., and Htoon, H. *Nature* **479**(7372), 203–7 (2011).

17. Htoon, H., Malko, A. V., Bussian, D., Vela, J., Chen, Y., Hollingsworth, J. A., and Klimov, V. I. *Nano Letters* **10**(7), 2401–7 (2010).

18. Javaux, C., Mahler, B., Dubertret, B., Shabaev, A., Rodina, A., Efros, A., Yakovlev, D., Liu, F., Bayer, M., Camps, G., Biadala, L., Buil, S., Quelin, X., and Hermier, J.-P. *Nature Nanotechnology* **8**(3), 206–12 (2013).

19. Park, Y.-S., Malko, A. V., Vela, J., Chen, Y., Ghosh, Y., García-Santamaría, F., Hollingsworth, J. A., Klimov, V. I., and Htoon, H. *Physical Review Letters* **106**(18), 187401 (2011).

20. Efros, A. L., Rosen, M., Kuno, M., Nirmal, M., Norris, D. J., and Bawendi, M. *Physical Review B* **54**(7), 4843–4856 (1996).

21. Kadantsev, E. and Hawrylak, P. *Physical Review B* **81**(4), 045311 (2010).

22. Korkusinski, M., Voznyy, O., and Hawrylak, P. *Physical Review B* **82**(24), 245304 (2010).

23. Zhao, Q., Graf, P. A., Jones, W. B., Franceschetti, A., Li, J., Wang, L.-W., and Kim, K. *Nano Letters* **7**(11), 3274–80 (2007).

24. Nirmal, M., Norris, D. J., Kuno, M., Bawendi, M. G., Efros, A. L., and Rosen, M. *Physical Review Letters* **75**(20), 3728 (1995).

25. Johnston-Halperin, E., Awschalom, D. D., Crooker, S. A., Efros, A. L., Rosen, M., Peng, X., and Alivisatos, A. P. *Physical Review B* **63**(20), 205309 (2001).

26. Crooker, S. A., Barrick, T., Hollingsworth, J. A., and Klimov, V. I. *Applied Physics Letters* **82**(17), 2793 (2003).

27. Biadala, L., Louyer, Y., Tamarat, P., and Lounis, B. *Physical Review Letters* **103**(3), 037404 (2009).

28. Biadala, L., Louyer, Y., Tamarat, P., and Lounis, B. *Physical Review Letters* **105**(15), 157402 (2010).

29. Willard, D. M., Mutschler, T., Yu, M., Jung, J., and Van Orden, A. *Analytical and Bioanalytical Chemistry* **384**(3), 564–571 (2006).

30. Chanyawadee, S., Harley, R., Henini, M., Talapin, D., and Lagoudakis, P. *Physical Review Letters* **102**(7), 077402 (2009).

31. Chanyawadee, S., Harley, R. T., Taylor, D., Henini, M., Susha, A. S., Rogach, A. L., and Lagoudakis, P. G. *Applied Physics Letters* **94**(23), 233502 (2009).

32. Becker, K., Lupton, J. M., Müller, J., Rogach, A. L., Talapin, D. V., Weller, H., and Feldmann, J. *Nature Materials* **5**(10), 777–81 (2006).

33. Chanyawadee, S., Lagoudakis, P. G., Harley, R. T., Charlton, M. D. B., Talapin, D. V., Huang, H. W., and Lin, C.-H. *Advanced materials (Deerfield Beach, Fla.)* **22**(5), 602–6 (2010).

34. Medintz, I. L., Clapp, A. R., Mattoussi, H., Goldman, E. R., Fisher, B., and Mauro, J. M. *Nature Materials* **2**(9), 630–8 (2003).

35. Förster, T. *Annalen der Physik* **437**(1-2), 55–75 (1948).

36. Rogach, A. L., Klar, T. A., Lupton, J. M., Meijerink, A., and Feldmann, J. *Journal of Materials Chemistry* **19**(9), 1208 (2009).

37. Crooker, S. A., Hollingsworth, J. A., Tretiak, S., and Klimov, V. I. *Physical Review Letters* **89**(18), 186802 (2002).

38. Clark, S., Harbold, J., and Wise, F. *Journal of Physical Chemistry C* **111**(20), 7302–7305 (2007).

39. Schrier, J. and Wang, L.-W. *Journal of Physical Chemistry C* **112**(30), 11158–11161 (2008).

40. Sitt, A., Even-Dar, N., Halivni, S., Faust, A., Yedidya, L., and Banin, U. *The Journal of Physical Chemistry C* , A–L (2013).

41. Kagan, C., Murray, C., and Bawendi, M. *Physical Review B* **54**(12), 8633–8643 (1996).

42. Kagan, C. R., Murray, C. B., Nirmal, M., and Bawendi, M. G. *Physical Review Letters* **76**(9), 1517 (1996).

43. Kim, D., Okahara, S., Nakayama, M., and Shim, Y. *Physical Review B* **78**(15), 153301 (2008).

44. Lunz, M., Bradley, A. L., Chen, W.-Y., and GunÊ$\frac{1}{4}$ko, Y. K. *The Journal of Physical Chemistry C* **113**(8), 3084–3088 (2009).

45. Franzl, T., Klar, T. A., Schietinger, S., Rogach, A. L., and Feldmann, J. *Nano Letters* **4**(9), 1599–1603 (2004).

46. Naruse, M., Runge, E., Kobayashi, K., and Ohtsu, M. *Physical Review B* **82**(12), 125417 (2010).

47. Franzl, T., Koktysh, D. S., Klar, T. A., Rogach, A. L., Feldmann, J., and Gaponik, N. *Applied Physics Letters* **84**(15), 2904 (2004).

48. Wuister, S. F., Koole, R., de Mello Donega, C., and Meijerink, A. *The journal of physical chemistry. B* **109**(12), 5504–8 (2005).

49. Lunz, M., Bradley, A. L., Lesnyak, V., and Gaponik, N. *Physical Review B* **81**(20), 205316 (2010).

50. Blumling, D. E., Tokumoto, T., McGill, S., and Knappenberger, K. L. *Physical Chemistry Chemical Physics* **14**(31), 11053–9 (2012).

51. Peng, X., Manna, L., Yang, W., Wickham, J., Scher, E., Kadavanich, A., and Alivisatos, A. *Nature* **404**(6773), 59–61 (2000).

52. Manna, L., Scher, E. C., and Alivisatos, A. P. *Journal of the American Chemical Society* **122**(51), 12700–12706 (2000).

53. Cassette, E., Mahler, B., Guigner, J.-M., Patriarche, G., Dubertret, B., and Pons, T. *ACS Nano* **6**(8), 6741–50 (2012).

54. Ithurria, S., Tessier, M. D., Mahler, B., Lobo, R. P. S. M., Dubertret, B., and Efros, A. L. *Nature Materials* **10**(12), 936–41 (2011).

55. Mahler, B., Nadal, B., Bouet, C., Patriarche, G., and Dubertret, B. *Journal of the American Chemical Society* **134**(45), 18591–8 (2012).

56. Rainò, G., Stöferle, T., Moreels, I., Gomes, R., Hens, Z., and Mahrt, R. F. *ACS Nano* **6**(3), 1979–87 (2012).

57. Rainò, G., Stöferle, T., Moreels, I., Gomes, R., Kamal, J. S., Hens, Z., and Mahrt, R. F. *ACS Nano* **5**(5), 4031–6 (2011).

58. Ithurria, S. and Dubertret, B. *Journal of the American Chemical Society* **130**(49), 16504–5 (2008).

59. Labeau, O., Tamarat, P., and Lounis, B. *Physical Review Letters* **90**(25), 257404 (2003).

60. Furis, M., Hollingsworth, J. A., Klimov, V. I., and Crooker, S. A. *Journal of Physical Chemistry B* **109**(32), 15332–15338 (2005).

61. Efros, A. In *Semiconductor and Metal Nanocrystals: Synthesis and Electronic and Optical Properties,* Klimov, V., editor, chapter 3, 103–141. Marcel Dekker, New York (2003).

62. Gupta, J. A., Awschalom, D. D., Efros, A. L., and Rodina, A. V. *Physical Review B* **66**(12), 125307 (2002).

63. Abragam, A. and Bleaney, B. *Electron Paramagnetic Resonance of Transition Ions*. Oxford University Press, England, (1970).

64. Efros, A., Ekimov, A., Kozlowski, F., Petrova-Koch, V., Schmidbaur, H., and Shumilov, S. *Solid State Communications* **78**(10), 853–856 (1991).

65. Bartsch, G., Gerbracht, M., Yakovlev, D., Blokland, J., Christianen, P., Zhukov, E., Dzyubenko, A., Karczewski, G., Wojtowicz, T., Kossut, J., Maan, J., and Bayer, M. *Physical Review B* **83**, 235317 (2011).

66. Astakhov, G., Yakovlev, D., Kochereshko, V., Ossau, W., Nürnberger, J., Faschinger, W., and Landwehr, G. *Physical Review B* **60**(12), R8485–R8488 (1999).

67. Efros, A. L. *Nature Materials* **7**(8), 612–3 (2008).

68. Galland, C., Ghosh, Y., Steinbrück, A., Hollingsworth, J. A., Htoon, H., and Klimov, V. I. *Nature Communications* **3**, 908 (2012).

69. Chepic, D., Efros, A., Ekimov, A., Ivanov, M., Kharchenko, V., Kudriavtsev, I., and Yazeva, T. *Journal of Luminescence* **47**(3), 113–127 (1990).

70. Wang, X., Ren, X., Kahen, K., Hahn, M. A., Rajeswaran, M., Maccagnano-Zacher, S., Silcox, J., Cragg, G. E., Efros, A. L., and Krauss, T. D. *Nature* **459**(7247), 686–9 (2009).

71. Jha, P. P. and Guyot-Sionnest, P. *ACS Nano* **3**(4), 1011–5 (2009).

72. Jha, P. P. and Guyot-Sionnest, P. *The Journal of Physical Chemistry C* **114**(49), 21138–21141 (2010).

73. Qin, W., Shah, R. A., and Guyot-Sionnest, P. *ACS Nano* **6**(1), 912–8 (2012).

74. Fernée, M. J., Littleton, B. N., and Rubinsztein-Dunlop, H. *ACS Nano* **3**(11), 3762–8 (2009).

75. Louyer, Y., Biadala, L., Tamarat, P., and Lounis, B. *Applied Physics Letters* **96**, 203111 (2010).

76. Fernée, M. J., Sinito, C., Louyer, Y., Potzner, C., Nguyen, T.-L., Mulvaney, P., Tamarat, P., and Lounis, B. *Nature Communications* **3**, 1287 (2012).

77. Dyakonov, M., editor. *Spin Physics in Semiconductors*. Springer-Verlag, Berlin, (2008).

78. Meier, F. and Zakharchenya, B. *Optical Orientation.* North-Holland, Amsterdam, (1984).

79. Ivchenko, E. *OPtical spectroscopy of semiconductor nanostrucutres.* Alpha Science, Harrow, (2005).

80. Wijnen, F. J. P., Blokland, J. H., Chin, P. T. K., Christianen, P. C. M., and Maan, J. C. *Physical Review B* **78**(23), 235318 (2008).

81. Stern, N., Poggio, M., Bartl, M., Hu, E., Stucky, G., and Awschalom, D. *Physical Review B* **72**, 161303(R) (2005).

82. Mahler, B., Lequeux, N., and Dubertret, B. *Journal of the American Chemical Society* **132**(3), 953–9 (2010).

83. De Mello Donegá, C., Bode, M., and Meijerink, A. *Physical Review B* **74**(8), 085320 (2006).

84. Blokland, J., Claessen, V., Wijnen, F., Groeneveld, E., de Mello Donegá, C., Vanmaekelbergh, D., Meijerink, A., Maan, J., and Christianen, P. *Physical Review B* **83**(3), 035304 (2011).

85. Moreels, I., Rainò, G., Gomes, R., Hens, Z., Stöferle, T., and Mahrt, R. F. *ACS Nano* **5**(10), 8033–9 (2011).

86. Shabaev, A., Rodina, A. V., and Efros, A. L. *Physical Review B* **86**(20), 205311 (2012).

87. Broser, I., Broser, R., and Hoffmann, A. In *Landolt-Bornstein Tables, New Series, Group III: Crystals and Solid State Physics, Vol. 17: Semiconductors; Subvolume b: Physics of II-VI and I-VII Compounds, Semimagnetics Semiconductors,* Madelang, O., editor, 202–224. Springer-Verlag, Berlin (1982).

88. Sirenko, A. A., Ruf, T., Cardona, M., Yakovlev, D. R., Ossau, W., Waag, A., and Landwehr, G. *Physical Review B* **56**(4), 2114 (1997).

89. Yugova, I. A., Greilich, A., Zhukov, E. A., Yakovlev, D. R., Bayer, M., Reuter, D., and Wieck, A. D. *Physical Review B* **75**(19), 195325 (2007).

90. Trif, M., Simon, P., and Loss, D. *Physical Review Letters* **103**(10), 106601 (2009).

91. Fras, F., Eble, B., Desfonds, P., Bernardot, F., Testelin, C., Chamarro, M., Miard, A., and Lemaître, A. *Physical Review B* **86**(4), 045306 (2012).

92. Takagahara, T. *Journal of Luminescence* **70**(1-6), 129–143 (1996).

93. Chen, Y., Okuno, T., Masumoto, Y., Terai, Y., Kuroda, S., and Takita, K. *Physical Review B* **71**(3), 033314 (2005).

94. Scholes, G., Kim, J., and Wong, C. *Physical Review B* **73**(19), 195325 (2006).

95. Takagahara, T. *Physical Review B* **62**(24), 16840–16855 (2000).

96. Ma, H., Jin, Z., Zhang, Z., Li, G., and Ma, G. *The journal of physical chemistry. A* **116**(9), 2018–23 (2012).

97. Cassette, E. *Nanocristaux de semi-conducteurs II_ VI et I-III-VI: Contrôle des propriétés optiques de structures coeur/coque*. PhD thesis, (2012).

98. Tessier, M. D., Biadala, L., Bouet, C., Ithurria, S., Abecassis, B., and Dubertret, B. *ACS Nano* **7**(4), 3332–40 (2013).

99. Andreani, L. C., Tassone, F., and Bassani, F. *Solid State Communications* **77**(9), 641–645 (1991).

100. Nirmal, M., Murry, C., and Bawendi, M. *Physical Review B* **50**(4), 2293 – 2300 (1994).

101. Kochereshko, V., Mikhailov, G., and Uraltsev, I. *Sov. Phys. Solid State* **25**, 435 (1983).

102. Jeukens, C. R. L. P. N., Christianen, P. C. M., Maan, J. C., Yakovlev, D. R., Ossau, W., Kochereshko, V. P., Wojtowicz, T., Karczewski, G., and Kossut, J. *Physical Review B* **66**(23), 235318 (2002).

Symbols and Abbreviations

ΔE	energy difference
η_{A},η_{F}	radiative quantum efficiency of bright and dark states
η_{o},η_{p}	radiative quantum efficiency of oblate and prolate NCs
γ_0	the relaxation rate from bright state to dark state at zero temperature
γ_{L},γ_{S}	radiative decay rate of the long and short component of PL decay
$\hbar$	reduced Plank constant
λ	wavelength
μ	shape factor of ellipsoid
μeV	micro electron volt
μ_{B}	Bohr magneton
ψ	wave function
ρ	spin polarization degree
$\sigma+$,$\sigma-$	right-handed, left-handed circular polarization
τ_{r}	radiative decay time
τ_{s}	spin relaxation time
$\mathbf{B}$	magnetic field vector
θ	angle between magnetic field and NC quantization axis
a	radius of the nanocrystal
B	magnetic field
b	the minor axes of the ellipsoid

c	the major axes of the ellipsoid
E	energy
f	a fraction of NCs
g	Landé g-factor
I^+,I^-	PL intensity of σ^+ and σ^- components
J_z	projection of total momentum of exciton
k_B	Boltzmann constant
M	projection of the total momentum of hole
m^*	effective mass
N	number of particles
N_B	Bose-Einstein phonon number at specific temperature
P	PL polarization degree
s_z	projection of electron spin
T	temperature
x	$\cos(\theta)$
J	sum of the electron spin and total momentum of hole
r	position vector
a, d	acceptor and donor NCs
A, F	optically allowed and forbidden states
c	circular polarization
CCD	charge-coupled device
cm	centimeter
CW	continuous wave
e	electron
eq	equlibrium
ET	energy transfer
eV	electron volt

FRET	Förster resonant energy transfer
FWHM	full width at half maximum
G	ground state
hh	heavy hole
lh	light hole
meV	milli electron volt
NC	nanocrystal
nm	nanometer
PL	photoluminescence
QD	quantum dot
T	Tesla
t	time
TEM	transmission electron microscope
th	thermal

List of Figures

List of Tables

Publications

Part of this work are or will be published as follows:

(i) F. Liu, L. Biadala, A. V. Rodina, D. R. Yakovlev, D. Dunker, C. Javaux, J-P. Hermier, Al. L. Efros, B. Dubertret and M. Bayer, Spin dynamics of negatively charged excitons in CdSe/CdS colloidal nanocrystals, *Physical Review B*, **88**(3), 035302 (2013).

(ii) C. Javaux, B. Mahler, B. Dubertret, A. Shabaev, A. V. Rodina, Al. L. Efros, D. R. Yakovlev, F. Liu, M. Bayer, G. Camps, L. Biadala, S. Buil, X. Quelin and J-P. Hermier, Thermal activation of non-radiative Auger recombination in charged colloidal nanocrystals, *Nature Nanotechnology*, **8**(3), 206-12 (2013).

(iii) A. Greilich, A. Pawlis, F. Liu, O. A. Yugov, D. R. Yakovlev, K. Lischka, Y. Yamamoto, and M. Bayer, Spin dephasing of fluorine-bound electrons in ZnSe, *Physical Review B*, **85**(12), 121303(R) (2012) (Editor recommended).

(iv) D. Sercombe, S. Schwarz, O. Del Pozo-Zamudio, F. Liu, B. J. Robinson, E. A. Chekhovich, I. I. Tartakovskii, O. Kolosov, A. I. Tartakovskii, Dielectric surface and capping effects on optical properties of a few atomic monolayer thick MoS_2, submitted to *Scientific Reports*.

(v) F. Liu, A. V. Rodina, D. R. Yakovlev, E. D. Vakhtin, A. Susha, A. L. Rogach and M. Bayer, Förster energy transfer in ensemble of CdTe colloidal nanocrystal, in preparation for *Physical Review B*.

(vi) F. Liu, A. V. Rodina, D. R. Yakovlev, A. L. Rogach and M. Bayer, Exciton spin dynamics of CdTe colloidal nanocrystals in magnetic fields, in preparation for *Applied Physics Letters*.

(vii) L. Biadala, F. Liu, D. R. Yakovlev, M. Bayer, et al.. Fast recombination of the band edge exciton in nanoplatelets, in preparation for *Physical Review Letters*.

Acknowledgments

This thesis would not have been completed without the help and support from my supervisors, colleagues, family and friends. Overall, I appreciate their great help and support!

Above all, I want to thank Prof. Dr. Manfred Bayer and Prof. Dr. Dmitri Yakovlev for giving me the opportunity to conduct the exciting research on colloidal semiconductor nanostrcutres. I greatly appreciate Prof. Dr. Dmitri Yakovlev for his careful and irreplaceable guidance.

Next, I would like to express my gratefulness to Dr. Gregor Bartsch, Dr. Louis Biadala and Dr. Anna Rodina. I benefit a lot from the patient demonstration of experimental techniques by Dr. Gregory Bartsch and Dr. Louis Biadala and their suggestions on various topics. I greatly acknowledge Dr. Anna Rodina for her invaluable theoretical support and guidance. Without their help, I could not have completed my thesis as planned.

I want to give my sincere appreciation to Dr. Jörg Debus, Dr. Alex Greilich, Dr. Ilya Akimov, Daniel Dunker, Tillmann Godde for the great help on my experimental work and illuminating discussions. I also want to thank Franziska Wishahi and Alexander Schwan for their great help, especially on the preparation of my thesis.

Meanwhile, I want to thank Prof. Dr. Dietmar Fröhlich and Dr. Jean-Sebastian Tempel for teaching me Deutsch, Prof. Dr. Evgeny Zhukov for very helpful discussions and Dr. Alexey Salasyuk for nice kicker games. I also want to thank Michaela Wäscher for the efficient admistration work and Klaus Wiegers and Lars Wieschollek for the excellent technique support. I want to thank all of my E2 colleagues who provide such a warm and enjoyable atmosphere.

Also, I must thank my parents Liu Xiangdong and Zhang Yan. There is no doubt that all of my achievements root deeply in the support of my family.

Finally, I want to thank all of other people whom I did not mention above. I need to say that the completion of this thesis not only depended on my own work, but also needed the support from all the people who once helped me.